

Thermoplastic composite stiffened structures in post-buckling

van Dooren, K.S.

DOI

[10.4233/uuid:b2f2e450-63dd-40cf-af09-bf67411e5980](https://doi.org/10.4233/uuid:b2f2e450-63dd-40cf-af09-bf67411e5980)

Publication date

2024

Document Version

Final published version

Citation (APA)

van Dooren, K. S. (2024). *Thermoplastic composite stiffened structures in post-buckling*. [Dissertation (TU Delft), Delft University of Technology]. <https://doi.org/10.4233/uuid:b2f2e450-63dd-40cf-af09-bf67411e5980>

Important note

To cite this publication, please use the final published version (if applicable). Please check the document version above.

Copyright

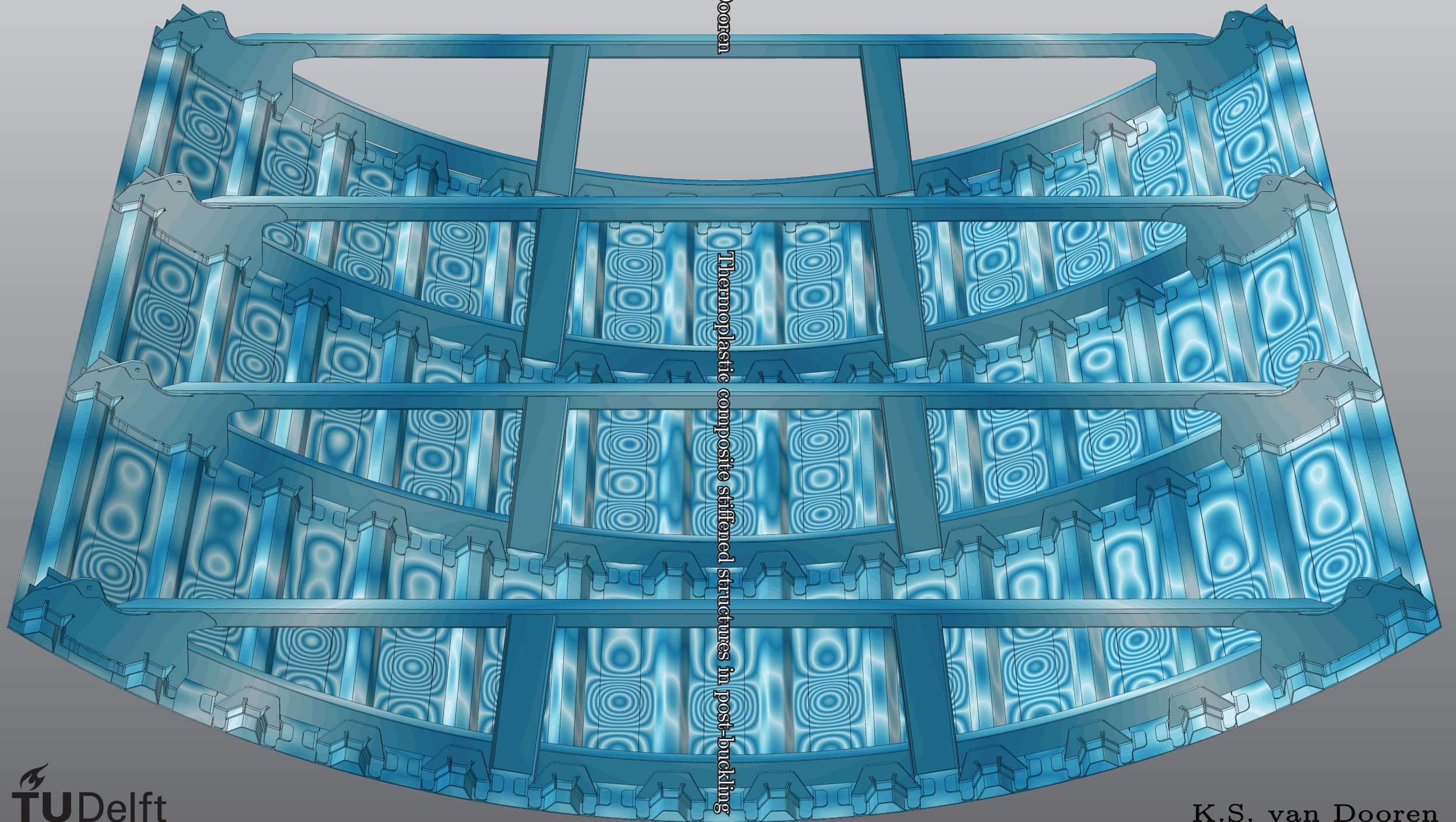
Other than for strictly personal use, it is not permitted to download, forward or distribute the text or part of it, without the consent of the author(s) and/or copyright holder(s), unless the work is under an open content license such as Creative Commons.

Takedown policy

Please contact us and provide details if you believe this document breaches copyrights. We will remove access to the work immediately and investigate your claim.

Thermoplastic composite stiffened structures in post-buckling

K.S. van Dooren



Thermoplastic composite stiffened structures in post-buckling

**THERMOPLASTIC COMPOSITE STIFFENED
STRUCTURES IN POST-BUCKLING**

THERMOPLASTIC COMPOSITE STIFFENED STRUCTURES IN POST-BUCKLING

Dissertation

for the purpose of obtaining the degree of doctor
at Delft University of Technology
by the authority of the Rector Magnificus Prof. dr. ir. T.H.J.J. van der Hagen
chair of the Board for Doctorates
to be defended publicly on
Wednesday 15 May 2024 at 10:00 o'clock

by

Kevin Steven VAN DOOREN

Master of Science in Aerospace Engineering,
Delft University of Technology, the Netherlands
born in Schaijk, The Netherlands.

This dissertation has been approved by the promotor.

Composition of the doctoral committee:

Rector Magnificus,	chairperson
Prof. dr. C. Bisagni,	Delft University of Technology, <i>promotor</i>
Dr. S. R. Turteltaub,	Delft University of Technology, <i>promotor</i>

Independent members:

Prof. dr. R. Butler	University of Bath, UK
Prof. dr. ir. M. Langelaar	Delft University of Technology
Prof. Dr. -Ing. K.U. Schröder	RWTH Aachen University, Germany
Prof. Dr. -Ing. R. Degenhardt	DLR, Germany
Prof. dr. ir. L.J. Sluys	Delft University of Technology

The research was supported by the Clean Sky 2 project STUNNING - SmarT Multi-FuNctional and INtegrated TP FuselaGe (grant agreement No 945583).



Keywords: Thermoplastic composite, post-buckling, skin-stringer separation, stiffened panels, welding, butt-joint, testing, damage tolerance, finite element, virtual crack closure technique

Printed by: Ipskamp

Cover: Designed by Kevin van Dooren. Post-buckling analysis of STUNNING fuselage keel section. Fuselage geometry design courtesy of Fokker/GKN Aerospace.

Copyright © 2024 by K.S. van Dooren
ISBN 978-94-6473-489-8

An electronic version of this dissertation is available at
<http://repository.tudelft.nl/>.

CONTENTS

Summary	ix
Samenvatting	xiii
1 Introduction	1
1.1 Projects on thermoplastic composites	1
1.2 Post-buckling behaviour	3
1.3 Dissertation outline	4
2 Design, analysis and testing of thermoplastic welded stiffened panels to investigate skin-stringer separation in post-buckling	7
2.1 Introduction	8
2.2 Thermoplastic fuselage section	9
2.3 Numerical analysis of fuselage section	11
2.4 Panel design and manufacturing	15
2.5 Test setup	18
2.6 Panel measurements	20
2.7 Experimental and numerical results	21
2.7.1 Load versus displacement curves	21
2.7.2 Load versus strain curves	22
2.7.3 Evolution of buckling shape	25
2.7.4 Final failure	25
2.7.5 Post-failure.	28
2.7.6 Weld fracture surface.	30
2.8 Concluding remarks	31
3 Post-buckling damage tolerance of welded omega-stiffened thermoplastic panels with initial damage	33
3.1 Introduction	34
3.2 Welded omega-stiffened thermoplastic panels	36
3.3 Numerical analysis of welded omega-stiffened thermoplastic panels with initial damage	38
3.3.1 Analysis methodology	38
3.3.2 Effect of damage size and location	39
3.4 Test setup and panels measurements	42
3.5 Damage and imperfection sensitivity study.	44
3.5.1 Damage size sensitivity	45
3.5.2 Damage location sensitivity	48

3.6	Test and numerical results	51
3.6.1	Panel 1: pristine panel	51
3.6.2	Panel 2: one initial damage in middle stringer	54
3.6.3	Panel 3: two initial damages in middle stringer.	58
3.6.4	Panel 4: one damage in side stringer	62
3.7	Summary and discussion	65
3.8	Concluding remarks	66
4	Design, analysis and testing of thermoplastic welded stiffened panels to investigate skin-stringer separation in post-buckling	69
4.1	Introduction	70
4.2	Panel geometry and material	72
4.3	Geometrical imperfections	75
4.4	Finite element analysis	76
4.5	Test setup	79
4.6	Test results and comparison to numerical prediction	81
4.6.1	Load versus displacement curves	81
4.6.2	Load versus strain curves	82
4.6.3	Out-of-plane displacement	84
4.6.4	Skin-stringer separation	86
4.6.5	Fracture surface	87
4.6.6	Mode-Mixity	88
4.6.7	First ply failure.	89
4.6.8	Final failure mode	90
4.7	Conclusions	92
5	Buckling and failure assessment of curved butt-joint stiffened thermoplastic composite panels with roller boundary conditions	93
5.1	Introduction	94
5.2	Panel geometry	95
5.3	Numerical methodology	97
5.3.1	Comparison of boundary condition approximation.	98
5.3.2	Damage and mesh size sensitivity	101
5.3.3	Skin-stringer separation	102
5.4	Test setup	103
5.5	Test and numerical results	105
5.5.1	Load versus displacement curves.	105
5.5.2	Load versus rotation curves	105
5.5.3	Strain gauge curves	106
5.5.4	Out-of-plane displacement	108
5.5.5	Panel collapse	110
5.5.6	Post-failure investigation.	113
5.6	Concluding remarks	116
6	Conclusions and recommendations	117
6.1	Conclusions	117
6.2	Recommendations	122

Bibliography	125
List of Publications	133
Acknowledgments	135
Biographical note	139

SUMMARY

The aeronautical industry has set ambitious goals to reduce its environmental impact and become sustainable. Addressing rising emissions involves strategies such as reducing structural weight, due to its direct impact on fuel consumption, and the use of new materials and manufacturing techniques. Research and development on thermoplastic composites has seen an uprise due to their mechanical properties and sustainability benefits. It enables cost-effective, innovative manufacturing techniques, less manufacturing waste and recyclability. This has led to the launch of several projects utilising thermoplastics, such as TAPAS 1 and 2 in The Netherlands, and the Clean Sky 2 project STUNNING. The TAPAS projects focussed on co-consolidated structures with the butt-joint technique, while STUNNING developed and manufactured a lower half of the multifunctional fuselage demonstrator, one of the world's largest thermoplastic structures.

This thesis investigates the post-buckling and skin-stringer separation behaviour of thermoplastic composite structures, with a combined experimental and numerical methodology. Allowing structures to buckle below the ultimate load can lead to considerable weight savings, however, the failure of composite structures in post-buckling is complex and usually catastrophic. This research intends to close the knowledge gap on thermoplastic composites in post-buckling, contributing to the goal of sustainable structures allowed to operate in post-buckling.

Thermoplastic composite panels with three omega stiffeners and conduction welded joints are designed by analysis and tested in post-buckling to study the welded joint performance. The panels are designed such that their structural behaviour is representative of the lower half of the Clean Sky 2 STUNNING multifunctional fuselage demonstrator. Finite element analysis is executed on a fuselage section, which consists of a simplified STUNNING keel section and incorporates skin-stringer separation in the pristine welded joint with the virtual crack closure technique. The fuselage's skin-stringer separation and post-buckling behaviour are analysed and serve as the reference for the three-stringer panel design. Two panels, manufactured by National Aerospace Laboratory (NLR) and GKN Fokker, are instrumented and tested till final failure. The test setup includes high-speed cameras to capture final failure and digital image correlation to measure panel deformation. The panels exhibit skin-stringer separation in post-buckling, starting with the unstable separation of the middle stringer, followed by the outer stringers separation and fracture of two stringers. The numerical analysis of the panels incorporates geometrical imperfections, as measured by digital image correlation. The analysis accurately predicts the structural behaviour, demonstrating only minor differences in buckling and separation behaviour.

The welded omega stiffened panels are further investigated, featuring initial damage in the conduction welded joint, for damage tolerance behaviour in post-buckling. Finite element analyses are executed with the virtual crack closure technique to model skin-stringer separation of pristine joints and joints with initial damage. Four panels are tested, with initial damage in three panels and one panel in pristine condition. The initial damage is

created by inserting a foil at the skin-stringer interface before welding. The buckling shape evolution and interaction with the initial damage is captured by digital image correlation. The panels show indications of minor stable separation growth at the initial damage from the out-of-plane displacement measurement and camera footage. This is followed by unstable separation as captured by the high-speed camera, starting from the initial damage location. The panels with one damage collapse once separation starts, but the panel with two initial damages exhibits a separation event of the middle stringer and continues to carry load followed by collapse. The numerical analysis predicts the structural behaviour well, with a conservative failure load prediction when there's initial damage in the middle stringer. The initial buckling is predicted accurately. However, the analysis has difficulty predicting the buckling shape evolution at higher loads.

Two thermoplastic composite stiffened panels utilising the butt-joint technique are analysed and tested to study the buckling behaviour and final failure mode. The panels are manufactured by co-consolidated and are of fast crystallising polyetherketoneketone carbon composite. The panels have three stringers with an angled cap on the side, with short-fibre filler to join the cap to the web, and the web to the skin. The middle skin-stringer interface has initial damage that represents barely visible impact damage. Finite element analyses, which use the virtual crack closure technique in the short-fibre filler interface, are executed to predict the structural behaviour. In the tests, damage propagation is captured by cameras, panel deformation is measured by digital image correlation and final failure is captured by high-speed cameras at the cap-side of the stringer. The initial buckling shape of the panel consists of three half-waves per bay, with a fourth half-wave appearing at higher loads in one of the bays. Damage propagation starts early after buckling, with a combination of both stable and unstable damage propagation followed by final failure. The middle stringer separates, followed by the collapse of the panel. The analysis predicts the structural behaviour accurately, with the buckling and failure behaviour showing excellent agreement.

Two curved thermoplastic composite panels with five stringers, butt-joint and roller boundary conditions are analysed and tested. The rollers are attached to the loading edges to approximate simply-supported boundary conditions that apply compression and bending to the panels. One panel is pristine, and the second has one barely visible impact damage in the butt-joint skin-stringer interface. The roller boundary conditions are approximated with three different approaches in the finite element analysis, after which the option with physical rollers but no contact is chosen as the best option. The following analysis to predict the test includes material damage and damage evolution. Panel failure is captured by high-speed cameras, and occurs in a sudden matter. Collapse starts with the cap separation from the web, after which the web fails and cripples and the butt-joint exhibits skin-stringer separation. Closer examination of the failed panels and high-speed footage reveals that the top plies of the web have failed and are still attached to the cap, indicating material failure of the web as the critical failure mode. The structural behaviour is well predicted by the finite element analysis, but it cannot predict the sudden panel collapse due to material damage in the web and the following cap separation.

Thermoplastic composite stiffened structures were extensively investigated. The thesis demonstrates the extensive possibilities w.r.t. manufacturing and designs of thermoplastic composites for stiffened panels and the robustness of using classical analysis methods devel-

oped initially for thermoset composites. The post-buckling performance, predictability, and damage tolerance of the structures investigated show the great potential of thermoplastic composites in primary aeronautical sustainable structures.

SAMENVATTING

De luchtvaartindustrie heeft ambitieuze doelen gesteld om te verduurzamen en haar impact op het milieu te verminderen. De aanpak van stijgende emissies bevat strategieën zoals het verlagen van het structurele gewicht, vanwege de directe invloed op het brandstofverbruik, en het gebruik van nieuwe materialen en productietechnieken. Onderzoek en ontwikkeling van thermoplastische composieten heeft een toename gezien vanwege de mechanische eigenschappen en duurzaamheid. Het maakt innovatieve en kosteneffectieve productietechnieken mogelijk, met minder productieafval en meer recycling mogelijkheden. Dit heeft geleid tot de lancering van verschillende projecten voor de ontwikkeling van thermoplastische structuren, zoals TAPAS 1 en 2 in Nederland, en het Clean Sky 2-project STUNNING. De TAPAS-projecten richtten zich op structuren voortkomend uit co-consolidatie met de kops-verbindingstechniek, terwijl STUNNING de onderste helft van een multifunctionele romp-demonstrator ontwikkelde en produceerde, een van 's werelds grootste thermoplastische structuren.

Deze scriptie onderzoekt het naknik en het huid-verstijver loslaat-gedrag van thermoplastische composietstructuren, met een gecombineerde experimentele en numerieke methodologie. Het toestaan van structuren om te knikken onder de ultieme belasting kan aanzienlijke gewichtsbesparingen opleveren, maar het falen van composietstructuren in naknik is complex en meestal catastrofaal. Dit onderzoek beoogt het kennistekort over thermoplastische composieten in naknik te dichten, bijdragend aan het doel van duurzame structuren die in naknik mogen opereren.

Thermoplastische composietpanelen met drie omega-verstijvers en conductie gelaste verbindingen worden ontworpen door middel van analyse en getest in naknik om de prestaties van de gelaste verbinding te bestuderen. De panelen zijn ontworpen zodat hun structureel gedrag representatief is voor de onderste helft van de Clean Sky 2 STUNNING multifunctionele romp-demonstrator. Eindige-elementenanalyse wordt uitgevoerd op een rompsectie, die bestaat uit een vereenvoudigde STUNNING kielsectie met huid-verstijver loslating in de ongerepte gelaste verbinding met de virtueel crack closure-techniek. De huid-verstijver loslating en naknik-gedrag van de romp worden geanalyseerd en dienen als referentie voor het ontwerp van het paneel met drie verstijvers. Twee panelen, vervaardigd door het Nationaal Lucht- en Ruimtevaartlaboratorium (NLR) en GKN Fokker, worden geïnstrumenteerd en getest tot het definitieve falen. De testopstelling bevat hogesnelheidscamera's om het definitieve falen vast te leggen en digital image correlation om de vervorming van het paneel te meten. De panelen vertonen huid-verstijver loslating in naknik, te beginnen met de onstabiele loslating van de middelste verstijver gevolgd door de loslating van de buitenste verstijver en breuk van twee verstijvers. De numerieke analyse van de panelen omvat geometrische imperfecties zoals gemeten door digital image correlation. De analyse voorspelt het structurele gedrag nauwkeurig, met slechts kleine verschillen in knik - en verstijver loslaat-gedrag.

De gelaste omega-versterkte panelen worden verder onderzocht, met initiële schade in de conductie gelaste verbinding, voor het schadetolerantie gedrag in naknik. Eindige-elementenanalyses worden uitgevoerd met de virtueel crack closure-techniek om huid-verstijver loslating van ongerepte verbindingen en verbindingen met initiële schade te modelleren. Vier panelen worden getest, met initiële schade in drie panelen en één paneel in ongerepte staat. De initiële schade wordt gecreëerd door een folie in de huid-verstijver interface te plaatsen voor het lassen. De vormevolutive tijdens knik en de interactie met de initiële schade wordt vastgelegd door digital image correlation. De panelen vertonen indicaties van lichte stabiele groei van de initiële schade vanuit de meting van verplaatsing uit het vlak en camerabeelden. Dit wordt gevolgd door onstabiele loslating zoals vastgelegd door de hogesnelheidscamera, beginnend vanaf de locatie van de initiële schade. De panelen met één schade falen zodra de loslating begint, maar het paneel met twee initiële schades vertoont een loslating van de middelste verstijver en gaat door met het dragen van belasting gevolgd door falen. De numerieke analyse voorspelt het structurele gedrag goed, met een conservatieve voorspelling van de faallast wanneer er initiële schade is in de middelste verstijver. Het initiële knikken wordt nauwkeurig voorspeld. De analyse heeft echter moeite met het voorspellen van de evolutie van de knik -vorm bij hogere belastingen.

Twee thermoplastische composiet versterkte panelen met de kops-verbindingstechniek worden geanalyseerd en getest om het knik -gedrag en de uiteindelijke faalwijze te bestuderen. De panelen zijn vervaardigd met co-consolidatie en zijn van snel kristalliserend polyetherketonketon-koolstofcomposiet. De panelen hebben drie verstijvers met een schuin kapje aan de zijkant, en de verbinding tussen kap en web, en web aan huid, bestaat uit korte vezelvuller. De interface van de middelste huid-verstijver heeft initiële schade die nauwelijks zichtbare impactschade vertegenwoordigt. Eindige-elementenanalyses, met de virtueel crack closure-techniek in de interface tussen huid en de korte vezelvuller, worden uitgevoerd om het structurele gedrag te voorspellen. In de tests wordt schade-groei vastgelegd door camera's, wordt de vervorming van het paneel gemeten door digital image correlation en wordt het definitieve falen vastgelegd door hogesnelheidscamera's aan de zijde van de verstijver-kap. De initiële knik -vorm van het paneel bestaat uit drie half-golven per baai, met een vierde half-golf die verschijnt bij hogere belastingen in een van de baaien. Schadegroei begint vroeg na het knikken, met een combinatie van zowel stabiele als onstabiele schadegroei gevolgd door definitief falen. De middelste verstijver laat los, gevolgd door het falen van het paneel. De analyse voorspelt het structurele gedrag nauwkeurig, en het knik - en faalgedrag vertoont uitstekende overeenkomst.

Twee gebogen thermoplastische composietpanelen met vijf verstijvers, kops-verbinding en rolrandvoorwaarden worden geanalyseerd en getest. De rollers zijn bevestigd aan de belastingsvlakken om eenvoudig oplegging voorwaarden te benaderen die compressie en buiging op de panelen toepassen. Eén paneel is ongerept, en de tweede heeft een nauwelijks zichtbare impactschade in de kops-verbinding tussen huid en verstijver. De rolrandvoorwaarden worden benaderd met drie verschillende methodes in de eindige-elementenanalyse, waarna de optie met fysieke rollers maar zonder contact als de beste optie wordt gekozen. De daaropvolgende analyse om de test te voorspellen bevat materiaalschade en schade-evolutie. Het falen van het paneel wordt vastgelegd door hogesnelheidscamera's en het falen gebeurt op een plotselinge manier. Falen begint met de loslating van de kap van de web, waarna de web faalt en breekt en de huid-verstijver loslating vertoont in de kops-

verbinding. Nader onderzoek van de gefaalde panelen en hogesnelheidsbeelden onthult dat de bovenste lagen van het weblaminaat zijn gefaald en nog steeds aan de kap zijn bevestigd, wat wijst op materiaalfalen van de web als de kritische faalwijze. Het structurele gedrag wordt goed voorspeld door eindige elementen, maar het kan de plotselinge falen van het paneel door materiaalschade in de web en daaropvolgende kap loslating niet voorspellen.

Thermoplastische composiet versterkte structuren zijn uitgebreid onderzocht. De scriptie toont de uitgebreide mogelijkheden met betrekking tot de productie en ontwerpen van thermoplastische composieten voor verstijfde panelen en de robuustheid van het gebruik van klassieke analysemethoden die oorspronkelijk zijn ontwikkeld voor thermohardende composieten. De naknik-prestaties, voorspelbaarheid en schadetolerantie van de structuren die zijn onderzocht, tonen het grote potentieel van thermoplastische composieten in primaire duurzame luchtvaartstructuren.

1

INTRODUCTION

The aeronautical industry has set ambitious goals for lowering its environmental impact and becoming sustainable. One strategy to reduce emissions is to lower fuel consumption, among other strategies, which in turn results in cost savings. An effective way of doing so is by lowering the aircraft's weight, as weight is directly linked to fuel consumption during flight. This weight reduction can also increase the passenger capacity per flight, reducing the required number of flights.

Thermoplastic composites have seen an uprise in research and development in the aeronautical field because of their mechanical properties and how they can aid in sustainability. Thermoplastics offer high recycling potential thanks to their ability to be melted multiple times with minor or no degradation, which also aids in the reduction of manufacturing waste and repairs. For instance, compression moulding of shredded trimmings into panels with ribs [1], and compression moulded rotorcraft door hinges of recycled fragments [2]. Thermoplastics allow for new manufacturing techniques, such as hot press forming, co-consolidation and thermoplastic welding. These techniques allow for faster processing times, fewer parts to assemble and reduced cost. Thermoplastics are also known to have higher toughness, leading to less brittle failure behaviour, which is a considerable advantage for damage tolerance.

1.1 PROJECTS ON THERMOPLASTIC COMPOSITES

In recent years, a number of projects have successfully been conducted on thermoplastic composite aeronautical structures, of which the projects relevant to this thesis will be discussed in chronological order.

The Thermoplastic Affordable Primary Aircraft Structure (TAPAS) 1 project was launched in The Netherlands in 2009, consisting of several partners, including GKN Fokker, NLR and Airbus, and investigated the necessary manufacturing technologies for thermoplastic primary structures [3]. It resulted in various new manufacturing techniques and delivered a torsion box and a fuselage shell demonstrator. The manufacturing techniques for the demonstrators included automated fibre placement, co-consolidation, press forming and thermoplastic welding. They incorporated the butt-joint concept to join skin and stringer and the use of carbon fibre PEKK. Both demonstrators were tested, and the torsion

box underwent a complete certification test programme. Considerable weight savings were achieved thanks to the separated skin and stiffener design, increasing the design space, and the higher toughness of thermoplastics allowed for thinner laminates due to better crack growth prevention.

A second project, called TAPAS 2, started in 2014, building on the achievements of TAPAS 1 [4]. The project further explored the demonstrators of TAPAS 1, achieved higher TRL levels for the thermoplastic technologies and developed an orthogrid fuselage shell entirely out of thermoplastic composites. It utilised innovative stiffening and joining techniques such as the butt-joint concept, resulting in a fastener-free fuselage design. This eliminated the requirement for a "mouse hole" in the frame, which the stringer would pass through in traditional designs. Further technology developments from the TAPAS projects concentrated on orthogrid shells with double curvature, with an example shown in Figure 1.1, including convex and concave sections [5]. The orthogrid shells utilized conduction welding to join the frame to the grid and capitalized on the manufacturability of thermoplastics, allowing for a more aerodynamic tail section for a jet to be designed while being cost-effective.

In this thesis, structures representative of a jet fuselage that utilises technologies originating from the TAPAS projects are investigated on the post-buckling and failure behaviour, emphasising the behaviour of the butt-joint.



Figure 1.1: Orthogrid double curvature fuselage panel [5].

In 2017, the Clean Sky 2 “SmarT mUlti-fuNctioNal and INtegrated TP fuselaGe” STUNNING project was initiated as part of the Horizon 2020 innovation funding programme of the European Union [6]. This project designed and manufactured the lower half of the thermoplastic multi-functional fuselage demonstrator, which is shown in Figure 1.2. The fuselage uses a wide variety of manufacturing techniques, including press-forming, compression moulding, and different types of thermoplastic welding of critical joints [7]. The fuselage is 8.5 meters long and 4 meters in diameter. It includes substructures such as the floor and cargo floor structure, energy absorbers, and is one of the largest thermoplastic structures in the world. It is the first full-scale fuselage for a large passenger aircraft made of carbon fibre LM-PAEK, and the design concentrates heavily on integrating sub-structures and systems. This allows further weight reduction, while the manufacturing techniques lead to shorter production times, with the project aiming to enable production rates of 60-100 aircraft/month. The fuselage skin was manufactured by National Aerospace Labora-

tory (NLR) utilising Automatic Fibre Placement (AFP), to which continuous compression moulded omega stringers from Xelis were conduction welded by GKN Fokker. GKN Fokker also manufactured the frame and floor beam sub-assemblies and was responsible for assembling the fuselage, which was executed at Smart Advanced Manufacturing XL (SAM XL) in Delft. The sub-assemblies were joined to the stiffened skin with injection-moulded clips of ECO-CLIP, for which ultrasonic welding was used in cooperation with Delft University of Technology. SAM XL developed also an industry-ready assembly process, by integrating robotics for ultrasonic welding and pick and place of stringers, and developed smart control and programming methods.

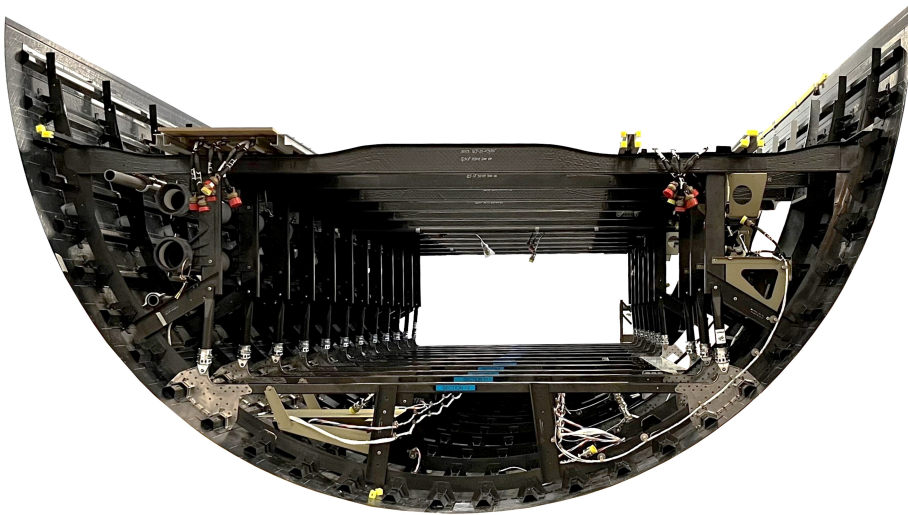


Figure 1.2: Lower half of the STUNNING fuselage [8].

Within the STUNNING project, the structural performance of thermoplastic composites was investigated and linked to the manufacturing techniques on several structural scales. In this thesis, the conduction welded joint of the stiffened skin of the STUNNING fuselage is investigated to evaluate the strength in post-buckling. The investigation includes the design of sub-components by analysis, aiming for structural behaviour representative of larger components, and testing and analysis of structures for pristine and damage tolerance performance.

1.2 POST-BUCKLING BEHAVIOUR

In aeronautics, the thin-walled designs of the fuselage and wing structures are subjected to compression and shear loads in flight, which can lead to buckling. Structural weight savings can be accomplished if the aforementioned structures are allowed to buckle below the ultimate load in certain loading conditions. It has already been shown that they are able to carry load far into the post-buckling field. However, the failure of composite structures in post-buckling can be complex and catastrophic, with behaviour that is difficult to

predict. These structures are susceptible to damage throughout manufacturing, in-service or maintenance. Internal damage may occur without apparent signs and leave it undiscovered following visual inspection. This heightens concerns about allowing these structures to operate in the post-buckling field, with the already complex post-buckling behaviour and potential interaction with internal damages in mind. To achieve post-buckled composite primary structures, the knowledge and understanding of the post-buckling behaviour and damage tolerance needs to be expanded, especially for structures manufactured with new technologies and materials.

In the research field on the post-buckling behaviour of composite stiffened structures, skin-stringer separation is arguably one of the most important failure modes, due to both the severity when it occurs and the interactions with internal damage that make it critical for damage tolerance. The failure originates from the large out-of-plane displacement exhibited by the skin, causing high stresses at the skin-stringer interface, leading to separation in an often unstable manner. The inherent ductility and higher toughness of thermoplastic composites compared to thermosets should lead to a higher resistance to skin-stringer separation. However, it remains unclear whether this is the case due to a noticeable research gap on thermoplastic composites. The primary emphasis of research on thermoplastic composites has been on manufacturing and resulting performance, with very limited research on the prediction of post-buckling behaviour and failure analysis. The difference in material properties and manufacturing techniques between thermoplastics and thermosets is expected to result in different structural behaviour, with a more pronounced difference in the post-buckling field. The differences in failure behaviour are evident from research on coupon levels, which raises concerns about the applicability of analysis methods originally developed for thermosets.

1.3 DISSERTATION OUTLINE

The main objective of the research presented in this thesis is to develop a combined experimental and numerical methodology to investigate the post-buckling and skin-stringer separation behaviour of thermoplastic composite stiffened structures. The research covers post-buckling analysis of sub-component and component structures, the design of representative test panels, imperfection sensitivity studies for damage tolerance, damage analysis, and investigates two different stiffener designs resulting from different manufacturing processes. The work in this thesis intends to close the knowledge gap on thermoplastic composites in post-buckling, and contribute to the push for sustainable primary structures designed to operate within the post-buckling field.

The thesis comprises four chapters directly based on scientific journal papers, followed by a conclusion and recommendation chapter. The chapters can be read independently and incorporate a literature review. Hence, the thesis introduction omits a literature review. The thesis is structured as presented in Figure 1.3, followed by a concise introduction for each chapter.

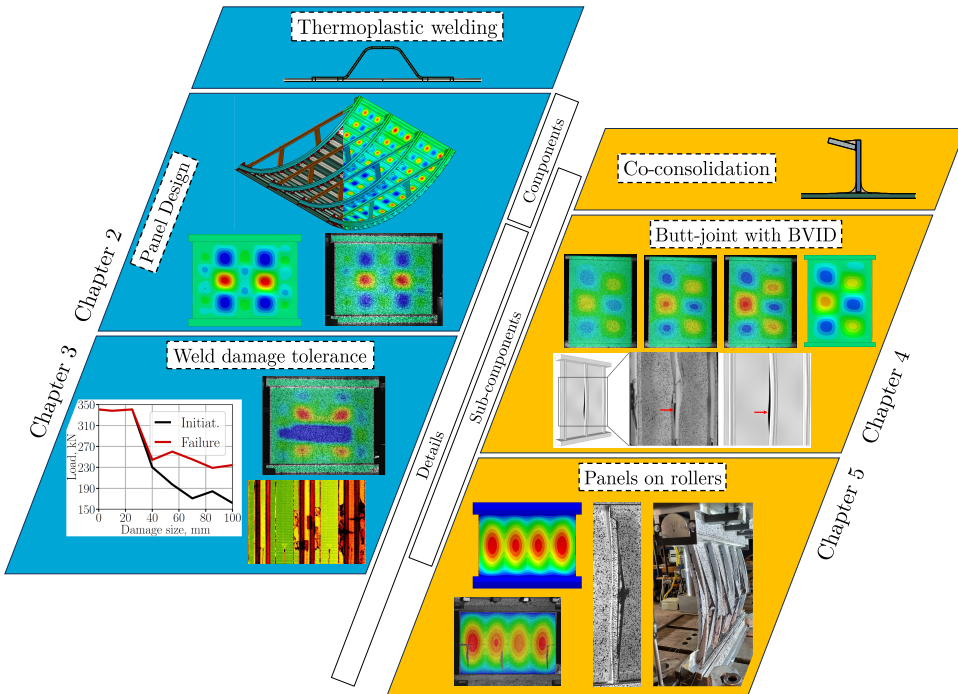


Figure 1.3: Dissertation outline.

Chapter 2

A three-stringer panel with omega stringers and conduction welded joints is designed with the aim of duplicating the structural behaviour of the STUNNING fuselage keel section. This section is considered critical due to its vulnerability to impact damage and low skin thickness. The design considerations are the post-buckling and failure behaviour, besides testing and manufacturing constraints. The strength of the conduction welded joint is assessed by a numerical and experimental methodology, allowing pristine joints to be modelled with the virtual crack closure technique. Two panels, manufactured by project partners Netherlands Aerospace Centre (NLR) and GKN Fokker, are tested until final failure.

Chapter 3

The three-stringer omega panels are further analysed, with the investigation concentrating on the damage tolerance of the conduction welded joints in post-buckling. Three panels with initial damage are designed based on an initial damage size and location sensitivity study. Two panels have one initial damage and one panel has two initial damages, and they are compared to a pristine panel. The initial damage consists of a foil inserted at the skin-stringer interface before welding. The sensitivity study is extended to include geometrical imperfections as measured by digital image correlation, to further evaluate interactions between imperfections and damage in post-buckling. Then, the four panels are tested until failure and compared to the numerical analysis.

Chapter 4

Two thermoplastic stiffened panels featuring three stringers with a butt-joint and angled cap, designed and manufactured by GKN Fokker, are analysed and tested. The panels incorporate initial damage at the middle skin-stringer interface, approximating barely visible impact damage. The numerical analysis includes geometrical imperfections and the virtual crack closure technique to model skin-stringer separation in the interface between the skin and the short fibre filler of the butt-joint. The test results are analysed in detail, emphasising the crack growth behaviour in post-buckling and the final failure behaviour, and compared to the numerical simulations.

Chapter 5

Curved multi-stringer panels with butt-joint and roller boundary conditions are examined in post-buckling by experimental tests and numerical analysis. The rollers approximate simply-supported boundary conditions, which allows for a better representation of loading conditions in flight. The roller boundary conditions are modelled with three different approaches to explore the effect of varying levels of modelling complexity. Numerical analyses are executed, including material damage, damage evolution and skin-stringer separation. Two panels are tested, one with barely visible impact damage in one stringer and one in pristine condition.

2

DESIGN, ANALYSIS AND TESTING OF THERMOPLASTIC WELDED STIFFENED PANELS TO INVESTIGATE SKIN-STRINGER SEPARATION IN POST-BUCKLING

Thermoplastic composite three-stringer panels with omega stiffeners and conduction welded joints are designed, analysed and tested until final failure to investigate the performance of the welded joint in post-buckling. The three-stringer panels are designed to be structurally representative of the fuselage demonstrator of the Clean Sky 2 project STUNNING. A simplified model of the fuselage keel section is analysed by finite element analysis, using the virtual crack closure technique to model skin-stringer separation of the welded joint. The post-buckling and skin-stringer separation behaviour of the fuselage section is then adopted as the reference for the design of the three-stringer panels. Two panels are then tested. The test setup utilises digital image correlation to measure the deformation of the panels, and a high-speed camera to capture the final failure mode. The panels failed in post-buckling due to the separation of the middle stringer, with unstable separation growth followed by separation of the outer stringers and then stringer fracture. The numerical analysis of the panels, with geometrical imperfections included, is able to predict the structural behaviour accurately, with only minor differences in buckling shape and separation behaviour.

2.1 INTRODUCTION

The aeronautical field has shown an increase in research and development of thermoplastic composite materials. The use of thermoplastic composites can aid in the sustainability of aeronautical structures, and in decreasing the manufacturing costs [6, 7]. It offers possibilities for a wide range of manufacturing techniques, such as thermoplastic welding [9] and co-consolidation processes [3, 4]. Other advantages are high toughness, recycle possibilities, long shelf life and chemical resistance [10].

Aeronautical composite structures usually consist of a skin with stiffening elements, and can present buckling under compression and shear loads. Weight savings could be achieved by allowing the structures to buckle below the ultimate load, which necessitates an increased understanding of the post-buckling and failure behaviour, but the failure of composite structures is difficult to predict due to the complexity and catastrophic nature [11].

In the post-buckling field of stiffened structures, the skin shows large out-of-plane displacement which causes high stresses at the interface between the skin and stringer. These high stresses can cause skin-stringer separation [12]. The majority of research on skin-stringer separation has been conducted on thermoset composites [13–15], and only limited research is available regarding thermoplastic composites [16]. Thermoplastics show higher fracture toughness compared to the more brittle thermoset materials, as demonstrated by Reeder [17], which can highly influence the skin-stringer separation behaviour.

The focus of the research field on thermoplastic composite stiffened structures has been primarily on manufacturing and testing, with limited research on predicting buckling and post-buckling behaviour. Flanagan et al. [18] compared joining techniques, namely induction welding and adhesive bonding, using press-formed stringers. Peeters et al. [19] designed and manufactured a thermoplastic section omega-shaped stringer. Oliveri et al. [20] designed, manufactured and tested a wingbox, which utilised laser-assisted automated tape placement process with winding and in-situ consolidation.

Tijs et al. [9, 10] evaluated conduction welded joints in single lap shear specimens and characterised inter-laminar behaviour considering fiber bridging and R-curve effects, both experimentally and numerically. Brito et al. [21, 22] investigated ultrasonic welded single lap shear specimens, and the effect of misaligned adherents and how to improve process efficiency and weld quality.

Skin-stringer separation has been researched on stiffened structures with both blade stringers and omega stringers, mainly made of thermoset composites [23, 24]. Single stringer specimens with a blade stringer were investigated by Orifici et al. [25] in both pristine and damaged states with a debond. The panels failed in compression due to skin-stringer separation in post-buckling, with the pristine panels collapsing immediately at the start of separation, and the pre-damaged panel collapsing after debond growth. The experimental data of Orifici et al. [25] was used for validation by Riccio et al. [26], who presented a numerical procedure for skin-stringer separation using both Virtual Crack Closure Technique (VCCT) and Cohesive Zone Method (CZM). Multi-stringer panels with blade stringers were designed and analysed by Degenhardt et al. [27], and the experimental data was used for validation of a numerical prediction by Orifici et al. [28]. The post-buckling behaviour was difficult to correlate with the experimental data, due to

the geometrical imperfections highly influencing the post-buckling shape.

Bisagni et al. [29] designed Single-Stringer Compression Specimens (SSCS) by analysis for the investigation of skin-stringer separation of stiffened structures with omega stringers. The numerical methodology included CZM for skin-stringer separation and a continuum damage model for crippling of the omega stiffeners. Specimens with and without artificial damage were tested, and the numerical prediction achieved good correlation. Vescovini et al. [13] analysed the failure behaviour of the SSCS with a simplified model and introduced a global/local damage approach. The fatigue behaviour of SSCS was analysed numerically by Raimondo et al. [30] with a VCCT-based approach for skin-stringer separation. Single-stringer specimens with an initial delamination were tested in fatigue by Paz et al. [31], investigating the effect of different load levels and load ratios. A skin-stringer separation study by Kootte [32] used single-stringer specimens, but instead of in-plane loading, out-of-plane displacement was applied directly to the skin to approximate the post-buckling shape.

This research is part of the STUNNING project, which designed and manufactured the lower half of a thermoplastic multi-functional fuselage demonstrator [6, 7]. The fuselage makes use of manufacturing techniques such as press-forming, compression moulding and thermoplastic welding of several critical joints. In this paper, a three-stringer panel is designed with the goal of approximating the structural behaviour of the fuselage keel section, as it is considered the critical section due to its low skin thickness and susceptibility to impact damage, for instance, by tool drops. The design of the panel is conducted with the objective of showing similar structural and failure behaviour and taking into account manufacturing and testing constraints. A numerical and experimental methodology is developed to evaluate the strength of the conduction welded joint between skin and stringer in post-buckling. Two panels, of which the skin is manufactured by NLR - Netherlands Aerospace Centre, and the conduction welding of the stringers to the skin is performed by GKN Fokker, are tested until collapse and analysed with Abaqus.

2.2 THERMOPLASTIC FUSELAGE SECTION

The lower half of the fuselage of the STUNNING project is shown in Figure 2.1. The keel section is considered as the area of interest, due to its low skin thickness, and is highlighted in red. A fuselage section approximating the keel section is modelled and shown in Figure 2.2. The fuselage section is modelled up to the cargo beams and includes the vertical beams, frames and clips. The geometries and joining methods used for the beams, frames, brackets and clips are simplified to lower the complexity of the models, and because these parts are not of interest in this research. The total length of the section is 2005 mm, the total width is 2664 mm, the outer radius is 1926 mm, the stringer pitch is 212 mm, and the frame spacing is 635 mm. The omega stringer geometry is reported in Figure 2.3.

The skin and stringers are made of Toray CETEX TC1225 T700/LM-PAEK 194 gsm with a nominal ply thickness of 0.184 mm. Properties of a similar material, Toray CETEX TC1225 T700/LM-PAEK 145 gsm, are used for the analysis with a ply thickness of 0.184 mm, and are reported in Table 2.1 [33]. The skin layups of the fuselage section are also simplified to only two different layups, a 12 ply layup in the middle nine bays, and a 16 ply layup for the two outer bays on each side of the section. The stringers have a 9 ply layup.

The layups are reported in Table 2.2.

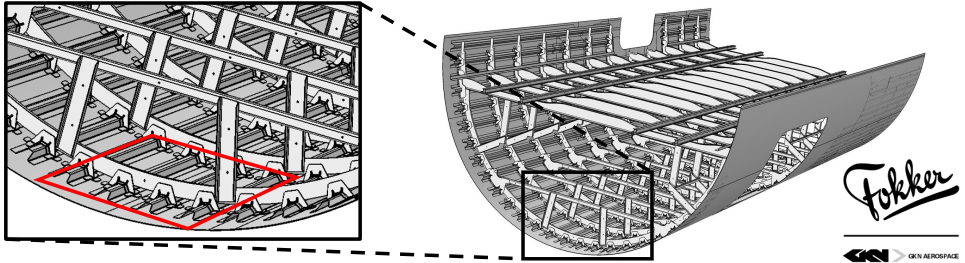


Figure 2.1: Lower half of the STUNNING Multifunctional Fuselage Demonstrator, with the keel section highlighted [6, 7].

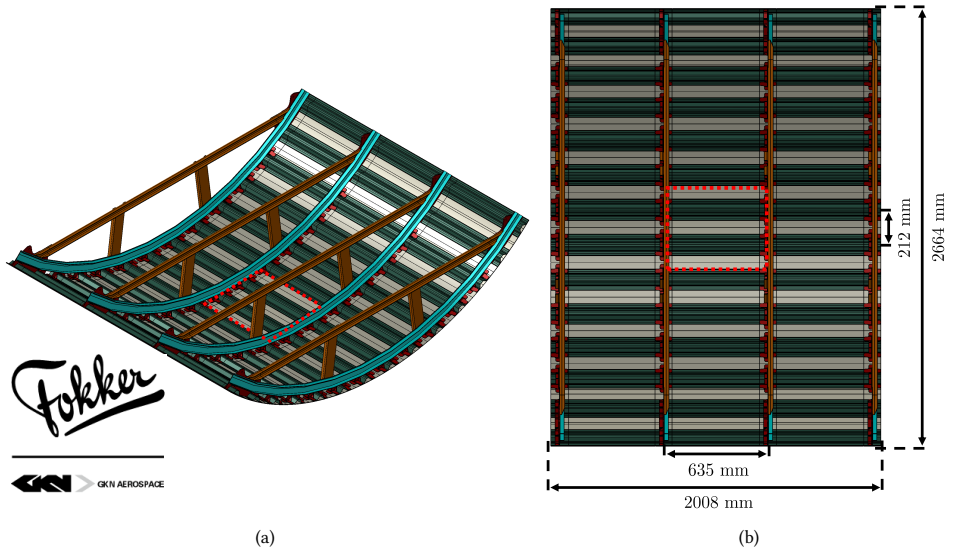


Figure 2.2: Fuselage section with highlighted area of interest: (a): iso-view; (b): top-view.

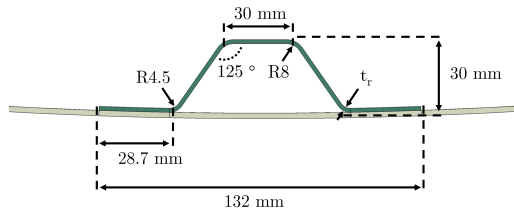


Figure 2.3: Omega stringer geometry.

Table 2.1: T700/LM-PAEK Toray CETEX TC1225 material properties [33].

E_{11} [MPa]	E_{22} [MPa]	ν_{12} [-]	G_{12} [MPa]	F_1^t [MPa]	F_1^c [MPa]	F_2^t [MPa]	F_2^c [MPa]	F_{12} [MPa]
116800	9100	0.36	4100	2442	1250	94	212	99

Table 2.2: Layups of fuselage section.

	Layup	Thickness (mm)
Skin 12	$[-45/45/0/90/-45/45]_s$	2.208
Skin 16	$[-45/45/0/90/0/90/0/90/-45/45]_s$	2.944
Stringer	$[45/0/-45/0/90]_s$	1.656

2.3 NUMERICAL ANALYSIS OF FUSELAGE SECTION

The numerical analyses are performed using the commercial software Abaqus 2021 [34]. The fuselage section is analyzed with dynamic implicit analysis, with non-linear geometry activated. The total time-step is 1 s with an initial and maximum time-step of 0.01 s, and a minimum time-step of $1e-08$ s.

The fuselage is loaded in bending using a linear displacement field that applies compression to the fuselage section, with the bottom of the section in maximum compression, as illustrated in Figure 2.4. Boundary conditions applied to the free edges of the fuselage section, which are the edges of the skin and frame ends, constrain the circumferential degree of freedom, as illustrated in Figure 2.5, and leave the radial degree of freedom unconstrained.

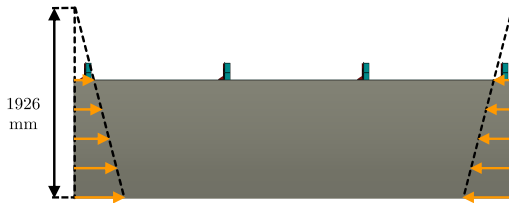


Figure 2.4: Side-view of fuselage section model showing bending load-case.

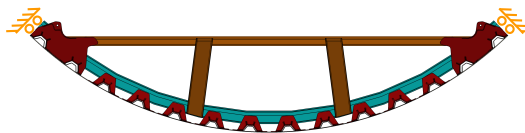


Figure 2.5: Cross-section of fuselage section showing circumferential constraint.

The area of interest of the fuselage section is in between the two middle frames and includes the middle three bays, as shown in Figure 2.2. The area of interest has a mesh size of 2.5 mm, while the adjacent areas are meshed coarser when feasible with a mesh size of

5 mm to improve computational efficiency. The clips and brackets have a mesh size of 5 mm, and the vertical strut and cargo beam have a mesh size of 10 mm. The laminated parts utilise SC8R continuum shell elements, and the brackets and clips of the fuselage section utilise the C3D10 tetrahedral element.

2

The joints between the separate geometries are modelled with three different techniques, namely shared nodes, rigid body ties and the Virtual Crack Closure Technique (VCCT) [35, 36]. Parts with mismatching meshes, such as the frame, vertical strut, clips, brackets and cargo beam, are modelled with rigid body ties. VCCT is applied for the welded joint of the two middle stringers in the area of interest, while the welded joints of the adjacent areas adopt shared nodes.

It is assumed that there is only crack growth in the skin-stringer interface, with no crack migration into other interfaces, to lower the complexity of the model. This assumption is based on the unwelded regions on both sides of the weld, which makes it more likely to separate the welded interface instead of the interlaminar interfaces. The VCCT definition utilizes the Benzeggagh-Kenane (BK) criterion for mode-mixity, in which the critical equivalent strain energy release rate G_{equivC} and the equivalent strain energy release rate G_{equiv} are calculated with Equation 2.1 and Equation 2.2, respectively. The critical equivalent strain energy release rate is calculated using the fracture toughness G_{IC} , G_{IIC} and G_{IIIC} of the interface and the BK parameter η . G_{IC} , G_{IIC} and η are based on a similar material AS4/PEEK [37], which utilises a matrix material from the same thermoplastic polymer family of polyaryletherketones, and the properties are reported in Table 2.3. It is assumed that G_{IIC} and G_{IIIC} are equal. The strain energy release rate is calculated for the three different modes, G_{I} , G_{II} and G_{III} , at each node and the sum is the equivalent strain energy release rate. The fracture criterion is reported in Equation 2.3. It allows a node to be released at the crack tip when G_{equiv} divided by G_{equivC} is higher than 1.

$$G_{\text{equivC}} = G_{\text{IC}} + (G_{\text{IIC}} - G_{\text{IC}}) \left(\frac{G_{\text{II}} + G_{\text{III}}}{G_{\text{I}} + G_{\text{II}} + G_{\text{III}}} \right)^\eta \quad (2.1)$$

$$G_{\text{equiv}} = G_{\text{I}} + G_{\text{II}} + G_{\text{III}} \quad (2.2)$$

$$f = \frac{G_{\text{equiv}}}{G_{\text{equivC}}} \geq 1.0 \quad (2.3)$$

Table 2.3: Fracture properties of skin-stringer interface [37].

G_{IC} [kJ/m ²]	G_{IIC} [kJ/m ²]	G_{IIIC} [kJ/m ²]	η [-]
0.969	1.719	1.719	2.284

A default fracture tolerance of 0.2 is used for the VCCT definition, with an unstable crack growth tolerance of 1. The unstable crack growth tolerance can improve convergence and lower computational time. It allows the analysis to release multiple nodes ahead of the crack-tip and allows the analysis to use larger time steps during unstable crack growth. While the default unstable crack growth tolerance in Abaqus is infinity, in this study it is chosen to limit this tolerance to have a larger number of data-points during unstable

crack growth events. A contact stabilisation factor of $1e-4$ is used to stabilize contact, and node-to-surface contact discretization is implemented with the stringer side as master surface and skin side as slave surface.

One of the main benefits of VCCT is that it allows for a coarser mesh to model skin-stringer separation, in comparison to other methods. The downside is that a pre-crack is required to utilise VCCT, which generally limits the use of this method to structures with initial damage. This downside can however be overcome in this study due to the geometry of the conduction welded joint. There are small unwelded areas adjacent to the joint, as shown in Figure 2.6, which are considered as a pre-crack. The weld is initially assumed to be 21 mm wide, based on visual inspection of an early manufacturing sample. This weld width of 21 mm is used for the fuselage section analysis and the preliminary panel analysis.

The analysis includes first-ply failure criteria, to investigate if material failure happens before skin-stringer separation. The criteria of Hashin, Tsai-Wu and Tsai-Hill are included. The strength properties are reported in Table 2.1 [33].

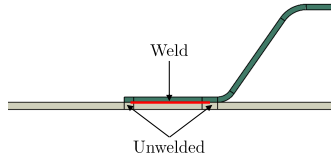


Figure 2.6: Weld between skin and stringer.

The buckling shape of the fuselage section is investigated. Contour plots of the out-of-plane displacement are shown at different levels of longitudinal bending, and consequentially different maximum longitudinal displacement, in Figure 2.7. The contour plots show the out-of-plane radial displacement of the fuselage section and a close-up of the area of interest, and the interface state of the two stringers in the area of interest. The area of interest consists of the middle three bays and two stringers in between the two middle frames and has the highest level of compression. This area also limits itself to the two stringers and adjacent bays where skin-stringer separation is modelled with VCCT. In the contour plots of the area of interest, the interface state of the welded flange is blue for the intact interface and red for the pre-crack and separation. The stringers are hidden, and an outline of the stringer flanges is shown in black, to allow seeing the radial displacement in the bay and underneath the stringer.

At a maximum applied longitudinal displacement of 5.36 mm, the skin in the middle of the section in between the two middle frames starts to buckle with a five half-wave buckling shape (Figure 2.7(a)). The half-waves in the bay have a much higher radial displacement compared to the half-waves underneath the stringer, with the half-waves at the top and bottom barely visible. The half-wave length underneath the stringer and in the bay is similar, but the sign of the radial displacement is inverted for the adjacent waves in the circumferential direction. The buckling shape continuously evolves, with the remaining bays in between the middle frames displaying an initial three half-wave buckling shapes followed by a five half-wave buckling shape (Figure 2.7(b)). At a maximum longitudinal displacement of 8.23 mm (Figure 2.7(c)) all bays have buckled, with the top and middle

2

bays showing mostly three half-wave buckling shapes, with some of the bays starting to form a fifth half-wave.

At a maximum displacement of 8.24 mm (Figure 2.7(d)), failure due to skin-stringer separation starts, with separation developing from underneath the stringer. It is seen that the outward half-waves in the radial direction in the bay and underneath the stringer start to connect, which is called tunnelling. Separation starts almost simultaneously in two stringers, with similar elliptical crack front shapes. Once separation starts, it is unstable, and the stringer totally separates in one separation event.

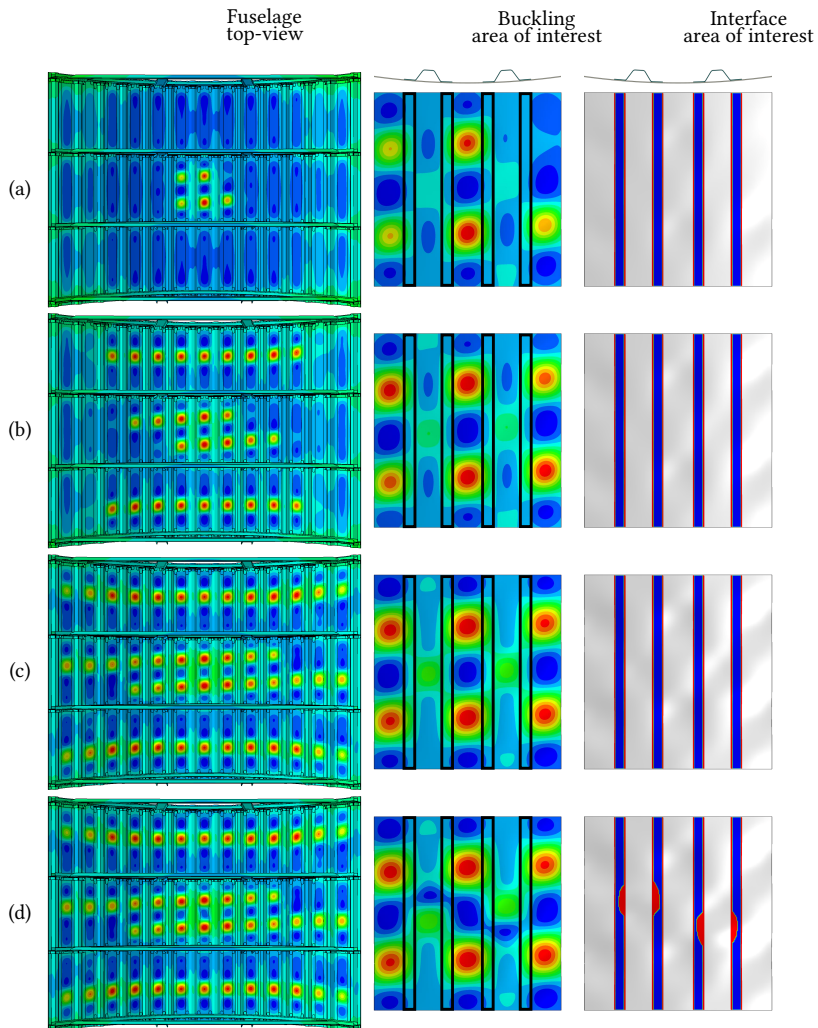


Figure 2.7: Radial displacement of fuselage section, radial displacement and interface state of area of interest, at different levels of bending with a longitudinal displacement of: (a) 5.36 mm; (b) 6.27 mm; (c) 8.23 mm; (d) 8.24 mm.

2.4 PANEL DESIGN AND MANUFACTURING

The structural behaviour of the STUNNING fuselage keel section is the reference behaviour for the design of the three-stringer panels, with the buckling and failure behaviour as the main focus. The design also needs to take manufacturing and testing constraints into account. The three stringers allow for bay buckling on both sides of the middle stringer, such that the structural behaviour of the middle stringer can be representative of the fuselage section.

The panels have the same stringer pitch and nominal stringer geometry as the STUNNING fuselage lower half, shown in Figure 2.2 and Figure 2.3, respectively. The nominal width and length of the panels are equal to 556 mm and 500 mm, respectively. The panel length corresponds to the maximum possible welding length available at the time of the design. The geometry of the three-stringer panel is shown in Figure 2.8.

The panels are made of the same CF/LM-PAEK material as used in the STUNNING fuselage, of which the material properties are reported in Table 2.1 [33]. The skin layup is different compared to the keel section of the STUNNING fuselage to achieve a more conservative stress field in post-buckling, while the stringer layup is the same as in the STUNNING fuselage. The layups are reported in Table 2.4.

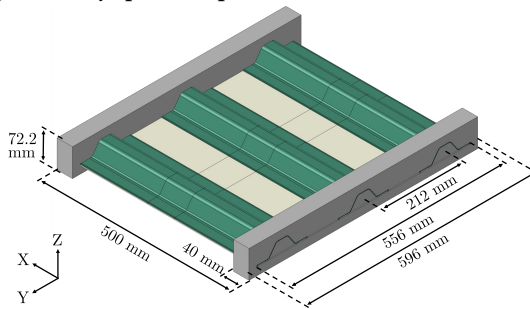


Figure 2.8: Three-stringer panel.

Table 2.4: Layups of three-stringer panel.

	Layup	Thickness (mm)
Skin	$[-45/45/90/0/90/0]_s$	2.208
Stringer	$[45/0/-45/0/90]_s$	1.656

The structural behaviour of the three-stringer test panel without imperfections is analyzed and compared to the reference behaviour of the fuselage section. The preliminary analysis of the panel is conducted without any imperfections and considering a 21 mm weld width.

A displacement boundary condition is used for the panel to apply the load case of pure compression. A reference point is positioned on each loading face of the model, with a rigid body tie to the loading face. One reference point is clamped, while the other reference point is constrained in all degrees of freedom except for the longitudinal displacement. A longitudinal displacement of 2.5 mm is applied, resulting in a displacement rate of 2.5 mm/s.

The laminated parts of the panel use a mesh size of 2.5 mm, and a mesh size varying between 2.5 mm and 10 mm is used for the potting material to improve computational efficiency. The laminated parts consist of SC8R continuum shell elements, and the C3D8R solid element is applied for the potting material. VCCT is utilized for the test panel in all welded joints in between the potting, while the geometries inside the potting material adopt shared nodes.

The load-displacement graph of the three-stringer panel is shown in Figure 2.9. The linear stiffness before buckling is 248.2 kN/mm. Local buckling occurs at an approximate load of 192 kN and displacement of 0.78 mm. At 338 kN the panel presents a small buckling shape change. Panel failure occurs at a load of 370 kN and displacement of 1.65 mm due to skin-stringer separation.

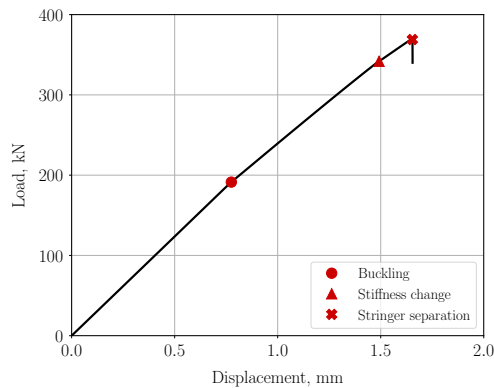


Figure 2.9: Load-displacement curve of the panel preliminary analysis.

The panel displays a three half-wave buckling shape, as reported in Figure 2.10(a), with one half-wave in an inwards direction and two half-waves in an outwards direction. The average half-wave length of the panel and the fuselage section is very similar. At a load of 338 kN, the buckling shape changes underneath the stringer, as shown in Figure 2.10(b).

Two main aspects of the skin-stringer separation behaviour of the fuselage section and of the three-stringer panel are compared. The first aspect is the out-of-plane deformation when skin-stringer separation occurs, shown in Figure 2.11(a) and Figure 2.11(c) for the fuselage and the panel, respectively. The second aspect is the shape and location of the crack front, shown in Figure 2.11(b) and Figure 2.11(d) for the fuselage section and the panel, respectively. To compare the structural behaviour of the fuselage section and the panel, an area with a similar size and similar buckling shape is selected on each structure and highlighted with red dashed squares. During separation, both structures show a similar tunnelling behaviour underneath the stringer between inwards half-waves, within the highlighted area. The panel displays two tunnels per highlighted area, while the fuselage section displays one tunnel per highlighted area. The weld interface shows the same difference in the number of failure locations, that can be caused by the difference in boundary conditions. In any case, both the fuselage section and the panel show similar separation behaviour, starting from underneath the stringer and presenting an elliptical crack front.

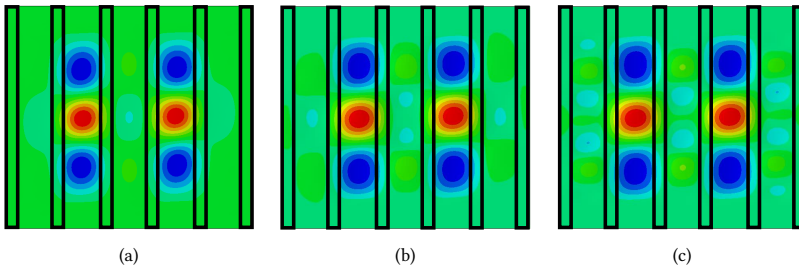


Figure 2.10: Buckling shapes of the panel preliminary analysis: (a) 0.78 mm / 191 kN; (b) 1.48 mm / 338 kN; (c) 1.65 mm / 370 kN.

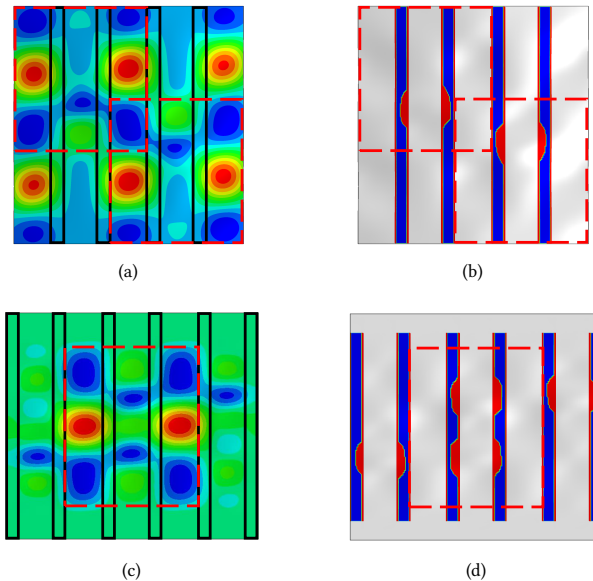


Figure 2.11: Comparison of skin-stringer separation behaviour from the analyses: (a) buckling shape of fuselage section; (b) welded skin-stringer interface state of fuselage section; (c) buckling shape of the panel; (d) welded skin-stringer interface state of the panel.

Two nominally identical three-stringer panels are then manufactured. Project partner NLR - Netherlands Aerospace Centre manufactured the skin by automatic tape laying followed by autoclave consolidation. Project partner GKN Fokker uses conduction welding to join the stringers to the skin. Conduction welding makes use of a heating element, that is pressed on the stringer flange to apply pressure and heat, and weld the stringer flange to the skin. A panel as received is shown in Figure 2.12(a). The panels are then prepared for the tests. The first step consists of casting epoxy potting onto both ends of the panels for load introduction, and then the loading faces are trimmed in a milling machine to minimize loading imperfections. This is followed by attaching strain gauges and wiring. A panel with potting and strain gauges is shown in Figure 2.12(b).

A total of 10 strain gauges are attached, 135 mm from the bottom loading face, and the locations are reported in Figure 2.13. A strain gauge is attached on top of each stringer cap and the bottom of the skin underneath each stringer. Then, strain gauges are attached back to back to the skin in the middle of each bay. The strain measurements are used to determine load imperfections, load distribution and load redistribution due to buckling and failure. The last step of the preparation for the tests consists of applying white paint with black speckles for DIC measurements.

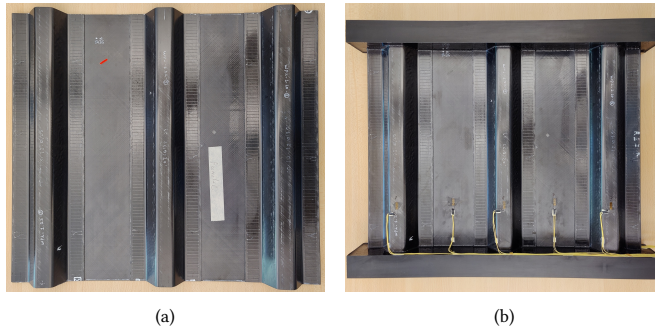


Figure 2.12: Test panels: (a) as received; (b) with potting and strain gauges.

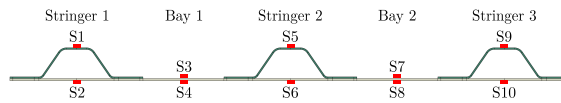


Figure 2.13: Strain gauge locations.

2.5 TEST SETUP

The two three-stringer panels with welded interface are tested at Delft University of Technology using an MTS test machine. The tests are executed to investigate the buckling, post-buckling and skin-stringer separation behaviour of the three-stringer panels, and to validate the numerical analysis.

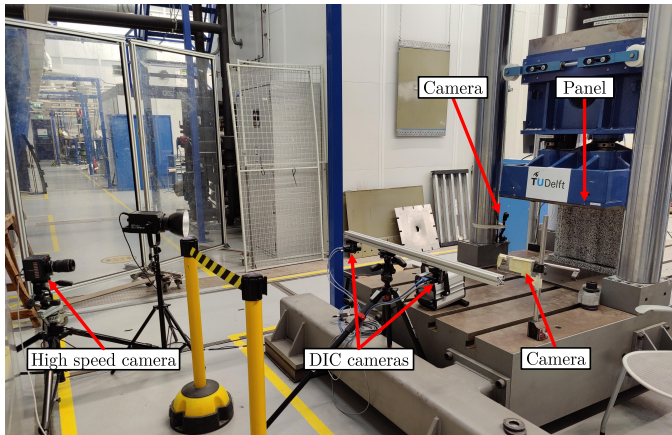
The test panels are placed in between the compression plate and the base, and a pre-load of 2 kN is applied. The loading rate is 0.1 mm/min until final failure, after which the loading stops automatically. The test setup is shown from the stringer-side of the panel in Figure 2.14(a) and a top-view illustration of the test setup is shown in Figure 2.14(b).

Three Laser Distance Sensors (LDS) are used to measure the longitudinal displacement of the compression plate in three different locations, which also allows to determine if a loading imperfection is occurring.

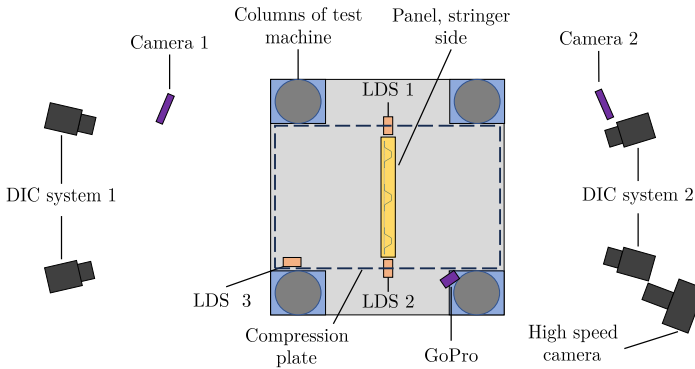
The displacement field is measured from both the stringer and skin side by two DIC systems. Both systems use two 5 MP cameras, and post-processing is done using VIC3D 8. This measurement allows to determine the post-buckling shape of the panels from the out-of-plane displacement, and the longitudinal shortening from the in-plane displacement of the potting.

The strain measurements, the load from the test machine, the displacement measurement by LDS and the pictures for DIC are recorded every 3 seconds, leading to approximately 500 data points per test.

Three additional cameras are used to capture the test. A GoPro is placed on one of the sides of the panel to capture the stringer-side of the panel for a close-up of any buckling shape changes or crack growth events. Two cameras are placed further away, one on the stringer-side and one on the skin-side of the panel, to capture the whole panel and test setup. A high-speed camera is used to capture the final failure from the stringer-side of the panels, at 10000 fps.



(a)



(b)

Figure 2.14: Test setup: (a) test setup photo stringer side; (b) test setup schematic top-view.

2.6 PANEL MEASUREMENTS

The global shape of the three-stringer panels is measured from the skin-side before the start of the test campaign using DIC.

The geometrical imperfections of panels 1 and 2 are shown in Figure 2.15, with the imperfection aligned with the z-axis of the axis system reported in Figure 2.8. The panels show a similar curved imperfection in the transverse direction, with the edges of the panel curved inwards. The total magnitude of the imperfections is 11.76 mm. The imperfection has a slight skew, rotated anti-clockwise. The orientation of the skew is likely caused by the outer -45 ply of the layup. When inspecting the imperfection of the panels more closely, it can be seen that the largest curvature is in the welding region. The curvature of the panels is most likely caused by the local heating during welding, leading to thermal stresses.

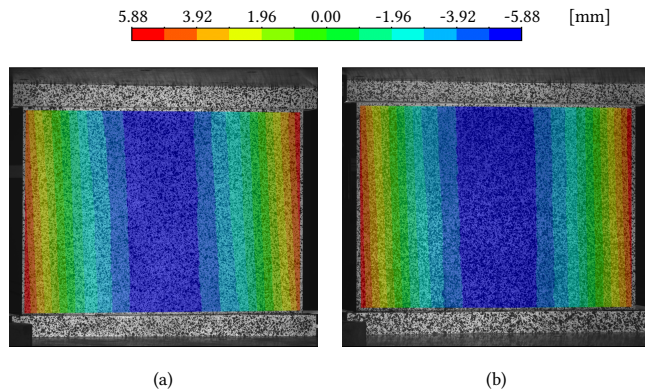


Figure 2.15: Out-of-plane imperfections: (a) panel 1; (b) panel 2.

The thickness of the skin and stringers are measured with a micrometer. The skin is found to be thinner compared to the nominal, with an average thickness of 2.14 mm. The flat sections of the stringers have an average thickness of 1.66 mm which is approximately the nominal thickness. It is however seen that in the middle of the radius from stringer flange to web, the thickness is lower, shown as t_r in Figure 2.3, with an approximate minimum thickness of 1.15-1.20 mm.

The stringer spacing and panel length are also measured. The stringer spacing of panel 2 matches the nominal design of 212 mm. The middle stringer of panel 1 has an average offset of 2 mm from the centre line of the panel and is slightly angled. The panel length is approximately 489 mm for both panels.

The numerical models for panels 1 and 2 are updated to take into account the measurements. In particular, numerical models of the two panels have geometrical imperfections included as measured by DIC. The method to include the measured imperfections is based on including a node file of the imperfection in the analysis [16]. This node file is created by a linear analysis, where the out-of-plane imperfection is applied as a displacement field to the skin. The final shape, which now replicates the out-of-plane imperfection, is outputted as a node file which can be included in further analysis. This node file only transfers the deformation and not the stress field.

The models also include imperfections of laminate thickness and stringer alignment imperfection. The models do not include residual stresses from the manufacturing process, to prevent additional complexity of the models and analysis.

After inspection of the failed test panels, it is found that the weld had a varying weld width which is less wide, with a lower bound of 18 mm in the middle region of the panel. The updated numerical models of panels 1 and 2 are therefore considered with a weld width of 18 mm.

2.7 EXPERIMENTAL AND NUMERICAL RESULTS

The test results of the three-stringer panels are reported in this section and are compared to the results from the numerical analysis performed using the updated analysis.

2.7.1 LOAD VERSUS DISPLACEMENT CURVES

The load measured by the load cell of the testing machine is reported in Figure 2.16, as a function of the average displacement measured by the two LDS. The panels show settling behaviour till approximately 30 kN after which they present a linear stiffness of approximately 240.2 kN/mm and 244.1 kN/mm for panels 1 and 2, respectively, until buckling. Panel 1 starts to locally buckle at an approximate load of 155 kN and panel 2 at a load of 165 kN. In the post-buckling field, panel 1 shows a higher reduction of stiffness compared to panel 2. This is caused by a buckling shape change, which starts gradually at 245 kN and shows a small load drop at 275 kN due to a sudden shape change. Panel 2 does not show any load drops before failure. The panels fail due to skin-stringer separation at a load of 301 kN and 309 kN for panels 1 and 2, respectively, as reported in Table 2.5.

The numerical analyses conducted using dynamic implicit analysis show a stiffness of 244.6 kN/mm and 244.9 kN/mm for panels 1 and 2, respectively. This is a 1.8% and 0.3% difference in comparison with the test results. The numerical analysis of both panels shows buckling at approximately 160 kN, which is a difference of 3.2% and 3.0% for panels 1 and 2, respectively. In comparison to the test results the initial post-buckling stiffness is similar, but at higher loads, the stiffness is over-predicted. The higher over-prediction for panel 1 is caused by smaller load drops due to buckling shape changes that occur at 245 kN and 285 kN. The numerical analysis predicts panel collapse due to skin-stringer separation at a load of 314 kN and 320 kN for panels 1 and 2 respectively, as reported in Table 2.5. This is an over-prediction of 4.3% for panel 1 and 3.6% for panel 2 in comparison to the test results. The difference between the experimental and numerical results can be caused by not taking into account the loading imperfections, the difference in material properties and the slight skew of the middle stringer of panel 1 in the numerical models.

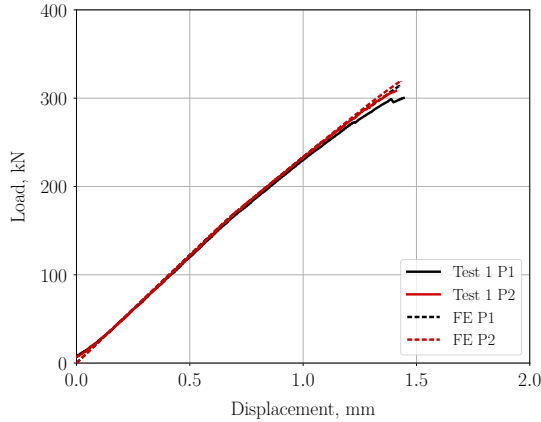


Figure 2.16: Load-displacement curves from tests and numerical analysis.

Table 2.5: Pre-buckling stiffness, buckling load and maximum load from tests and numerical analysis.

	Pre-buckling stiffness			Buckling load			Maximum load		
	Test [kN/mm]	FE [kN/mm]	Diff. [%]	Test [kN]	FE [kN]	Diff. [%]	Test [kN]	FE [kN]	Diff. [%]
Panel 1	240.2	244.6	1.8	155	160	3.2	301	314	4.3
Panel 2	244.1	244.9	0.3	165	160	3.0	309	320	3.6

2.7.2 LOAD VERSUS STRAIN CURVES

The strains measured on the caps of panels 1 and 2 are shown in Figure 2.17(a) and Figure 2.17(b), respectively. On panel 1 they show diverging behaviour initially, most likely due to loading imperfections, and a similar gradient until the buckling shape changes and the skin and stringer separate. The strains in the caps of panel 2 diverge less in comparison to panel 1, with stringers 1 and 2 showing similar strains in pre-buckling and stringer 3 showing lower strains. In post-buckling, it is seen that the strains in stringers 2 and 3 show similar gradients, while the strains in stringer 1 show a higher gradient. The numerical analysis predicts the strains in the stringers reasonably well, with the main difference being the initial loading.

The strains measured at the bottom of the skin underneath the stringers of panels 1 and 2 are shown in Figure 2.18(a) and Figure 2.18(b), respectively. The strains of panel 1 show only minor differences in pre-buckling, with slightly lower strains underneath stringer 3. In post-buckling, the strains start to diverge, with sudden drops and increases of strain due to buckling shape changes and a separation event. The strains in the stringers of panel 2 show a slightly larger difference in pre-buckling, with higher strains underneath stringer 1. In post-buckling, the strains underneath stringers 1 and 2 converge, with lower strains underneath stringer 3. No sudden changes in strains are seen in comparison to panel 1. The numerical analysis predicts the pre-buckling strains well. For panel 1 the predicted strains diverge less in post-buckling in comparison to the test result, and the jumps in strain happen at different load levels. For panel 2 the post-buckling strains are predicted

more accurately, with the strains being under-predicted close to the failure load.

The strains measured back-to-back in bay 1 of panels 1 and 2 are shown in Figure 2.19(a) and Figure 2.19(b), respectively. The strains in pre-buckling of panel 1 show a small difference, which indicates a small bending component. In post-buckling, the strains diverge due to high levels of bending, with a small jump when the buckling shape of bay 2 changes and a large jump when bay 1 shows a buckling shape change. The strains in bay 1 of panel 2 present a higher bending component, both before buckling and in the post-buckling field, with no sudden jumps. Close to the failure load, it is also seen that the strain gradient changes sign. The numerical analysis results of panel 1 show close agreement in pre-buckling strain gradient compared to the test, but with an opposite bending component. In post-buckling, the strains diverge more in comparison to the test results, which corresponds to a higher bending component, and the jumps in strain are less severe and at different load levels. These differences can be accounted to differences in buckling shape between the test and numerical analysis. The numerical analysis results of panel 2 show a closer agreement with the test, both in pre-buckling and post-buckling.

The strains measured back-to-back in bay 2 of panels 1 and 2 are shown in Figure 2.20(a) and Figure 2.20(b), respectively. The strains in bay 2 of panel 1 show similar behaviour as bay 1, with sudden changes in strains in the post-buckling field due to the buckling shape changes. The strains in bay 2 of panel 1 are similar to bay 1, with a large bending component and no sudden changes. The numerical analysis predicts the strains in bay 2 of panel 1 well in pre-buckling and in the post-buckling field until buckling shape changes start to occur. For bay 2 of panel 2, the strains are predicted well, with an under-prediction of the bending component in both pre-buckling and post-buckling.

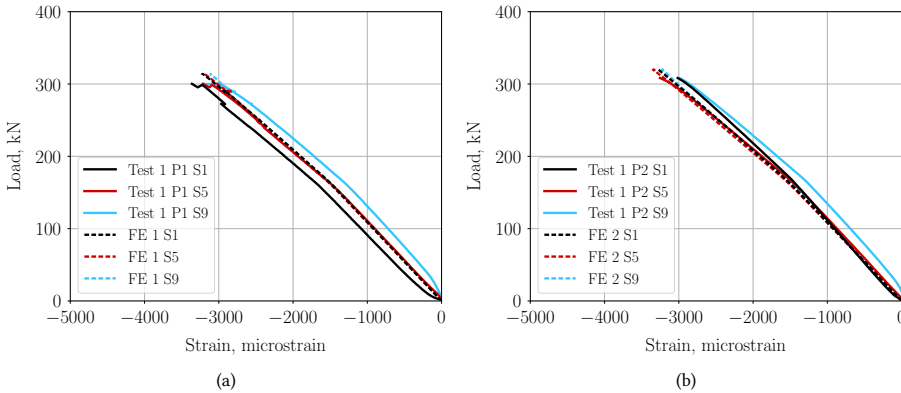


Figure 2.17: Experimental and numerical compressive strains in stringer caps: (a) panel 1; (b) panel 2.

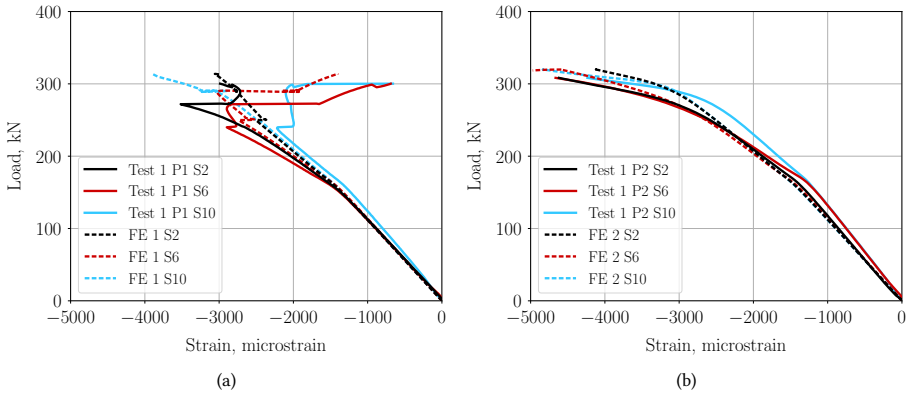


Figure 2.18: Experimental and numerical compressive strains in the skin below stringer: (a) panel 1; (b) panel 2.

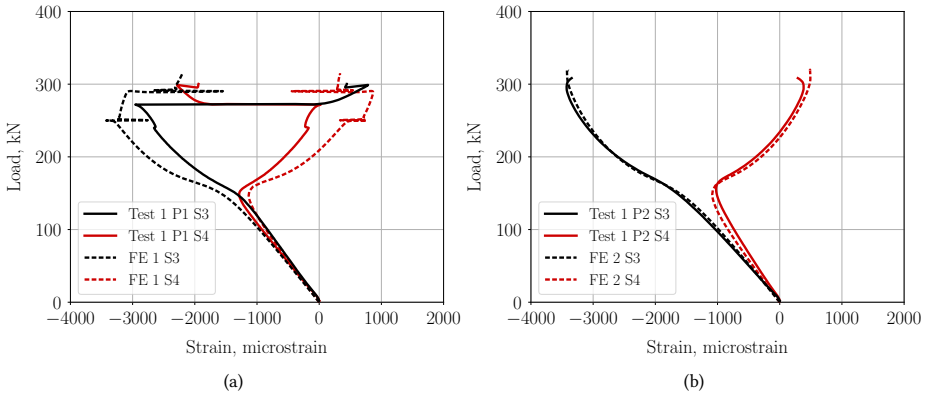


Figure 2.19: Experimental and numerical compressive strains in the skin of bay 1: (a) panel 1; (b) panel 2.

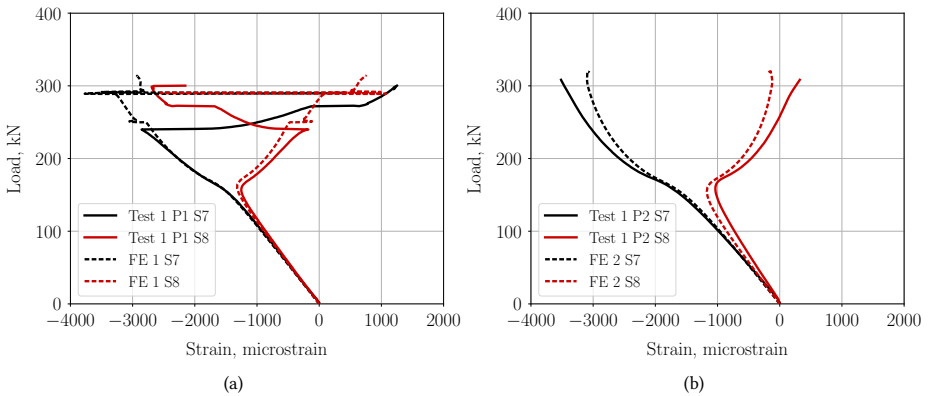


Figure 2.20: Experimental and numerical compressive strains in the skin of bay 2: (a) panel 1; (b) panel 2.

2.7.3 EVOLUTION OF BUCKLING SHAPE

The out-of-plane displacement from the DIC measurement and the numerical analysis of panels 1 and 2 are reported in Figure 2.21 and Figure 2.22, respectively, highlighting the buckling shape and the evolution of the shape in the post-buckling field. Positive displacement corresponds to inwards direction, and negative displacement corresponds to outwards direction, in line with the axis system reported in Figure 2.8.

Panel 1 shows an initial three half-wave buckling shape, with a slight skew in the vertical half-wave position. At 245 kN a buckling shape change occurs in bay 2 with a fourth half-wave at the bottom of the bay, and at 273 kN another buckling shape change happens with a fourth half-wave at the bottom of bay 1. After the buckling shape changes in the bay, the number of half-waves underneath the stringer also increases. At the maximum load, the displacement is higher on the right side of the panel, which is due to a skin-stringer separation event that occurred at 300 kN.

Panel 2 shows a three half-wave buckling shape with no buckling shape change in the bays, and at higher loads the number of half-waves increases underneath the stringer. The three half-wave buckling shape does not show a skew in vertical position of the half-waves as panel 1, which might be due to differences in imperfections. The maximum inwards out-of-plane displacement is similar between panels 1 and 2, but the maximum outwards displacement of panel 2 is higher. The difference in final buckling shape might lead to the small difference in failure load and it can indicate that the four half-wave buckling shape is slightly more critical. Both panels showed an increase in the number of half-waves underneath the stringer, and these half-waves become more prominent in terms of out-of-plane displacement close to the failure load.

The numerical analysis predicts the initial three half-wave buckling shape of both panels 1 and 2. The numerical analysis of panel 1 also shows buckling shape changes in the bay to four half-waves, but the changes occur at higher loads and the fourth half-waves form at the top of the panel. This difference can be caused due to the fact that the stringer alignment imperfections are not taken into account. The numerical analysis of panel 2 is able to predict the post-buckling behaviour well, with the evolution of the half-waves underneath the stringer and no shape changes in the bay. The maximum inwards displacement of panel 1 is lower in the numerical analysis, while the maximum outwards displacement shows good agreement. The maximum inwards and outwards displacement of panel 2 is predicted well, with the outwards displacement being slightly over-predicted.

2.7.4 FINAL FAILURE

The final failure of panels 1 and 2 is captured by the high-speed camera at 10000 fps. Panel 1 shows a skin-stringer separation event in stringer 1 which did not lead to final failure. The location of this separation event is indicated by the blue arrow in Figure 2.23(a). It occurs at a load of 299 kN and causes a load drop to 295 kN. It is visible from the deformation of the flange and web of the stringer, which causes a change in the shadow on the web. The event could also be heard and seen on the normal camera footage and causes a sudden increase in the out-of-plane displacement measured by the DIC. From the camera footage, it appears that the separation starts from underneath the stringer and stops approximately halfway through the stringer flange.

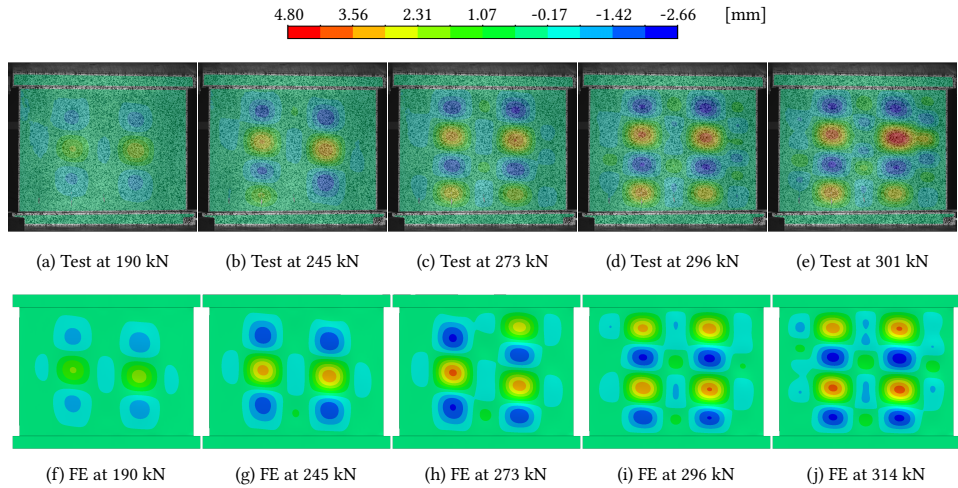


Figure 2.21: Experimental and numerical out-of-plane displacement of panel 1.

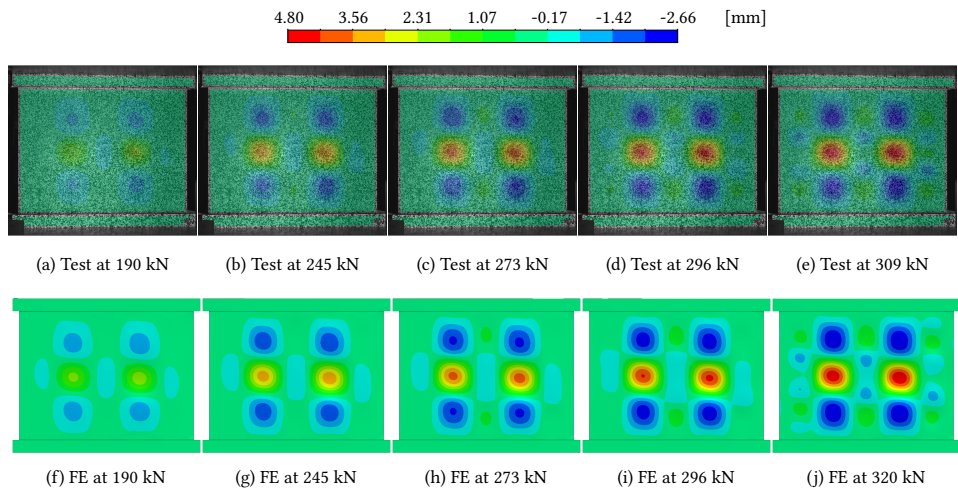


Figure 2.22: Experimental and numerical out-of-plane displacement of panel 2.

The test is then continued until a load of 301 kN where the panel fails due to skin-stringer separation. Final failure starts by separation of the middle stringer, with the first separation location shown by the red arrow in Figure 2.23(a). This separation appears to start from underneath the stringer and grows both in longitudinal direction and width direction towards the bay.

Panel 2 shows final failure at a load of 309 kN due to skin-stringer separation of the middle stringer, as reported in Figure 2.23(d). Separation starts at a different location than panel 1, most likely caused by the different buckling shape, but grows in a similar manner from underneath the stringer.

The numerical results are shown in Figure 2.23(b-c) and Figure 2.23(e-f) for panels 1 and

2, respectively. The figures report the skin of the panels with contour plots of the interface states, where blue means intact interface and red means separation or unwelded regions next to the weld. The numerical analysis predicts that the final failure of panel 1 starts with skin-stringer separation of stringer 1 as shown in Figure 2.23(b-c). The separation grows in longitudinal and width directions with an elliptical crack front. The failure location is similar to the location of the first skin-stringer separation event in the test of panel 1. The numerical analysis of panel 2 predicts that final failure starts with skin-stringer separation of the middle stringer as shown in Figure 2.23(e-f). Separation starts in two locations simultaneously, shortly followed by two other locations, all in the middle stringer with elliptical crack fronts. The failure locations are slightly different compared to what is seen in the test, which can be caused by differences in buckling shape and imperfections.

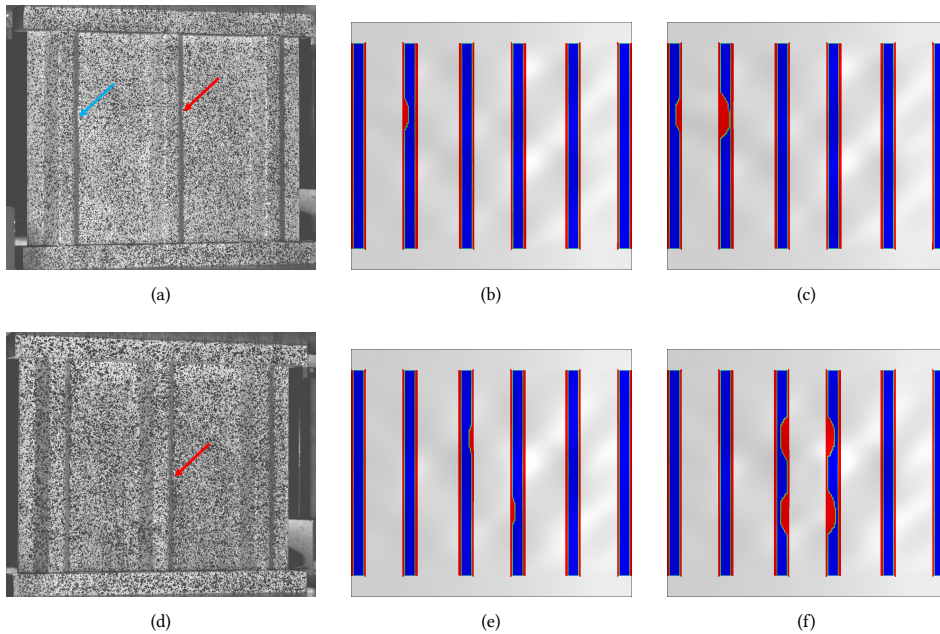


Figure 2.23: Comparison of failure behaviour: (a) start of failure of panel 1 during test; (b) start of failure of panel 1 analysis; (c) propagation of panel 1 analysis; (d) start of failure of panel 2 during test; (e) start of failure of panel 2 analysis; (f) propagation of panel 2 analysis.

The final failure sequence of panel 1 is shown in Figure 2.24. It starts with skin-stringer separation in the right flange of the middle stringer, Figure 2.24(a-b). The separation propagates in outward direction towards the bay, and the left flange also separates with similar behaviour, Figure 2.24(c-d). Separation then starts in the left stringer, first in the right flange, followed by the left flange, Figure 2.24(e-f). This is followed by the fracture of the left stringer, Figure 2.24(g-h), and then of the middle stringer, Figure 2.24(i-j). Lastly, the right stringer separates, Figure 2.24(k-l). The failure sequences occur within approximately 3 ms.

The failure sequence of panel 2 is not reported, as it shows similar behaviour. It starts with skin-stringer separation in the middle stringer, followed by the separation of the left

and right stringers, which happen simultaneously. Then, the middle stringer fractures, closely followed by the fracture of the right stringer.

From the high-speed footage of both panels, it can be concluded that skin-stringer separation is the critical failure mode leading to final failure.

2

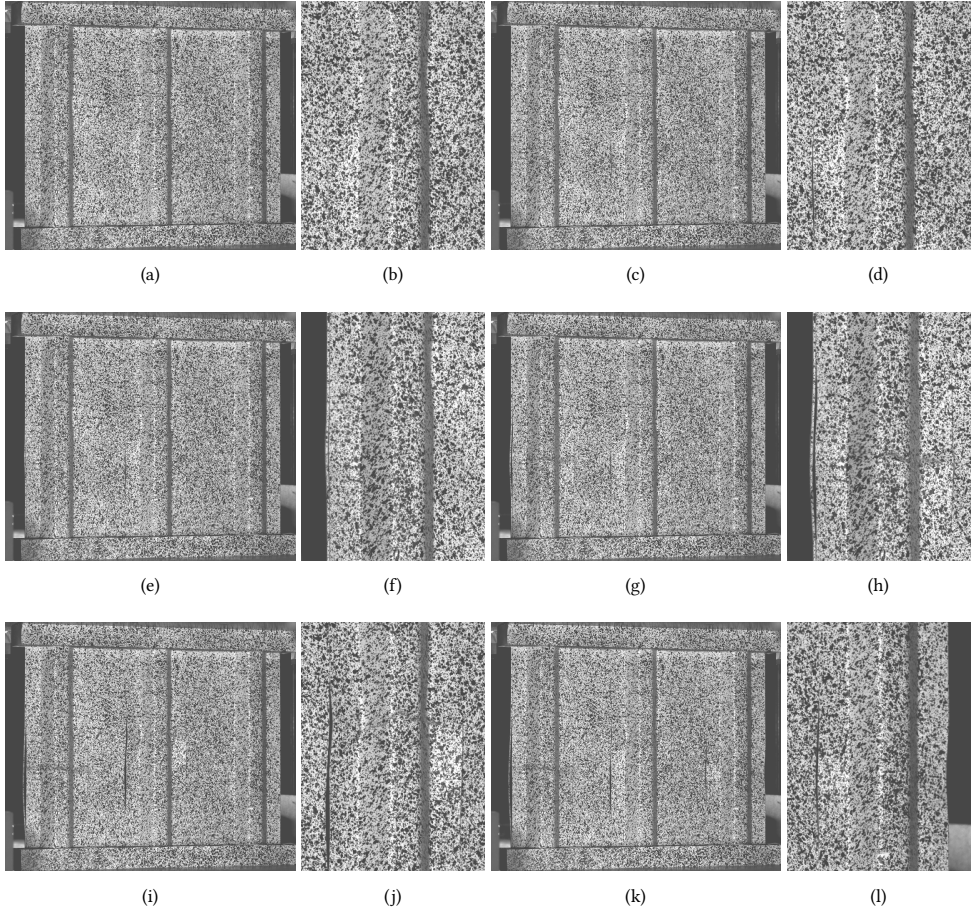


Figure 2.24: Failure sequence of panel 1: (a) separation in middle stringer; (b) close-up of middle stringer; (c) propagation of separation in middle stringer; (d) close-up of middle stringer; (e) separation in left stringer; (f) close-up of left stringer; (g) fracture of left stringer; (h) close-up of left stringer; (i) fracture of middle stringer; (j) close-up of fracture of middle stringer; (k) separation in right stringer; (l) close-up of right stringer.

2.7.5 POST-FAILURE

Photos of panel 1 after failure are shown in Figure 2.25(a-b). The panel shows large separated areas and large outward deformation of the skin. The left and middle stringer are fractured approximately in the middle of the panel, and several stringer flanges have delaminations. The skin appears to be mostly intact, with only minor damage close to the failed welds. These findings are supported by the c-scan results reported in Figure 2.26(a), where it is possible to note that the left and middle stringers have partial separations from

underneath the stringer at the top of the panel, with elliptical crack fronts, while the right stringer has almost no intact interface left.

Photos of panel 2 after failure are shown in Figure 2.25(c-d). The panel has large separated areas towards the top, with large outward skin deformation. It can be noted that the large separated areas are in the opposite direction compared to panel 1, which has more separation in the downward direction. The middle and right stringer are fractured approximately in the middle of the panel, and the stringer flanges show delaminations. The skin seems to be mostly intact, judging from both visual inspection and the c-scan results reported in Figure 2.26(b). From the c-scan, it can also be seen that the interface at the bottom of the middle stringer shows separations in both flanges with elliptical crack fronts.

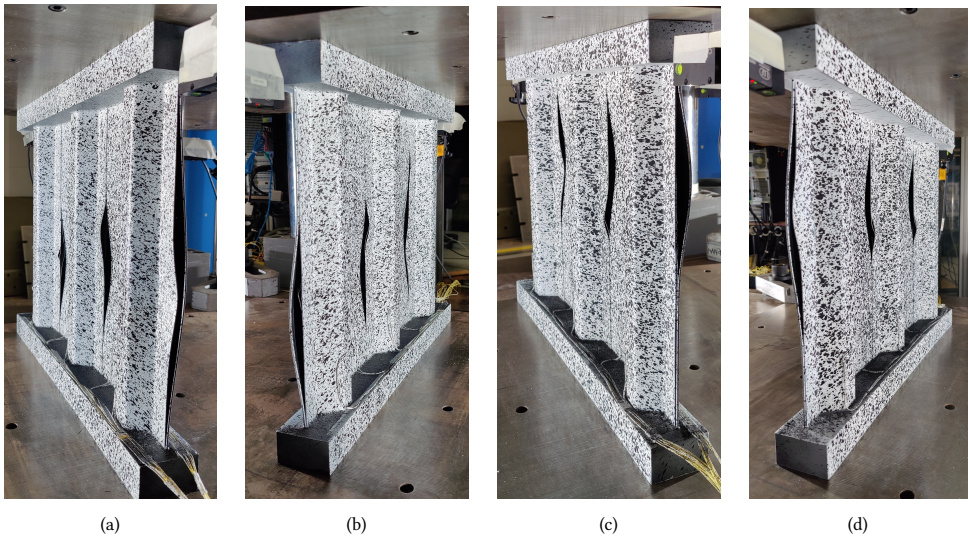


Figure 2.25: Post-failure photos: (a) panel 1 right side; (b) panel 1 left side; (c) panel 2 right side; (d) panel 2 left side.

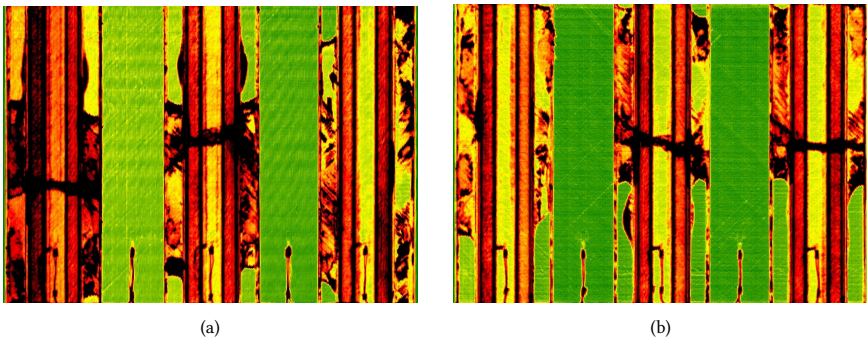


Figure 2.26: Post-failure c-scan: (a) panel 1; (b) panel 2.

2.7.6 WELD FRACTURE SURFACE

The middle stringer of panel 1 is removed after the test to investigate the weld fracture surface, which is shown in Figure 2.27. The area in between the red dashes is separated during the test, while the areas outside of the red dashes are separated after the test when the stringer is removed from the panel. The weld fracture surface can be identified by the darker and rough surface in comparison to the surrounding areas. It can be seen that there is limited damage to the skin-side of the interface, with only small amounts of fibres delaminated from the skin. The stringer flanges have several areas where the top ply has delaminated. There are also fibres fractured off the stringer, which remain attached on the skin-side of the interface. On both the left and right weld Figure 2.27(a+c), light grey marks indicate an elliptical crack front during propagation. The width of the weld varies slightly along the length, ranging from approximately 17 to 19 mm. However, the weld might seem wider than it actually is, due to the possibility of the adjacent surfaces being damaged by the separation of the weld.

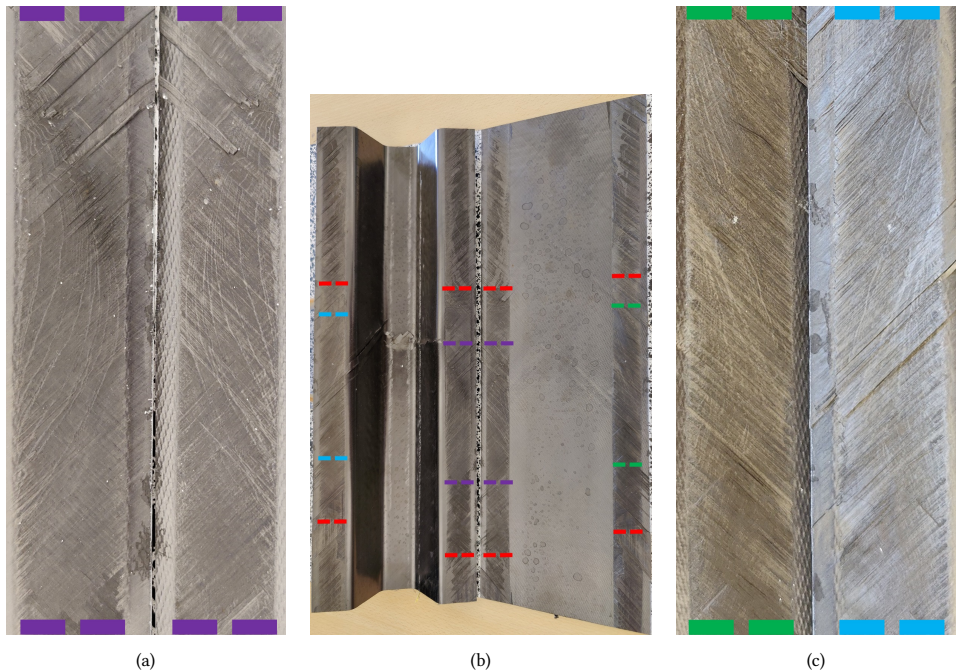


Figure 2.27: Weld fracture surfaces of panel 1 middle stringer: (a) close-up of the left weld, with the area between purple dashes; (b) welds middle stringer, with the area in between red dashes corresponding to the separated area in the test; (c) close-up of the right weld, with the area between blue and green dashes.

2.8 CONCLUDING REMARKS

This study investigates the conduction welded skin-stringer interface of the thermoplastic composite fuselage demonstrator of the STUNNING project, for which three-stringer panels are successfully designed, analysed and tested.

At first, a fuselage section is analysed to determine the buckling and failure behaviour, which is used as reference behaviour for the design of the panels. The critical failure mode is skin-stringer separation in post-buckling, with separation starting from underneath the stringer and growing in an outwards direction. The preliminary analysis of the three-stringer panel shows similar structural behaviour, with the main difference being the higher number of failure locations, which can be caused by the difference in boundary conditions.

Then, two three-stringer panels are manufactured and tested. The two panels show a similar pre-buckling stiffness, buckling load and initial buckling shape. It is however observed that only one panel changes buckling shape in post-buckling from a three half-wave shape to a four half-wave shape. The welded joint is able to withstand the deformation of post-buckling till a considerable high load, with the ratio between buckling load and final failure load being 1.94 and 1.87 for panels 1 and 2, respectively. The panels fail in post-buckling due to skin-stringer separation, with no material failure before the start of separation.

Skin-stringer separation appears to start from underneath the stringer, with separation growth in both the longitudinal direction and outward direction. The number of half-waves underneath the stringer increases before final failure, which indicates that the buckling shape underneath the stringer is an important factor.

Further numerical analyses of the two panels are conducted, which include imperfections from DIC and laminate thickness imperfections based on measurements of the manufactured panels. The overall structural behaviour of the two panels is accurately predicted, with a slight difference in the buckling shape evolution of panel 1 between the test and prediction. The skin-stringer separation behaviour is also predicted well.

The results obtained in this research do show that the methodology is a reliable tool for the analysis of welded panels in post-buckling. The post-buckling performance of the welded panels, and the predictable structural behaviour, show great promise for the use of thermoplastic composites for primary structures.

ACKNOWLEDGEMENT

This project has received funding from the Clean Sky 2 Joint Undertaking (JU) under grant agreement No 945583. The JU receives support from the European Union's Horizon 2020 research and innovation programme and the Clean Sky 2 JU members other than the Union.

The authors thank GKN Fokker and NLR - Netherlands Aerospace Centre, for the manufacturing and welding of the test panels.

DISCLAIMER

The results, opinions, conclusions, etc. presented in this work are those of the authors only and do not necessarily represent the position of the JU; the JU is not responsible for any use made of the information contained herein.

3

3

POST-BUCKLING DAMAGE TOLERANCE OF WELDED OMEGA-STIFFENED THERMOPLASTIC PANELS WITH INITIAL DAMAGE

Welded omega-stiffened panels made of thermoplastic carbon composite with initial damage in the conduction welded joint are analysed and tested to investigate the damage tolerance in post-buckling. Finite element analyses are performed, using the virtual crack closure technique to investigate skin-stringer separation for both the pristine welded joint and joints with initial damage. A sensitivity study is executed for the initial damage size and location with different geometrical imperfections. Four omega-stiffened panels are tested, of which three have initial damage consisting of a foil at the welded skin-stringer interface. During the test, digital image correlation is used to measure the panels' deformation to determine the evolution of the buckling shape and the interaction with the initial damage. A high-speed camera is placed on the stringer side of the panel to capture the final failure. The panels fail in post-buckling when skin-stringer separation occurs, starting from the initial damage. The finite element analysis is able to predict the overall structural behaviour well, with conservative failure load predictions for panels with initial damage in the middle stringer. Although the initial buckling shape is predicted well, the buckling shape evolution at higher loads is difficult to predict.

3.1 INTRODUCTION

Composite materials are increasingly used in the aeronautical field because of their performance-to-weight ratio. The structures commonly used in aeronautics consist of thin-walled designs with stiffening elements, such as the stiffened skin of a fuselage or wing. These structures are often subjected to compression loads, which leads to buckling, and have been shown to withstand load far into the post-buckling field [16, 38]. However, these structures are vulnerable to damage during manufacturing, in-service or maintenance, from which composite structures are more likely to sustain damage than metallic structures. The damage can occur internally and not show signs of damage during a visual inspection. This increases the concerns about allowing the structures to operate in the post-buckling field due to the complex nature of post-buckling behaviour and possible interaction with internal damages. Considerable weight savings can be achieved by allowing post-buckling, which requires an increased understanding of the damage tolerance of composite structures in post-buckling.

This research focuses on the damage tolerance of thermoplastic stiffened structures with welded joints. Thermoplastic composites show excellent promise for aeronautical structures regarding sustainability and cost-savings while also increasing damage tolerance due to the high toughness [10]. They offer new ways of manufacturing composite materials for out-of-autoclave processes, such as thermoforming, thermoplastic welding [9], in-situ consolidation [20], and in-autoclave co-consolidation [3].

The structures investigated in this research represent components of the thermoplastic multi-functional fuselage demonstrator of the STUNNING project [7, 38]. This project developed the required technologies for manufacturing the fuselage demonstrator, which consists of techniques such as compression moulding, press-forming and conduction welding. This paper conducts a combined numerical and experimental investigation to evaluate the damage tolerance of the conduction welded joint between skin and omega stringer in the post-buckling field. The higher toughness and new manufacturing technologies of thermoplastics can contribute greatly to the push for composite primary structures and advance towards structures designed for post-buckling below ultimate load.

Stiffened structures in post-buckling exhibit high out-of-plane deformations of the skin, which leads to skin-stringer separation as the common failure mode due to the high interface stresses between skin and stringer [12]. Skin-stringer separation is a widely researched phenomenon on thermoset composites [31, 32, 39] and, to a lesser extent, thermoplastic composites [16, 38]. The research on skin-stringer separation can be divided into the structural levels it is researched on, such as single-stringers and multi-stringer panel level, and the stringer design.

The damage tolerance of composite structures in post-buckling was investigated by Bisagni et al. [29]. Single-stringer compression specimens with omega stringer were designed to show structural behaviour representative of a multi-stringer panel. Bisagni and Dávila [40] further investigated the single-stringer compression specimens, with geometrical imperfections measurements and digital image correlation was used during the test to determine the buckling shape. Action and Leone [41] analysed and tested a multi-stringer panel with omega stringers and Teflon inserts to validate the CompDam material model. The panel failed due to skin-stringer separation in post-buckling, which showed stable damage growth before it became unstable and the panel collapsed. Mo et

al. [42] presented an experimental and numerical study on curved multi-stringer panels with omega stringers investigating the buckling and post-buckling behaviour. The study focussed on the effect of curvature, stringer spacing and skin thickness on the buckling behaviour and the prediction by Finite Element analysis. Feng et al. [43] studied the effect of impact damage positions on the buckling and post-buckling behaviour of stiffened panels with I-stringers. Panels were subjected to impact to create Barely Visible Impact Damage in different positions. It was seen that the impact damage had little influence on the buckling load, compared to a pristine panel, but the failure load decreased up to 10 %. Sepe et al. [44] tested and analysed two-stringer panels to investigate the residual strength after low-velocity impact and with a cut-out. The multiple impacts and cut-out lowered the ultimate strength of the panel by approximately 30 %. Stiffened panels made of thermoplastic composite were tested in compression after impact by Ishikawa and Matsushima [45]. Two single-stringer hat-stiffened panels were impacted at a different energy level, resulting in delaminations between skin and stringer of approximately 18 and 900 mm², that lead to a difference of 20 % in compression after impact strength.

Blade-stiffened panels in pristine condition and with initial damage were analysed and tested in post-buckling by Orifici et al. [25]. Two different panel designs were tested, with panel lengths of 400 and 500 mm and an initial damage length of 80 and 105 mm, respectively. The initial damage reduced the failure load up to approximately 50% in post-buckling. Riccio et al. [26] introduced a numerical procedure which utilizes both the Virtual Crack Closure Technique (VCCT) and the Cohesive Zone Method (CZM) to model skin-stringer separation. The numerical results are compared to the experimental data of Orifici et al. [25], and showed good correlation. Bertolini et al. [14, 15] compared the modelling of separation by VCCT and CZM on non-specific specimen level and then applied VCCT on element and panel level because of its computational efficiency. The computational time differed by one order of magnitude on specimen level, and CZM was therefore considered unsuitable for industrial applications at the higher structural level.

The sensitivity of stiffened panels with blade stringers to the damage size, width, location and the number of initial damage locations was numerically investigated by Ji et al. [46]. The damage size had the largest effect on the final failure load, with a debond length of 10% of the panel length, causing a 25 % reduction of the final failure load. The sensitivity to the initial damage size and location of stiffened panels with omega stringers was numerically investigated by Yetman et al. [47]. The damage size influenced both the buckling load and failure load, while the damage location only influenced the failure load and not the buckling load.

In this paper, omega-stiffened thermoplastic panels are analysed and tested to investigate the damage tolerance of the conduction welded joint. Three panels have initial damage, and one panel is in a pristine state. The panels are manufactured by project partners NLR - Netherlands Aerospace Centre and GKN Fokker. The initial damage involves a foil inserted at the skin-stringer interface before welding. The numerical analyses are done with Abaqus and use the Virtual Crack Closure Technique to model skin-stringer separation for pristine joints and joints with initial damage. The analyses are executed to predict the behaviour of the test panels, with initial geometrical imperfections accounted for, and for a sensitivity study on damage size and location. The four panels are tested until they collapse.

3.2 WELDED OMEGA-STIFFENED THERMOPLASTIC PANELS

The welded omega-stiffened thermoplastic panels are designed to show structural behaviour similar to the STUNNING fuselage [38]. They have three stringers, to allow for bay buckling on both sides of the middle stringer and achieve a deformation and loading similar to a fuselage section. The stringer pitch is equal to the stringer pitch of the keel section of the STUNNING fuselage, 212 mm, which results in a total width of 556 mm, as reported in Figure 3.1. The panels are 490 mm long, which is the maximum welding length at the time of production, with the panel's loading edges trimmed.

The omega stringer is 132 mm wide, 30 mm in height and has a web-cap angle of 125°, as reported in Figure 3.2. The flange width is 28.7 mm, and the cap width is 30 mm. The panels are made of CF/LM-PAEK material, and the properties used are reported in Table 3.1 [33]. The nominal ply thickness is 0.184 mm, and the layups of the skin and stringer are reported in Table 3.2.

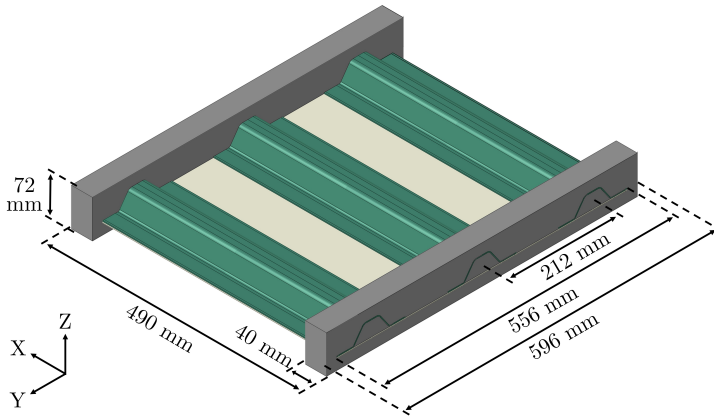


Figure 3.1: Welded omega-stiffened thermoplastic panel.

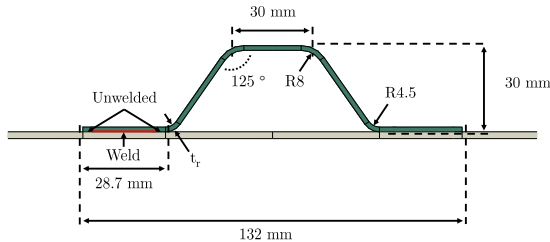


Figure 3.2: Omega stringer geometry and weld.

Table 3.1: CF/LM-PAEK Toray CETEX TC1225 material properties [33].

E_{11} [MPa]	E_{22} [MPa]	ν_{12} [-]	G_{12} [MPa]	F_1^t [MPa]	F_1^c [MPa]	F_2^t [MPa]	F_2^c [MPa]	F_{12} [MPa]
116800	9100	0.36	4100	2442	1250	94	212	99

Table 3.2: Layups of the welded omega-stiffened thermoplastic panel.

Name	Layup	Thickness (mm)
Skin	$[-45/45/90/0/90/0]_s$	2.208
Stringer	$[45/0/-45/0/90]_s$	1.656

Four omega-stiffened panels are manufactured. The skin is manufactured by project partner NLR - Netherlands Aerospace Centre. The skin is laid up by automatic tape laying and then consolidated in an autoclave. The stringers are joined to the skin with conduction welding by project partner GKN Fokker. The conduction welding process involves a heating element applying pressure and heat on top of the stringer flange, which melts the material and joins the skin and stringer. The weld is approximately in the middle of the stringer flange, with small unwelded regions on both sides of the weld, as reported in Figure 3.2. The weld width at the interface is approximately 18 mm. The initial damage is created by inserting a foil between the skin and the stringer flange, which prevents this area from being welded.

The panels are received from the project partners as reported in Figure 3.3 (a). The panels are then prepared for testing in several steps. They are trimmed, followed by the casting of potting to both ends of the panel for load introduction. Then the loading faces of the panels are machined to minimise loading imperfections. The following steps are to attach strain gauges and wiring, as shown in Figure 3.3 (b). The panels have 10 strain gauges attached, of which the locations are reported in Figure 3.4, 135 mm from the bottom loading plane. The strain gauges are on top of the cap and the bottom of the skin underneath each stringer. There are two strain gauges attached back-to-back in the bays. The strain measurements are used for load distribution and redistribution due to phenomena such as buckling and failure, and also for loading imperfections. The last step is to paint the panels in matt white, followed by black speckles, for digital image correlation.

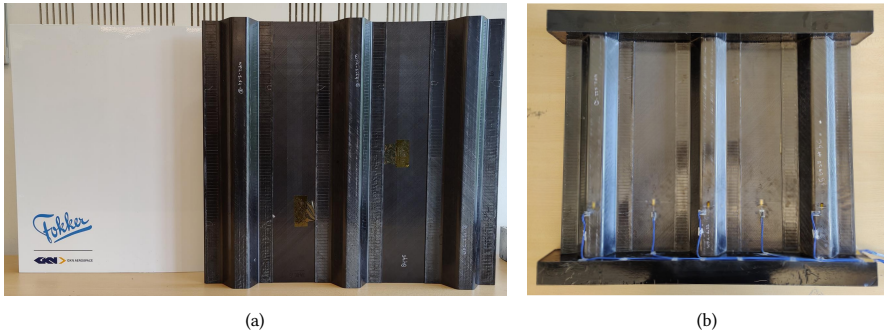


Figure 3.3: Omega-stiffened panels: (a) as received; (b) with potting and strain gauges.

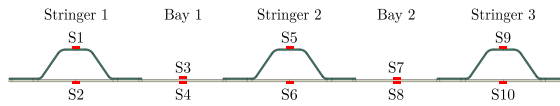


Figure 3.4: Strain gauge locations.

3.3 NUMERICAL ANALYSIS OF WELDED OMEGA-STIFFENED THERMOPLASTIC PANELS WITH INITIAL DAMAGE

The numerical analyses are executed to study the buckling, failure behaviour and damage tolerance of the panels with Abaqus 2021 [34].

3.3.1 ANALYSIS METHODOLOGY

The panels are analyzed with a dynamic implicit analysis and non-linear geometry enabled. The analysis time is 1 s with a minimum time-step of $1e-08$ s and a maximum and initial time-step of 0.01 s. Load is applied with displacement boundary conditions on two reference nodes. The reference nodes are placed at each loading plane, and rigid body ties are used between the reference nodes and the loading plane. One reference node is clamped, except in the longitudinal direction, for which 2.5 mm of displacement is applied. The other reference node is clamped. The boundary conditions and the time-step result in a displacement rate of 2.5 mm/s.

The mesh size of the laminated sections is 2.5 mm. The potting material has a variable mesh size, between 2.5 and 10 mm. The potting mesh starts fine where it joins to the laminated sections, and becomes courses in an outwards direction. The laminated sections are modelled with continuum shells (SC8R), and the potting is modelled with reduced integration solid elements (C3D8R) for improved computational efficiency.

The laminated sections and the potting are joined with shared nodes in the potting region. The skin and stringer between the potted sections are joined with the Virtual Crack Closure Technique (VCCT), to resemble the welded joint.

In this study, VCCT is utilised for both panels in a pristine state and with initial damage, with a weld width of 18 mm. The VCCT method is normally limited to structures with initial damage due to the pre-crack requirement. However, the weld has small unwelded

regions on both sides of the weld, as shown in Figure 3.2, allowing VCCT to be used for pristine welded joints. This results in a relatively efficient analysis for a panel-level structure due to the courser mesh allowance of VCCT compared to other methods. In this model, skin-stringer separation can only occur at the interface between skin and stringer, and can't grow into the laminates, to limit the complexity of the model and analysis. Also, due to the unwelded region on both sides, it is less likely that separation will migrate.

In the VCCT definition, the skin side is assigned as the slave surface and the stringer side as the master surface, in combination with node-to-surface discretization. Contact stabilization is used with a factor of 1e-4. The fracture tolerance is set to the default value of 0.2, and the unstable crack growth tolerance is set to 1. The Benzeggagh-Kenane (BK) criterion is used to model mode-mixity, which is reported in Equation 3.1. To determine when fracture occurs, VCCT calculates the critical equivalent strain energy release rate G_{equivC} using the BK criterion and the critical energy release rate with Equation 3.2. When $G_{equivC} \geq G_{equiv}$, fracture occurs. The required fracture toughness of the interface and the BK parameter are based on a similar material from literature, AS4/PEEK [37], of which the matrix is of the same polyaryletherketone polymer family. The properties are reported in Table 3.3. The assumption is made that G_{IIC} and G_{IIIC} are equivalent.

$$G_{equivC} = G_{IC} + (G_{IIC} - G_{IC}) \left(\frac{G_{II} + G_{III}}{G_I + G_{II} + G_{III}} \right)^\eta \tag{3.1}$$

$$G_{equiv} = G_I + G_{II} + G_{III} \tag{3.2}$$

Table 3.3: Fracture properties of skin-stringer interface [37].

G_{IC} [kJ/m ²]	G_{IIC} [kJ/m ²]	G_{IIIC} [kJ/m ²]	η [-]
0.969	1.719	1.719	2.284

3.3.2 EFFECT OF DAMAGE SIZE AND LOCATION

This section focuses on the analysis of panels with different damage sizes and damage locations. The first study considers the damage size of an initial damage in the centre of the panel, as shown in Figure 3.5 (a). The considered damage sizes are reported in Table 3.4. The results of the study are reported in terms of the initiation load and the final failure load. Initiation is considered the start of skin-stringer separation, and final failure is considered when unstable separation leads to panel collapse.

The initiation load and failure load for a panel with one initial damage of different sizes are reported in Figure 3.6 (a). The panel has a low sensitivity to initial damage sizes of 10 and 25 mm, and for a damage size of 40 mm both the initiation and final failure load drop considerably. A buckling shape change most likely causes this drop. The panel starts out with three half-waves in the bays, reported in Figure 3.7 (a), and the panel with a damage size of 40 mm presents a gradual shape change to four half-waves, reported in Figure 3.7 (c). A damage size of 25 mm and below did not show this buckling shape change. The initiation load drops further for larger damage sizes, while the failure load does not go

below 230 kN for the damage sizes in this study. Based on these results, it is chosen to use a 40 mm damage size for the test panels, as reported in Figure 3.8(a). This damage size presents a considerable drop in final failure load, while there is still a margin between the buckling load of approximately 170 kN and the initiation load of 230 kN. Since the strength of the welded joint is unknown at the time of the design, a conservative damage size is deemed best.

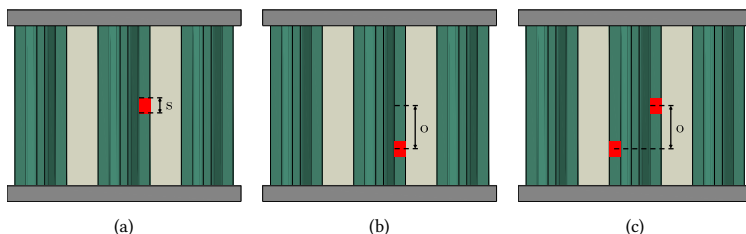


Figure 3.5: Panel illustrations of three sensitivity parameters: (a) damage size; (b) damage 1 offset; (c) damage 2 offset.

Table 3.4: Sensitivity study parameters.

Damage size [mm]	Damage offset [mm]
0	0
10	22
25	44
40	66
55	88
70	110
85	132
100	154

The second study considers the location of the initial damage, for a panel with one initial damage and a panel with two initial damages, both for a damage size of 40 mm. The location is defined as the offset between the panel’s centre and the damage’s centre, as reported in Figure 3.5 (b-c). The study considers one initial damage (Figure 3.5 (b)) and two initial damages, where the first damage in the right flange will remain in the centre, and the second damage in the left flange will be offset (Figure 3.5 (c)). The damage offset range of the study is reported in Table 3.4.

The initiation load and failure load for a panel with one and two initial damages at different locations are reported in Figure 3.6 (b). For panels with one initial damage, the initiation load is similar for offsets of 0 and 22 mm, and then for higher offsets the initiation load increases. This is caused by differences in the buckling shape evolution. The panels have an initial three half-wave buckling shape, as reported in Figure 3.7 (a), that changes to four half-waves in one bay for 0 and 22 mm offset, as reported in Figure 3.7 (b). Higher offsets do not exhibit this buckling shape change. The initiation load does go down between 44 and 110 mm offset, which seems to be caused by the relative position of the damage w.r.t. the outward half-wave being more critical for separation. The failure load is lowest

for 0 mm offset, for higher offsets it plateaus at approximately 270 kN. An offset of 0 mm is chosen for the test panel with one initial damage, which is reported in Figure 3.8 (a).

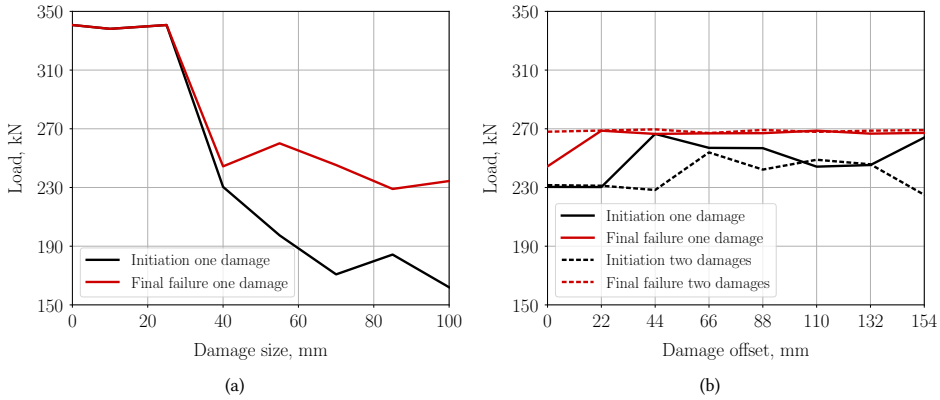


Figure 3.6: Sensitivity study of: (a) damage size; (b) damage offset.

The panel with two initial damages shows an initiation load of approximately 230 kN for 0, 22 and 44 mm of offset, and increases to approximately 255 kN know for an offset of 66 mm. This difference is caused by the change in buckling shape from three to four half-waves in both bays, as reported in Figure 3.7 (c), and four half-waves seems to be more critical. The failure load is approximately 270 kN for all cases, which seems to be dominated by a certain amount of separated area after which separation becomes unstable and the panels collapse. Offsets of 88, 110 and 132 mm present similar behaviour in terms of initiation load, but the case of 110 mm is deemed to be most interesting, as the separation starts at the damage in the middle, while the opposite flange also starts to separate in the middle of the panel which grows towards the second initial damage. This interaction is considered interesting, while it has a low risk of the initial damages quickly causing tunnelling behaviour, and far enough from the potting to minimise the influence of boundary conditions. Therefore, an offset of 110 mm is chosen for the panel with two initial damages, as reported in Figure 3.8 (b).

The last configuration has one initial damage of 40 mm in the side stringer, as reported in Figure 3.8 (c). This allows to study the effect of initial damage in different stringers.

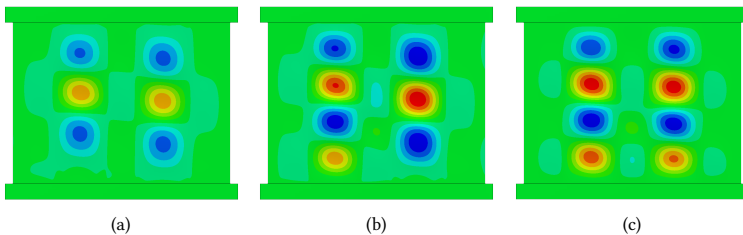


Figure 3.7: Buckling shapes: (a) three half-waves; (b) three and four half-waves; (c) four half-waves.

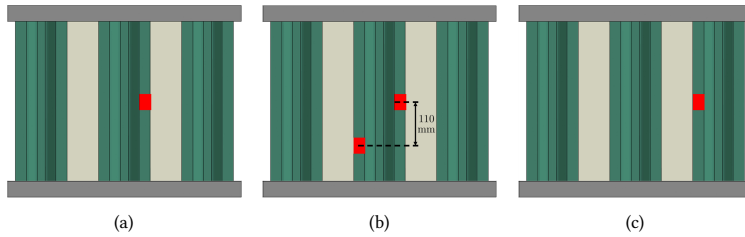


Figure 3.8: Panels with initial damage of 40 mm: (a) panel 2; (b) panel 3; (c) panel 4.

3.4 TEST SETUP AND PANELS MEASUREMENTS

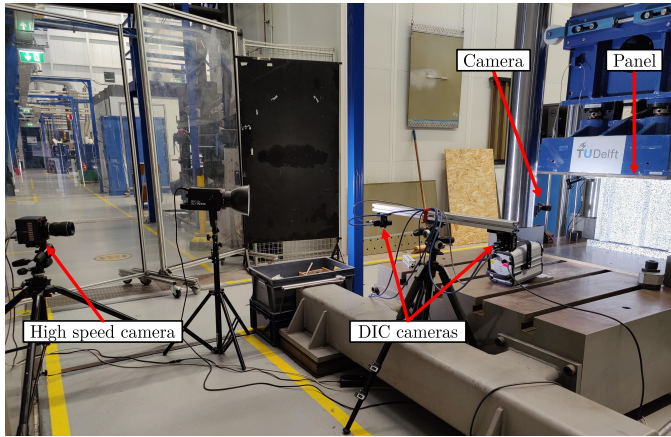
The panels are tested in compression until failure with an MTS test machine at Delft University of Technology. The test machine is capable of 3500 kN in tension and compression, and the configuration with the adjustable compression plate is capable of 1300 kN.

The test setup is reported in Figure 3.9 from the (a) stringer side and (b) skin side of the panel. The panels are positioned in the test machine and a preload of 2 kN is applied to keep the panel in place. The test is then executed with a loading rate of 0.1 mm/min. and the loading stops automatically after failure.

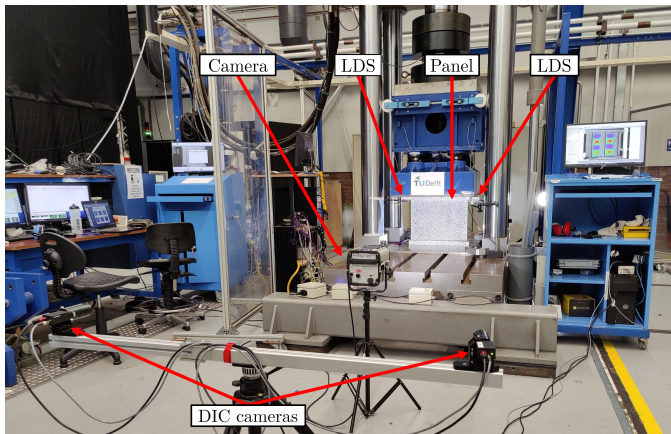
Two DIC systems measure the deformation field, with one system on each side of the test setup. The DIC systems have 5 MP cameras, and the post-processing software is VIC3D 8. The longitudinal displacement of the compression plate is measured by three Laser Displacement Sensors (LDS). Two LDS are placed next to the potting ends, and one is placed out-of-plane on the corner of the plate, which allows to determine if loading imperfections occur. All mentioned measurement systems record every 3 seconds, which results in approximately 500 data points per test for a pristine panel. Three cameras are used to capture the test, with two cameras on the stringer side to capture the buckling and skin-stringer separation behaviour and one camera on the skin side. Final failure of the panels is captured by a high-speed camera which records at 10000 fps. The camera captures the full panel.

The imperfections of the panels are measured. The measurements allow comparing the imperfections between the panels, and a selection of the imperfections will be taken into account in the numerical analysis.

The first imperfection that is measured is the out-of-plane imperfection of the skin, for which DIC is used. The nominal design has a flat skin, and the imperfection is the deviation of the skin w.r.t. a flat plane. The out-of-plane imperfections of all four panels are reported in Figure 3.10, with the imperfection aligned with the z-axis of the axis system reported in Figure 3.1. All four panels have a similar curved imperfection in the width direction, with a total magnitude of the imperfection ranging from 12.36 mm to 15.88 mm. The imperfection has a counterclockwise skew, probably caused by the layup and the outer -45 ply. The panels are also slightly curved in the longitudinal direction, but it is minimal compared to the imperfection in the width direction. The highest curvature in the width direction is in the welded area, as the imperfection is mostly caused by the local heating of the conduction welding process, which results in thermal stresses.



(a)



(b)

Figure 3.9: Test setup seen from: (a) stringer side; (b) skin side.

The skin and stringer laminate thickness is measured with a micrometer. The skin has an average thickness of 2.14 mm, which is thinner than the nominal thickness. The stringers have an average thickness of 1.66 mm, close to the nominal thickness. The bottom radius of the stringer is, however, thinner than nominal, with an approximate thickness of 1.15 mm. The stringer spacing is measured to determine stringer offset and alignment. Panels 1 and 2 have no considerable offset or misalignment. Panels 3 and 4 have an offset of approximately 1 mm of the middle stringer.

The numerical analysis of the four panels will include a selection of these imperfections, which are: the out-of-plane imperfection, the skin thickness, the thickness of the bottom stringer radius, the middle stringer offset of panels 3 and 4, and finally, the average panel length of 491 mm. Residual stresses from the manufacturing process are not taken into account.

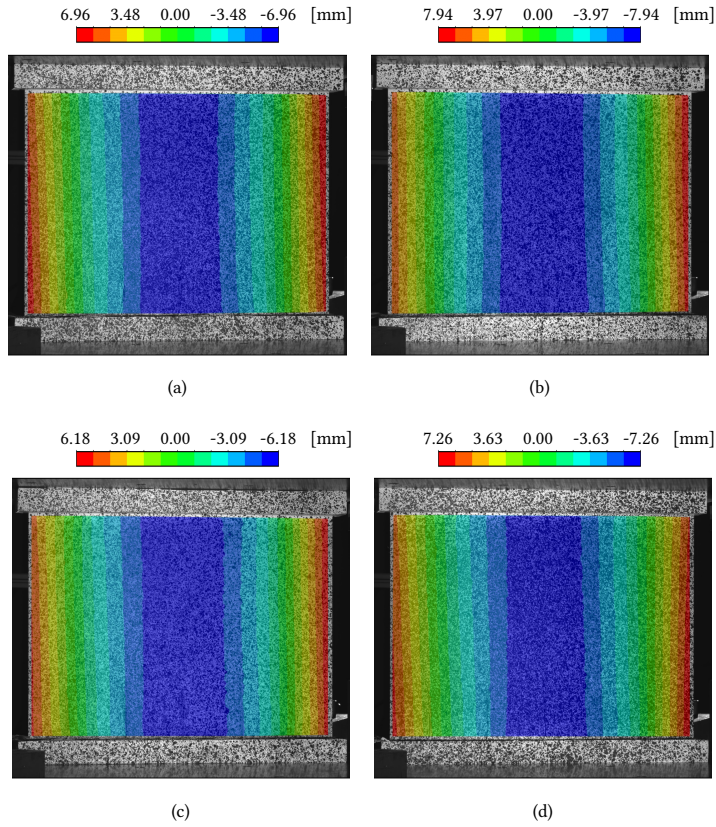


Figure 3.10: Out-of-plane imperfection of test panels: (a) panel 1; (b) panel 2; (c) panel 3; (d) panel 4.

3.5 DAMAGE AND IMPERFECTION SENSITIVITY STUDY

This study considers the interaction between the damage location and size for different geometrical imperfections. The study is executed for different imperfection amplitudes, as reported in Table 3.5. The damage size sensitivity study will be done for both panel 1 and 2 imperfections, which are reported in Figure 3.10(a) and (b), respectively, and the damage location sensitivity study for the panel 2 imperfection.

Table 3.5: Sensitivity study parameters.

Imperfection amplitude
0
0.5
1
1.5

3.5.1 DAMAGE SIZE SENSITIVITY

The initiation loads for the damage size sensitivity study with panels 1 and 2 geometrical imperfections are reported in Figure 3.11 (a) and (b), respectively. For small damage sizes, a higher imperfection amplitude lowers the initiation load, especially for the imperfection of panel 2. At a damage size of 40 mm and larger, the initiation load drops considerably for most cases, except for an imperfection amplitude of 0.5 of panel 2. The average initiation load for a damage size of 40 mm is 275 kN for the imperfection of panel 2, while it's 234 kN for the imperfection of panel 1. This is a decrease in the failure load compared to a pristine panel of 30% and 17% for panels 1 and 2, respectively. The initiation loads drop further for larger damages, with the case of no imperfection presenting the highest sensitivity to the damage.

The failure loads of the damage size sensitivity study are reported in Figure 3.11 (c) and (d), for panels 1 and 2, respectively. When comparing the results to the initiation loads in Figure 3.11 (a) and (b), it can be concluded that for damage sizes of 40 mm and smaller, the panels show final failure at or shortly after the initiation of skin-stringer separation. At larger damage sizes, the failure load increases for the imperfection of panel 2 and an amplitude of 1 and 1.5. This is also seen for the imperfection amplitude of 1 of panel 1, while imperfection amplitudes of 0.5 and 1.5 have varying results. At damage sizes of 40 mm and larger, the panels without imperfection have the lowest failure loads, and the geometrical imperfection seems to lower the sensitivity to damage for skin-stringer separation. At damage sizes of 55 mm and above, the lower bound for the failure load is between 230 and 250 kN, which is a reduction of 26-32 % of the failure load compared to a pristine panel.

The panels present the highest sensitivity to damage size between 25 mm and 55 mm, at a larger damage size the initiation and final failure load start to plateau. The explanation for this effect is twofold. Firstly, the initiation of skin-stringer separation seems to occur when the damage opens, of which the load does not seem to vary considerably above a certain damage size. Secondly, above a certain damage size, final failure occurs when the weld in the same stringer, but opposite flange of the damage location, becomes critical and separates in an unstable matter. This lowers the overall sensitivity to the damage size, as the opposite flange dominates final failure. The criticality of the opposite flange can be influenced by the opening of the damage, which is a rather stable increase of loading on the weld, but also due to buckling shape changes in the bay which can trigger sudden final failure.

Two damage sizes are investigated further to study the possible effect of imperfections on the buckling and failure behaviour of panels with damage in more detail.

The first investigation focuses on the damage size of 40 mm for different imperfection amplitudes of panel 2, as both the initiation load and failure load are highly affected. The load-displacement behaviour for the three imperfection amplitudes of 0, 0.5 and 1 is reported in Figure 3.12 (a). For no imperfection, a small load drop is seen at 230 kN, due to the opening of the initial damage and the start of separation, and final failure occurs at 244 kN. The imperfection amplitudes of 0.5 and 1 have a failure load of 328 and 276 kN, respectively, and experience no load drop before final failure. Out-of-plane contour plots are reported in Figure 3.12 (b-d), (e-g) and (h-j) for imperfection amplitudes 0, 0.5 and 1, respectively. The initial damage of 40 mm is on the left side of the panel. All three cases start initially with three half-wave buckling shapes with a clockwise skew regarding half-wave

placement. At higher loads, a fourth half-wave appears in the bay with the initial damage for no imperfection, while the other two cases present no additional half-waves in the bays. For an imperfection amplitude of 0.5 the skew of the half-waves rotates anti-clockwise with increased load, and additional half-waves appear underneath the stringers.

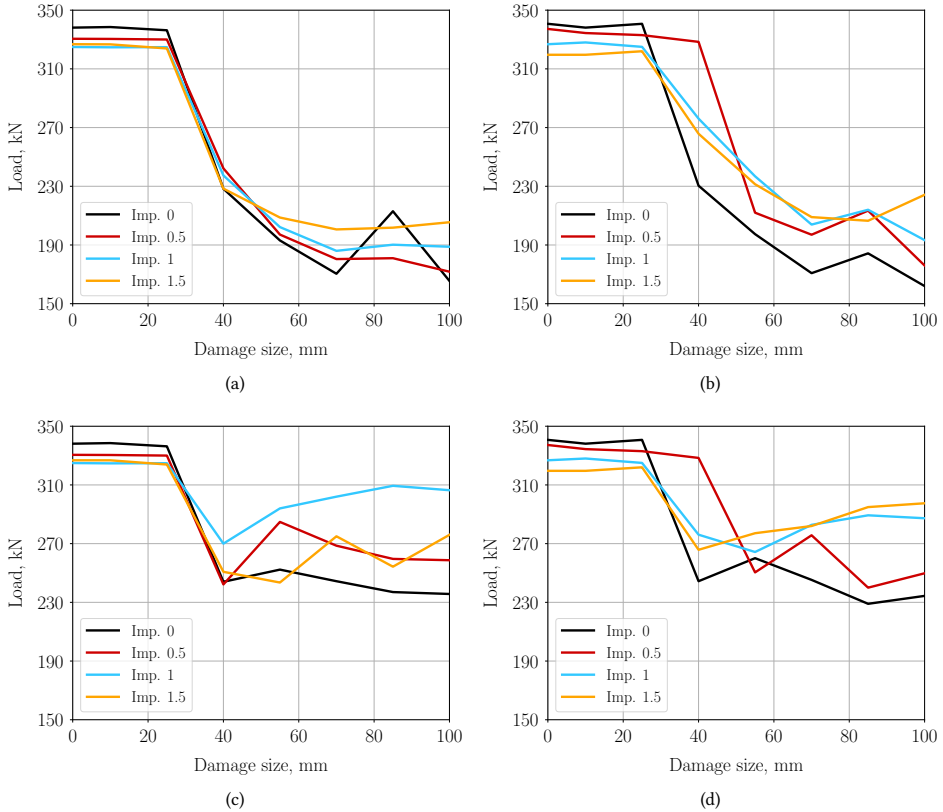


Figure 3.11: Damage size sensitivity study results for different imperfection amplitudes: (a) initiation panel 1 imperfection; (b) initiation panel 2 imperfection; (c) final failure panel 1 imperfection ; (d) final failure panel 2 imperfection.

The effect of the different buckling shapes, caused by different imperfections, on the skin-stringer separation behaviour and failure load is considerable. This seems to be related to the relative position of an outward half-wave w.r.t. to the initial damage, which can cause opening of the initial damage and start separation. The four half-wave buckling shape is most critical, where an outward half-wave with a shorter half-wave length is positioned close to the initial damage location. In this case separation starts at 230 kN, with a small load drop, followed by stable separation growth until a load of 244 kN. Then the middle stringer weld, opposite to the initial damage, starts to separate. The least critical case is with an imperfection amplitude of 0.5, where there is no outward half-wave close to the initial damage. At higher loads, the outward half-wave only moves further away, with the buckling shape having an anti-clockwise skew. Also, the curvature of the imperfection

is highest in the weld region, which can also effect the separation behaviour.

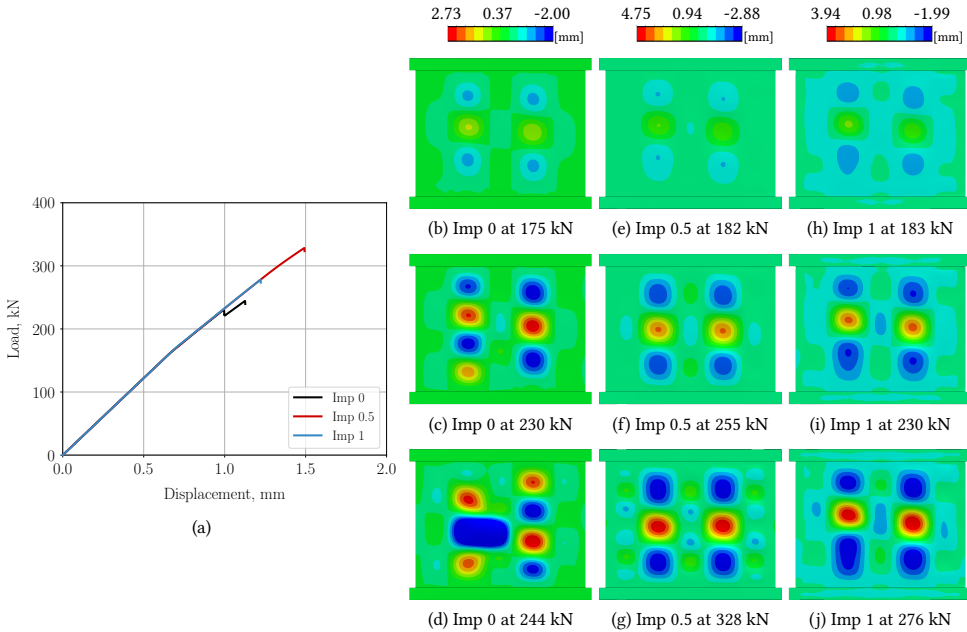


Figure 3.12: Panels with 40 mm damage and panel 2 imperfection: (a) load-displacement; (b-g) out-of-plane displacement contour plots.

The second investigation is on the damage size of 70 mm for different imperfection amplitudes of panel 1. The load-displacement behaviour for the three imperfection amplitudes of 0, 0.5 and 1 is reported in Figure 3.13 (a), which present higher failure loads for a larger imperfection. After buckling, all three imperfection amplitudes experience a small load drop, which is caused by a small separation event at the initial damage location. Out-of-plane contour plots are reported in Figure 3.13 (b-d), (e-g) and (h-j) for imperfection amplitudes 0, 0.5 and 1, respectively. For no imperfection, the initial buckling shape has three half-waves (b), and the initial damage opens shortly after a small load increase which results in an anti-symmetric buckling shape (c). The imperfection amplitudes of 0.5 and 1 present opening of the initial damage at the start of buckling (e-h), with an anti-symmetric buckling shape. All three amplitudes show stable separation growth of the initial damage after the first separation event, until final failure. The final failure of imperfection amplitudes 0 and 0.5 starts with the right bay switching buckling shape to four half-waves (d-g). This buckling shape change is not seen for an imperfection amplitude of 1.

At final failure, all three imperfection amplitudes show a similar amount of separation growth, with the separation length growing from 40 mm to approximately 162 mm. It is therefore difficult to judge how much the buckling shape change of imperfection amplitude 0 and 0.5 contributes to the start of final failure, and the separation length might be the main contributor. The imperfection amplitudes and resulting buckling shape differences do contribute to the differences in final failure, but indirectly by influencing the separation

behaviour.

A larger imperfection delays the start of separation at 173, 183 and 192 kN for imperfection amplitude 0, 0.5 and 1, respectively. Also, for larger imperfections, this separation event caused less growth while occurring at higher loads. This can be considered counter-intuitive, as one could expect that a higher load leads to more separation. This might be caused by the relatively high curvature of the imperfection in the weld region. The larger imperfection increases the curvature of the welded interface, which might increase the initiation and the failure load.

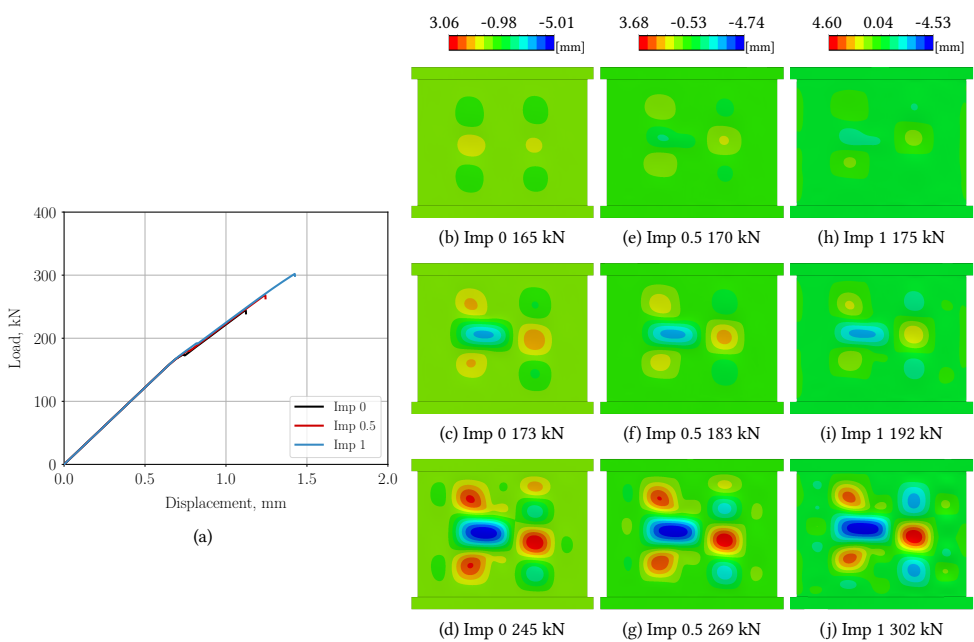


Figure 3.13: Panels with 70 mm damage and panel 1 imperfection: (a) load-displacement; (b-g) out-of-plane displacement contour plots.

3.5.2 DAMAGE LOCATION SENSITIVITY

The initiation loads for single damage have a lower bound of approximately 230 kN, as reported in Figure 3.14 (a). For an offset of 0 mm, the initiation load is highly influenced by the imperfection amplitude, with the imperfection amplitude initially increasing the initiation load considerably and then converging to an intermediate load level between 230 and 270 kN. The results from different imperfection amplitudes converge for offsets between 44 and 110 mm, with the highest initiation load for no imperfection. The results diverge at offsets above 110 mm, with larger imperfections leading to higher initiation loads. This effect is caused by all cases between 44 and 110 mm offset presenting similar three half-wave buckling shapes, and more varying buckling shapes below 44 mm and above 110 mm offset. The higher sensitivity to the damage location between 44 and 110 mm offset is most likely caused by the relative location of the damage w.r.t. an outward

buckling half-wave. The lower sensitivity at 132 mm for imperfection amplitudes 1 and 1.5 are caused by a buckling shape change underneath the stringers, and results at 154 mm offset are most likely starting to get affected by the proximity of the potting.

The final failure loads for single damage show less variance than the initiation loads, as reported in Figure 3.14 (c), with a lower bound of approximately 250 kN. The largest difference is seen at 0 mm offset, where the highest failure load is for the imperfection amplitude of 0.5. At high offsets of 132 mm and 154 mm, the imperfection amplitude of 1 and 1.5 shows the highest failure loads, where final failure occurs after the first initiation of skin-stringer separation. Most cases that present initiation above approximately 270 kN, collapse after initiation, while cases that experience initiation below 270 kN continue to carry load until approximately 270 kN.

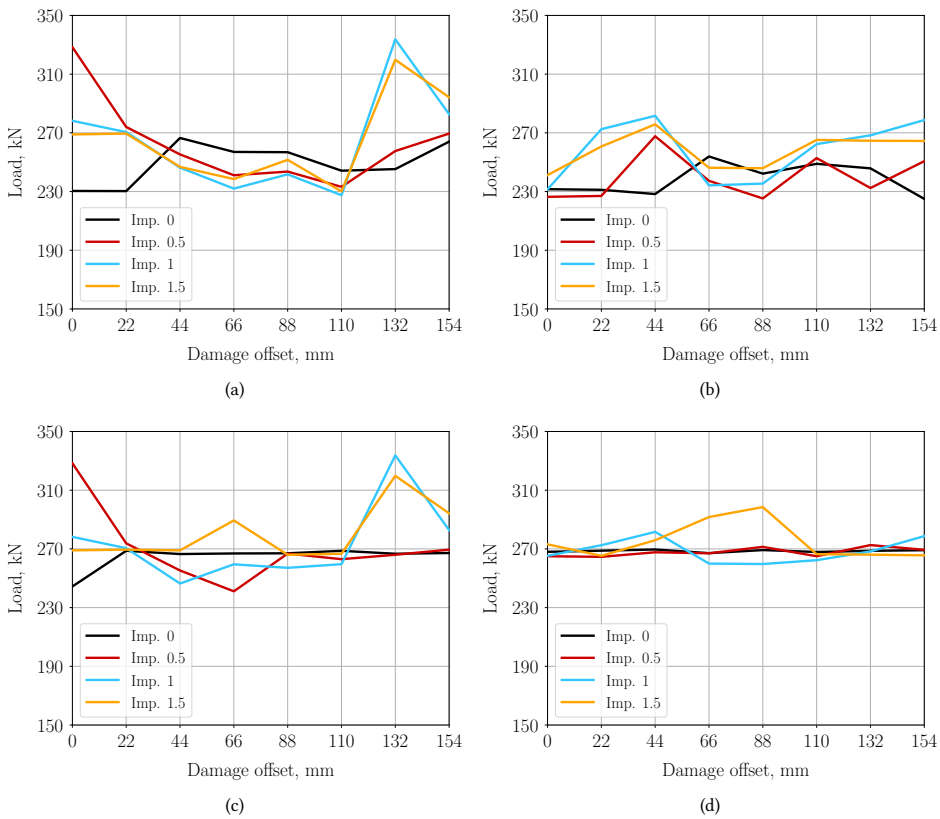


Figure 3.14: Damage offset sensitivity study results with Panel 2 imperfection: (a) initiation damage 1; (b) initiation damage 2; (c) final failure damage 1 ; (d) final failure damage 2.

The results of the sensitivity study with two initial damages shows initiation loads between 230 and 280 kN, as reported in Figure 3.14 (b). Imperfection amplitudes 1 and 1.5 result in similar behaviour over the whole offset range, while imperfection amplitudes 0 and 0.5 result in varying behaviour. There are three different ways in which initiation starts. Firstly, the damage at the middle of the panel starts, followed by the second damage. Secondly, the second damage with the offset starts, followed by the damage in the middle of the panel. Lastly, both damages experience initiation simultaneously. Offsets of 0 and 22 mm always experience simultaneous initiation, while 66 mm always initiates at the second damage. The remaining cases have varying behaviour, due to differences in buckling shapes and buckling shape evolution. One of the common factors seems the proximity of an outward half-wave, which increases the criticality of a damage location.

The failure load present little variation for the offset of the second damage, as reported in Figure 3.14 (d), with most failure loads at approximately 270 kN. Most cases show that after the initiation of the two damage locations, one tunnel (or one half-wave) is formed between the two locations, and final failure occurs after one of the side stringers exhibits skin-stringer separation. An exception is for an imperfection amplitude of 1.5 for an offset of 55 and 88 mm, which have a higher failure load, and there are two separate tunnels underneath the middle stringer.

The effect of the imperfection amplitude is investigated in more detail for an offset of 110 mm, as this offset is chosen for one of the test panels. The load-displacement behaviour for the three imperfection amplitudes of 0, 0.5 and 1 is reported in Figure 3.15 (a), which shows higher initiation load and a lower failure load for higher imperfection amplitudes. Out-of-plane contour plots are reported in Figure 3.13 (b-d), (e-g) and (h-j) for imperfection amplitudes 0, 0.5 and 1, respectively. All three imperfection amplitudes start with a three half-wave buckling shape (b-e-h). The case of no imperfection presents a buckling shape change to four half-waves in both bays (c). The buckling shape evolution between imperfection amplitudes 0.5 and 1 shows differences in half-wave lengths and skew of the half-wave positions (f-i). After initiation, all three cases experience tunnelling behaviour underneath the middle stringer (d-g-j). For the case of no imperfection, initiation starts at the damage in the middle of the panel, while for the cases with an imperfection amplitude of 0.5 and 1, initiation starts at the second damage at an offset of 110 mm. After the initiation of skin-stringer separation, it presents a load-drop, followed by stable separation growth until final failure when one of the side-stringer starts to separate. The lower imperfection amplitudes have a lower initiation load, and more separation growth after the separation event, which seems to lead to a higher final failure load.

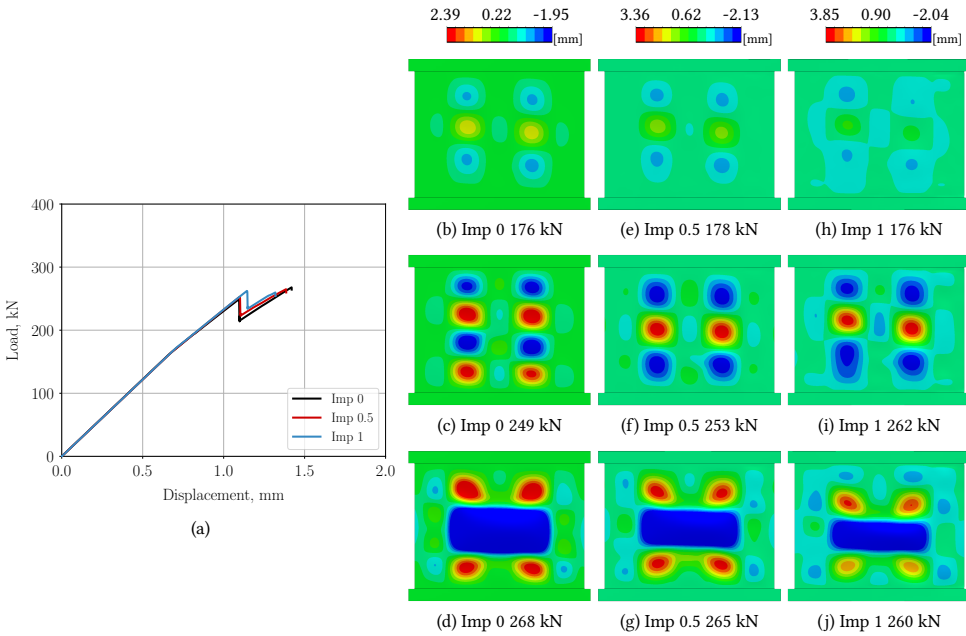


Figure 3.15: Panels with two 40 mm damages with a 110mm offset, and panel 2 imperfection: (a) load-displacement; (b-g) out-of-plane displacement contour plots.

3.6 TEST AND NUMERICAL RESULTS

This section reports the test results of the panels, compares them to the numerical results, and focuses on the effect of each configuration.

3.6.1 PANEL 1: PRISTINE PANEL

The load, as measured by the load cell and the average of the LDS displacement measurement, is analysed. The load-displacement behaviour of the pristine panel is reported in Figure 3.16. The panel has an approximate stiffness of 236 kN/mm, buckles at a load of 172 kN and fails at a load of 332 kN. At approximately 275 kN a small load drop is seen due to a sudden change in buckling shape. The numerical analysis is able to predict the overall structural behaviour well, but it does not predict the buckling shape change and resulting small load drop. This also leads to a larger difference in post-buckling stiffness, as the buckling shape change seen during the test also reduces stiffness.

The strains of the stringer cap are reported in Figure 3.17(a). The loading imperfection is small, and in the post-buckling range, there is a small jump in strains which is caused by the sudden buckling shape change. The strains under the stringers are reported in Figure 3.17(b). The strains underneath the stringer show equal loading and a drop in stiffness after buckling. The strains only diverge slightly and experience a sudden jump in strain due to a buckling-shape change.

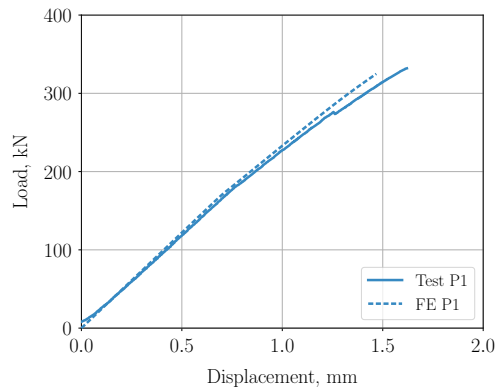


Figure 3.16: Load-displacement curves from tests and numerical analysis of pristine panel.

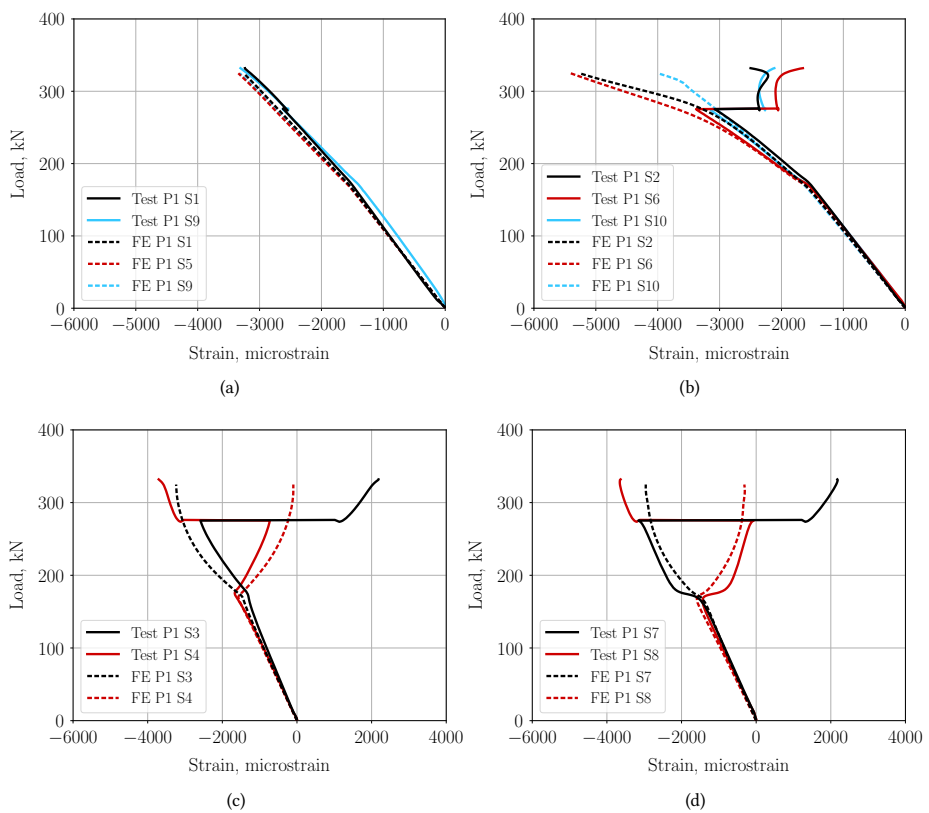


Figure 3.17: Experimental and numerical compressive strains of the pristine panel: (a) caps; (b) skin under stringer; (c) bay 1; (d) bay 2.

The strains in bay 1 show a large jump due to the buckling-shape change, as reported in Figure 3.17(c). This jump in strain is not seen in the numerical results, due to the lack of a buckling-shape change. The strains in bay 2, as reported in Figure 3.17(d), show a higher bending component compared to bay 1, with a similar jump in strains due to the buckling shape change. The strains, as predicted by the numerical analysis, are very similar but lack the jump in strain due to buckling shape change.

The numerical analyses are able to predict the overall strains well but present differences in the post-buckling field, due to buckling-shape changes and skin-stringer separation events.

The post-buckling shape and evolution of the panels are determined from the DIC measurement and compared to the results from the numerical analysis. The displacement is positive for inwards direction and negative for outwards direction, in line with the axis system reported in Figure 3.1. The panel presents an initial three half-wave buckling shape until approximately 275 kN, after which a sudden buckling shape change occurs with a four half-wave buckling shape, as reported in Figure 3.18. The numerical analysis predicts a three half-wave buckling shape. The number of half-waves underneath the stringer increases in the post-buckling field, similar to the test, but the buckling shape does not change.

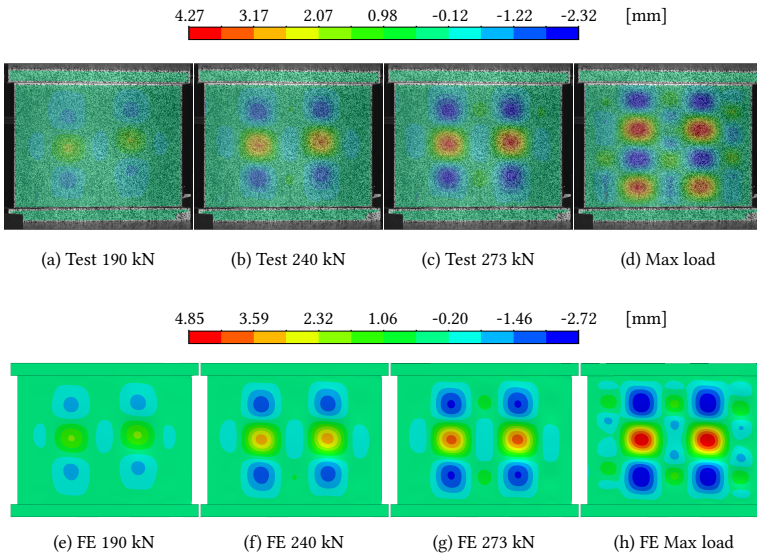


Figure 3.18: Experimental (a-d) and numerical (e-h) out-of-plane displacement of the pristine panel.

The start of final failure is captured at 10000 fps by a highspeed camera. It starts with skin-stringer separation in the right flange of the middle stringer, which is followed by separation in the left flange of the middle stringer, as reported in Figure 3.19(a-b). Before final failure occurs, small ticking sounds can be heard on the GoPro footage, indicating possible stable separation. The numerical analysis predicts the start of failure in the right stringer, as reported in Figure 3.19(c-d). This difference can be caused by the differences in imperfection and buckling shape.

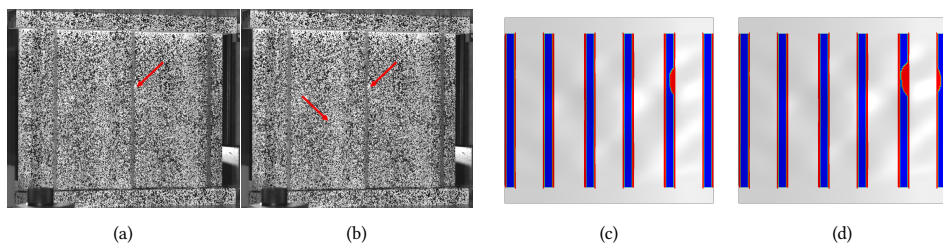


Figure 3.19: Comparison of failure behaviour of pristine panel: (a) start of failure during test; (b) propagation of failure during test; (c) start of failure in analysis; (d) propagation of failure in analysis.

The post-failure state is reported in Figure 3.20(a-b-c). All stringers have large separated areas, with more separation on the right-hand side of the panel. All stringers have fractures across the whole stringer width, and the flanges have large delaminations. The areas of the weld at the top of the panel have elliptical crack fronts.

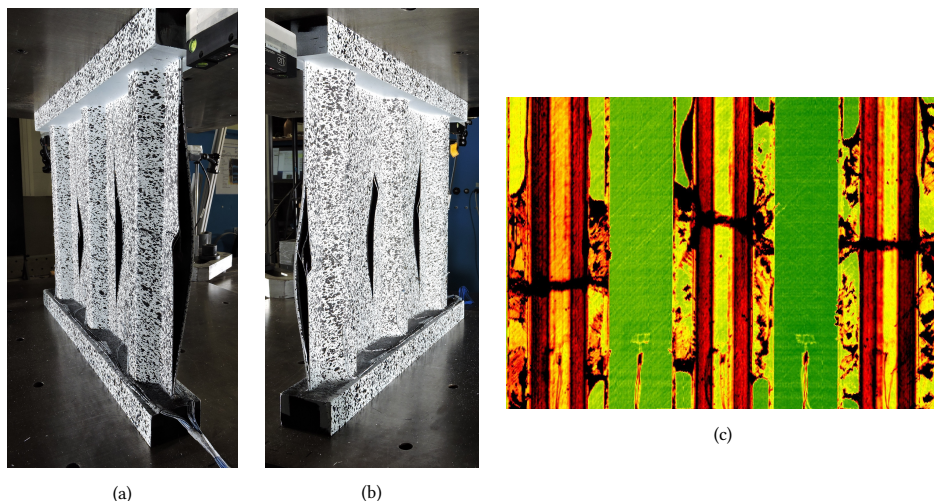


Figure 3.20: Post-failure of pristine panel: (a) photo from right side; (b) photo from left side; (c) c-scan.

3.6.2 PANEL 2: ONE INITIAL DAMAGE IN MIDDLE STRINGER

The load-displacement behaviour of the panel with one initial damage in the middle stringer is reported in Figure 3.21, in a comparison with the pristine panel. The panel has a stiffness of approximately 237 kN/mm and buckles at a load of 168 kN. Panel 2 fails due to skin-stringer separation at a load of 295 kN, while the pristine panel fails at a load of 332 kN. This is a reduction of the failure load of 11.2 % due to the damage in the flange of the middle stringer. The numerical analysis of panel 2 is able to predict the overall structural behaviour well. The biggest difference is seen for the failure load, which is conservative with a 6.4 % lower failure load compared to the test.

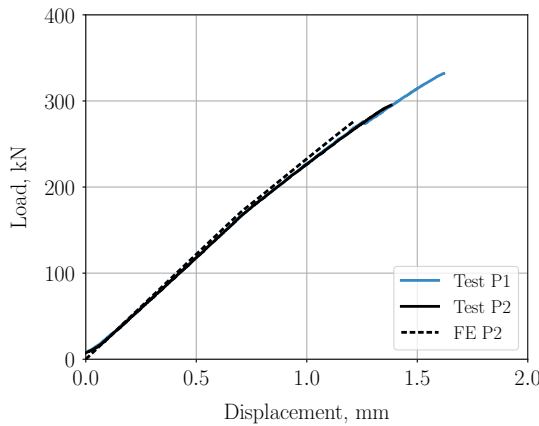


Figure 3.21: Load-displacement curves from tests and numerical analysis of panel 2.

The strains on the cap of the panel are reported in Figure 3.22(a), where it is seen that S9 shows lower strains compared to S1 and S5. A small loading imperfection can cause this difference. The strains under the stringers are equal, and there is no sign of unequal loading of the skin Figure 3.22(b). A slight drop in stiffness can be seen initially when buckling occurs after which the strains diverge, probably due to the different half-wave positions underneath each stringer, with more divergent behaviour close to the failure load.

The strains in bay 1 present slight divergent behaviour initially after buckling, as reported in Figure 3.22(c). When the buckling-shape further develops, the strains diverge more and experience a large bending component. The numerical prediction shows less divergent strains and in opposite direction, due to differences in buckling shape. The strains in bay 2 are reported in Figure 3.22(d). There is comparable behaviour to the strains in bay one, with slightly more divergent behaviour. The numerical prediction, however, predicts almost linear strains, with only a small bending component which switches sign several times.

The panel shows an initial three half-wave buckling shape, with the half-waves positioned towards the top of the panel, as reported in Figure 3.23. The buckling shape evolves to a four half-wave buckling shape, and just before final failure, the outwards half-waves in the bay and underneath the stringer start to connect. The numerical analysis predicts a three half-wave buckling shape, which evolves in terms of out-of-plane displacement magnitude and half-wave length. The difference in buckling shape compared to the test can be due to the differences in geometrical imperfection and loading imperfection.

The start of failure is reported in Figure 3.24(a), which is captured by a high-speed camera at 10000 fps. Separation starts in the right flange of the middle stringer, at the initial damage location. This is followed by separation of the left flange, as reported in Figure 3.24(b), and then the stringer further separates in upwards and downward directions. The numerical analysis also predicts this behaviour, as reported in Figure 3.24(c-d). There is an elliptical crack front shape for the separation at the initial damaged location and in the opposing flange.

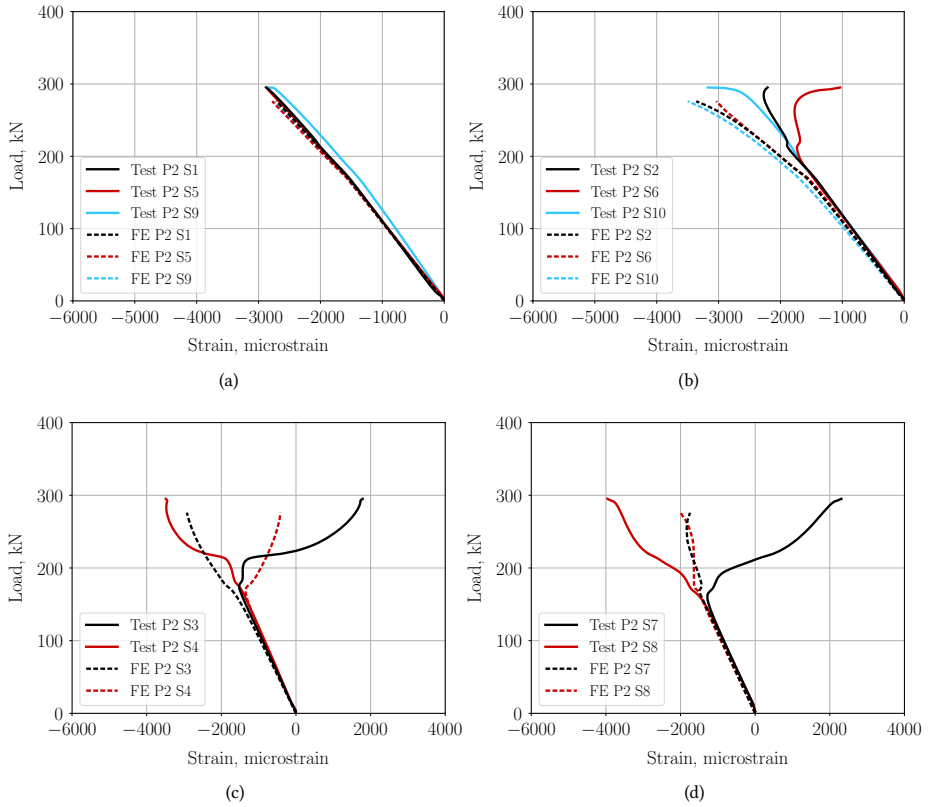


Figure 3.22: Experimental and numerical compressive strains of the panel 2: (a) caps; (b) skin under stringer; (c) bay 1; (d) bay 2.

The post-failure state of panel 2 is reported in Figure 3.25(a-b). It is seen that both the left and middle stringer have large separations. The left stringer has a larger separated area compared to the middle stringer, while the middle stringer had initial damage in the right flange. Final failure started with separation at the damaged location, which caused further large separations in the left-hand side of the panel. The right stringer's interface has some small separated areas, and the weld presents small elliptical fronts. The right flange of the left stringer shows material damage, with a fracture that starts from the lower radius to the flange edge.

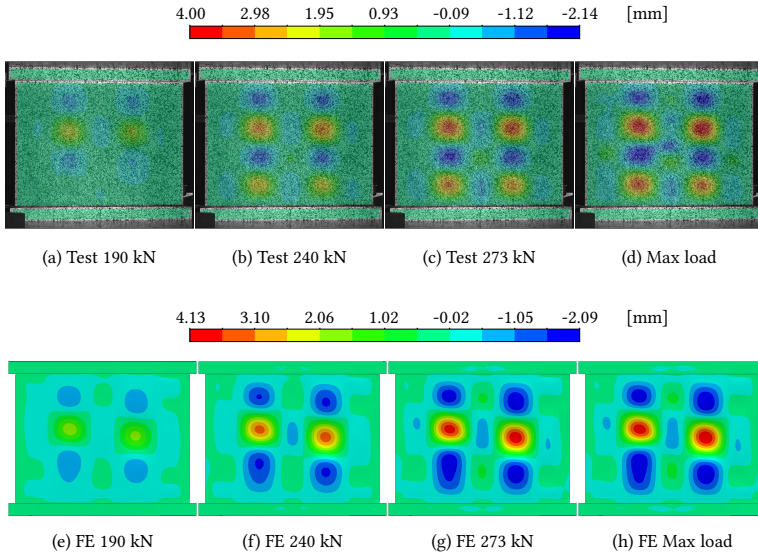


Figure 3.23: Experimental (a-d) and numerical (e-h) out-of-plane displacement of panel 2.

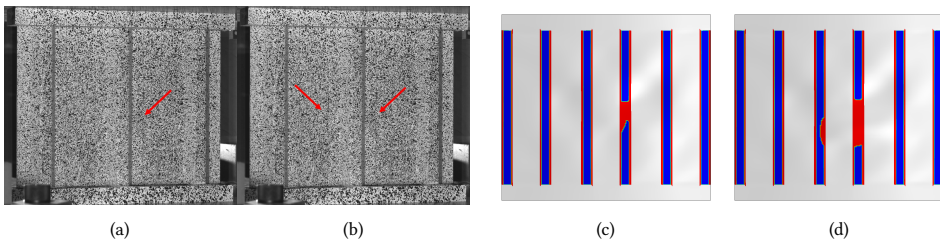


Figure 3.24: Comparison of failure behaviour of panel 2: (a) start of failure during test; (b) propagation of failure during test; (c) start of failure in analysis; (d) propagation of failure in analysis.

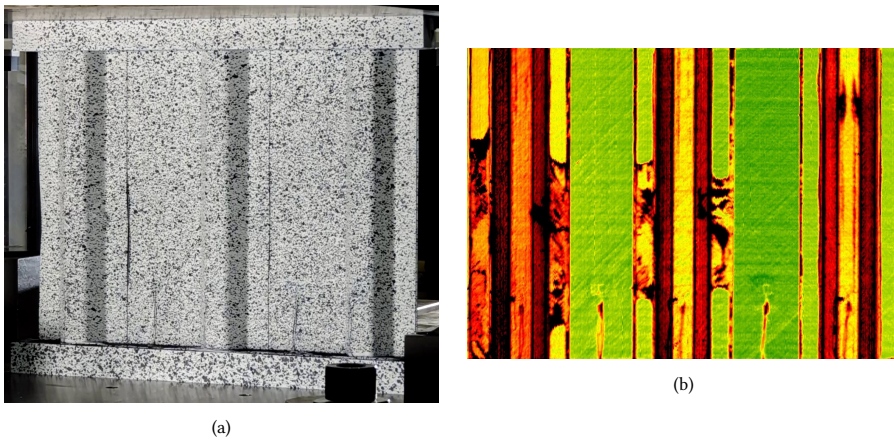


Figure 3.25: Post-failure of panel 2: (a) photo; (b) c-scan.

3.6.3 PANEL 3: TWO INITIAL DAMAGES IN MIDDLE STRINGER

The load-displacement behaviour of panel 3 is reported in Figure 3.26. Panel 3 has a stiffness of approximately 236 kN/mm, and it buckles at a load of 173 kN. The panel experiences a maximum load of 277 kN at 1.29 mm of displacement, after which a load drop occurs. The panel fails at a load of 270 kN and 1.48 mm of displacement. This maximum load is 16.6 % lower compared to the pristine panel. The numerical analysis predicts similar behaviour with a load drop due to a skin-stringer separation event before final failure. It is, however, seen that this load-drop occurs at a lower load, and the maximum load is 5.8% lower compared to the test.

3

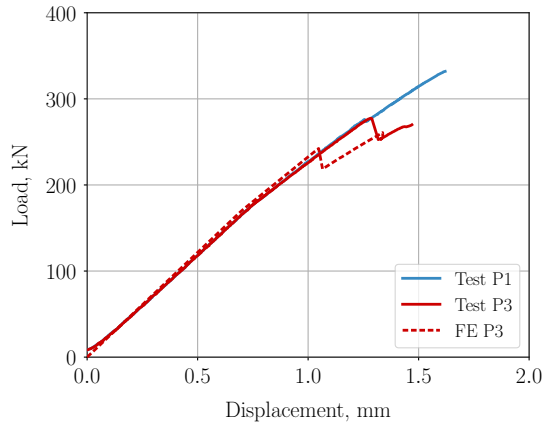


Figure 3.26: Load-displacement curves from tests and numerical analysis of panel 3.

The strains on the caps of the panels are reported in Figure 3.27(a). It is seen that there might be a small loading imperfection, and a load drop due to a skin-stringer separation event. The strains underneath the stringer are reported in Figure 3.27(b). Before buckling a minor difference in strains can be seen in the skin, indicating a small loading imperfection. After buckling the strains diverge, with large strain changes in the post-buckling field. These large changes are caused by the skin-stringer separation event, which also leads to a load drop.

The strains in bay 1 start to diverge immediately after buckling, and show jumps in strain due to the skin-stringer separation event, as reported in Figure 3.27(c). The numerical analysis predicts similar behaviour initially, although with opposite bending component, and larger jumps in strain in the post-buckling field. The strains in bay 2 present a high bending component in the post-buckling field, as reported in Figure 3.27(d). A strain jump occurs due to the skin-stringer separation event, with S7 also presenting an increase in strains just before the separation event. The numerical analysis predicts an opposite bending component with larger jumps of strain in the post-buckling field due to the skin-stringer separation event.

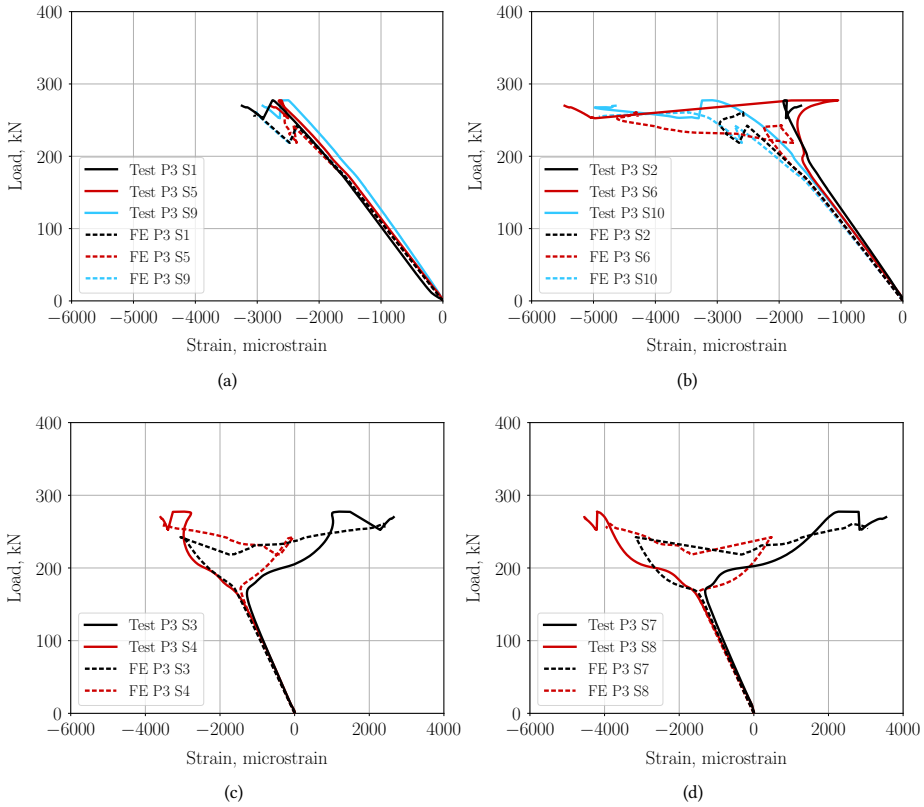


Figure 3.27: Experimental and numerical compressive strains of the panel 3: (a) caps; (b) skin under stringer; (c) bay 1; (d) bay 2.

Panel 3 shows a four half-wave initial buckling shape, with the fourth half-wave barely visible in bay two, as reported in Figure 3.28. At higher load levels the fourth half-waves become more prominent. At 277 kN the initial damage opens, with the outward half-waves in the bay and underneath the stringer connecting. After the skin-stringer separation event there is large out-of-plane displacement in the middle of the panel, due to the separation between skin and stringer. At 270 kN, just before final failure, the large half-wave in the middle of the panel grows towards the side of the panel. The numerical analysis predicts a three half-wave buckling shape, with an anti-clock-wise skew in terms of half-wave position. At 218 kN, after the skin-stringer separation event, a large area of high out-of-plane displacement is seen, similar to the test results. At 263 kN the area of high out-of-plane displacement has moved upwards, indicating separation growth in an upwards direction.

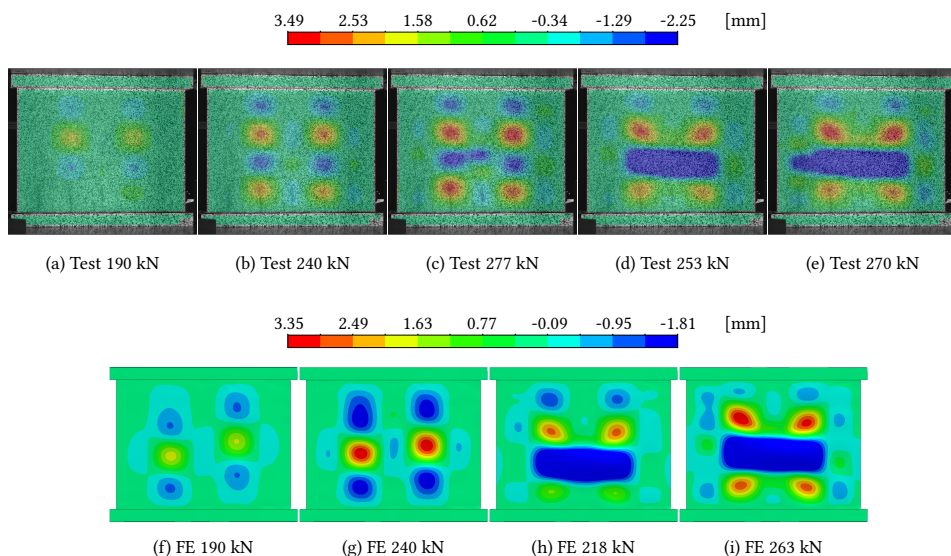


Figure 3.28: Experimental (a-e) and numerical (f-i) out-of-plane displacement of panel 3.

Panel 3 endured a skin-stringer separation event of the middle stringer, which did not lead to panel collapse, as reported in Figure 3.29(a). The event started with stable crack growth, heard on the GoPro camera footage, for approximately 15 seconds. This stable crack growth seems to occur at the initial damage in the middle of the panel, as DIC measured an increase in out-of-plane displacement at this location. The stable crack growth is followed by unstable crack growth that results in a large separated area. After loading continued, final failure occurred with further separation of the middle stringer, followed by separation of the right stringer, as reported in Figure 3.29(b). Similar behaviour is predicted by the numerical analysis, as reported in Figure 3.29(c-d). Both flanges of the middle stringer separate initially, and final failure starts by separation of the right stringer.

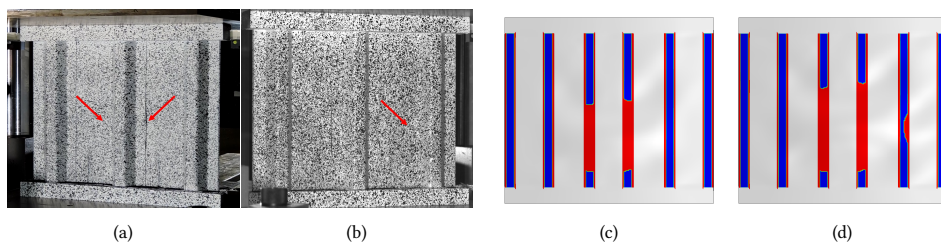


Figure 3.29: Comparison of failure behaviour of panel 3: (a) start of failure during test; (b) propagation of failure during test; (c) start of failure in analysis; (d) propagation of failure in analysis.

The post-failure state of panel 3 is reported in Figure 3.30(a-b-c). The middle and right stringer present large separated areas, with the right stringer having the largest separated area. The right stringer also presents two fractures across the stringer, in the middle of the

panel. All flanges which have separated also have delaminations of the stringer flanges. The left stringer has no visible separations and no material damage.

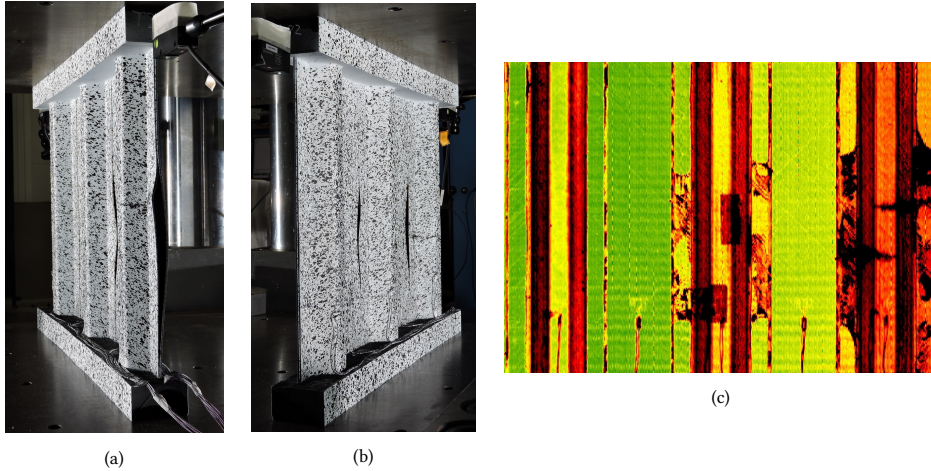


Figure 3.30: Post-failure of panel 3: (a) photo right side; (b) photo left side; (c) c-scan.

After the test, the middle stringer of panel 3 is removed to investigate the fracture surfaces of the failed welds. The weld can be distinguished by the rough surface with visible fibres Figure 3.31 (b). The area in between the red dashes corresponds to the area that separated during the test. The two yellow foils of the initial damage are visible on the skin, while on the stringer two smooth areas can be seen that correspond to the same initial damage locations. The areas in between the purple and green dashes are highlighted in Figure 3.31 (a) and (c), respectively. The skin is mostly intact in the area that separated in the test, with limited fibre pullout and no obvious delaminations. The stringer has a few locations with delaminations, and small pieces of the stringer ply remain on the skin. The bottom 0 ply of the stringer is visible in a few small areas where the bottom 45 ply has delaminated.

On the fracture surfaces, lighter and darker areas can be identified. There are lighter areas around the middle initial damage and the opposite weld, with an elliptical shape. These areas correspond to the location where DIC measured higher out-of-plane displacement before the first separation event. This might indicate that the lighter areas are caused by stable crack growth, while the darker areas are due to unstable crack growth.

On the fracture surface on the opposite side of the middle initial damage, next to the elliptical lighter area associated with the stable crack growth, dark elliptical marks can be seen. These markings indicate crack growth with an elliptical crack front shape. The crack growth seems to go in a sideways direction towards the bay and a downward direction towards the second initial damage location.

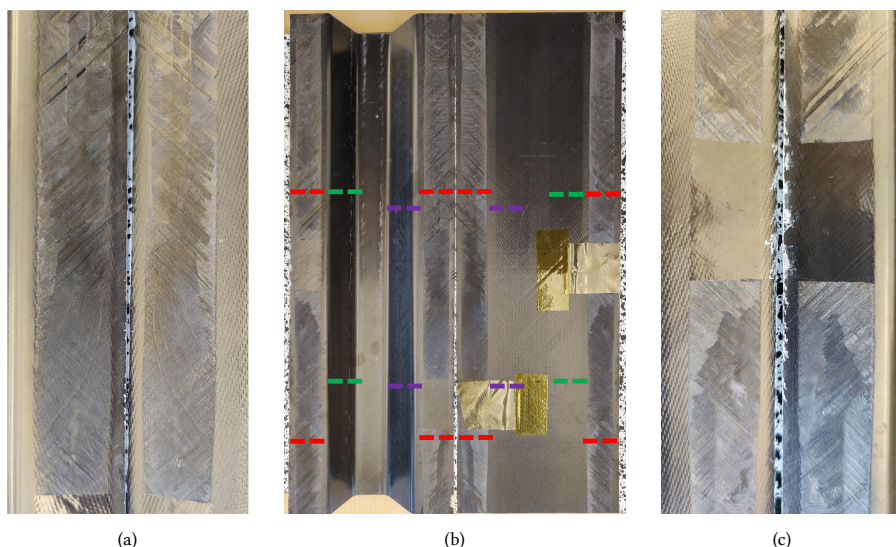


Figure 3.31: Fracture surface of welds of middle stringer of panel 3; (a) close-up of the area between purple dashes; (b) fracture surfaces of middle stringer, with the stringer and skin on the left and right side respectively, with red dashes indicating the area that separated in the test; (c) close-up of the area between green dashes.

3.6.4 PANEL 4: ONE DAMAGE IN SIDE STRINGER

The load-displacement behaviour of panel 4 is reported in Figure 3.32. Panel 4 has an approximate stiffness of 236 kN/mm before buckling. It buckles at a load of 177 kN and fails at a load of 284 kN. This is a reduction of 14.5 % in comparison to the pristine panel failure load. The numerical analysis over-predicts the failure load by 9.3 %, which is the largest difference between numerical results and test results of all panels. This might be due to the location of the damage, which is in one of the side stringers.

The strains of the stringer caps are reported in Figure 3.33(a). They are comparable to the previous panels, with a small reduction in strains of S9 just before final failure. The strains under the stringers are reported in Figure 3.33(b). In post-buckling they present jumps and divergent behaviour due to buckling shape changes, and a sudden increase just before final failure.

The strains in bay 1 show convergent behaviour initially after buckling, as reported in Figure 3.33(c). Then they suddenly diverge considerably with a large bending component. The numerical analysis predicts diverging strains immediately after buckling, with a jump in the post-buckling field.

The strains in bay 2 present similar behaviour to bay 1, as reported in Figure 3.33(d). In post-buckling, they present an initial small bending component, after which the strains diverge due to high bending levels. The numerical analysis predicts divergent strains at a lower load, indicating buckling in the bay starts at a lower load than the test.

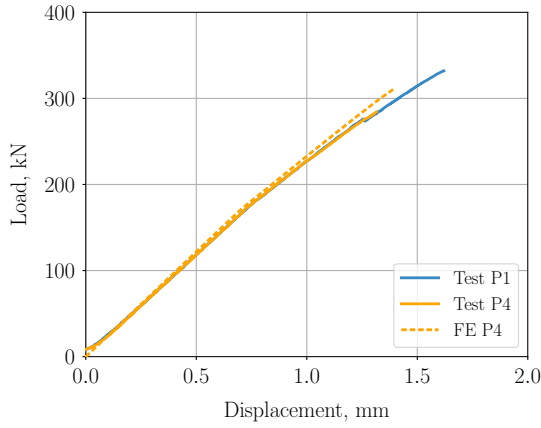


Figure 3.32: Load-displacement curves from tests and numerical analysis of panel 4.

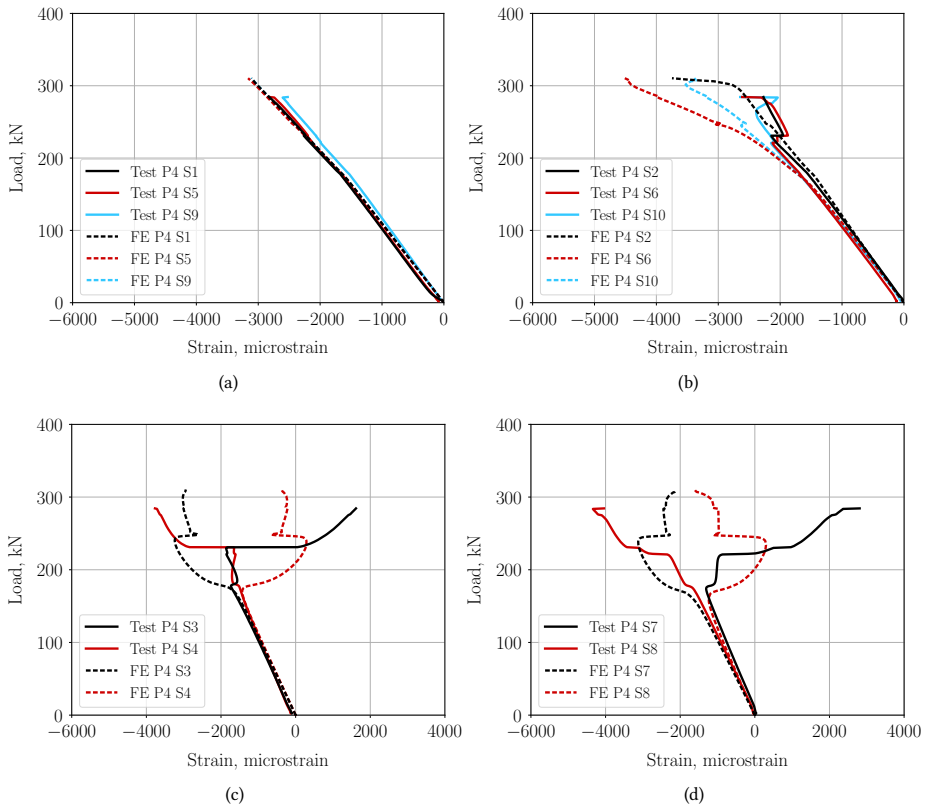


Figure 3.33: Experimental and numerical compressive strains of the panel 4: (a) caps; (b) skin under stringer; (c) bay 1; (d) bay 2.

The panel has an initial three half-wave buckling shape, with the half-waves positioned towards the top of the panel, as reported in Figure 3.34. The bottom inwards half-waves have a higher half-wave length, and at higher loads the fourth half-waves appear at this position. At the maximum load the damage in the stringer opens, with inward half-waves connecting between the bay and underneath the stringer. The numerical analysis predicts a three half-wave buckling shape, with the half-waves initially positioned towards the bottom of the panel. At higher load levels, the half-waves evolve towards the top of the panel, and the number of half-waves underneath the stringer increases.

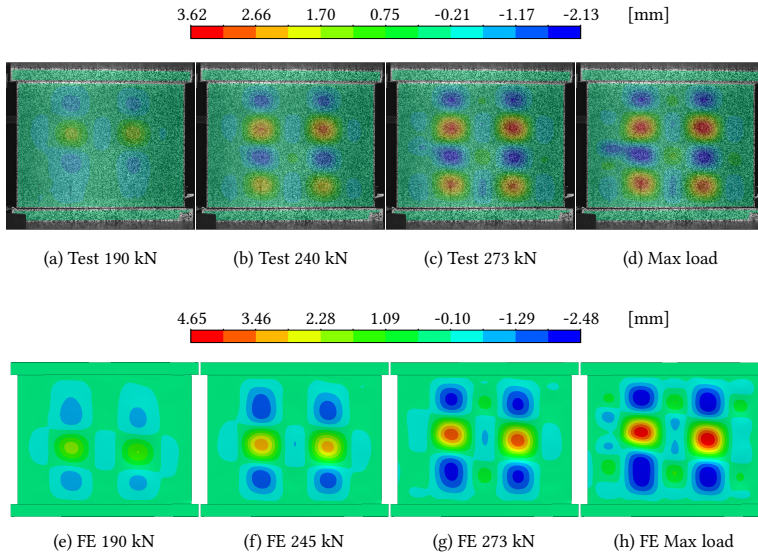


Figure 3.34: Experimental (a-d) and numerical (e-h) out-of-plane displacement of panel 4.

The final failure is captured by the high-speed camera and starts in the left flange of the right stringer, where the initial damage is located, as reported in Figure 3.35(a). This is followed by the separation of the right flange of the same stringer, Figure 3.35(b). Before final failure occurs, a ticking sound can be heard on the GoPro footage, indicating stable separation. The numerical analysis predicts the same start location at the initial damage, Figure 3.35(c). Then separation starts in the right flange of the right stringer and in the middle stringer’s left flange, as reported in Figure 3.35(d). This behaviour was not seen during the test.

The post-failure state of panel 4 is reported in Figure 3.36(a-b). Only the right stringer has large separated areas, with a fracture in the right flange. The middle stringer welds present small separations at the inner weld edge, as the weld becomes slightly narrower in some areas.

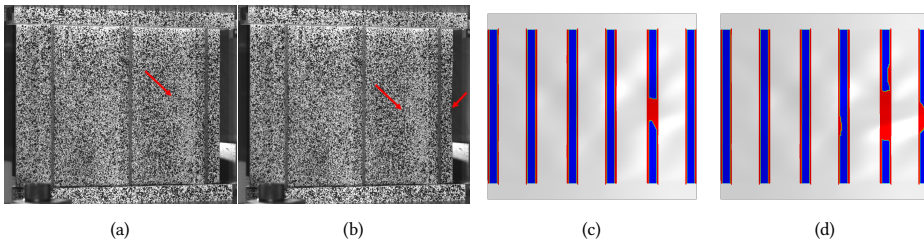


Figure 3.35: Comparison of failure behaviour of panel 4: (a) start of failure during test; (b) propagation of failure during test; (c) start of failure in analysis; (d) propagation of failure in analysis.

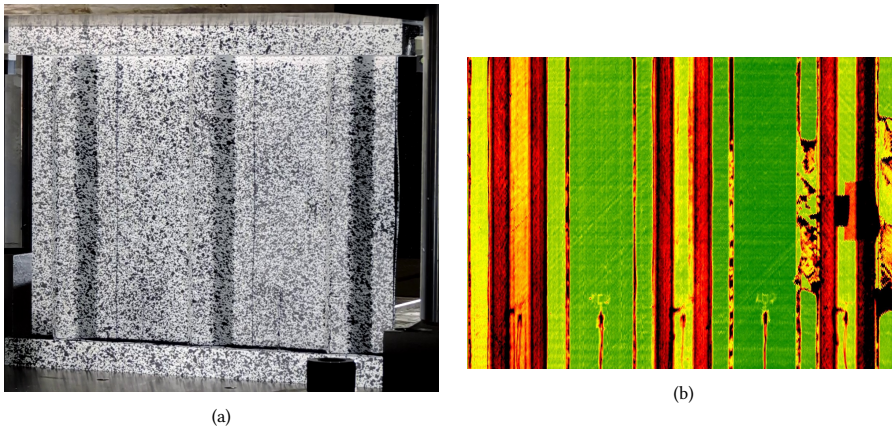


Figure 3.36: Post-failure of panel 4: (a) photo; (b) c-scan.

3.7 SUMMARY AND DISCUSSION

The pre-buckling stiffness, buckling load and maximum loads of the four tests and numerical analyses are reported in Table 3.6. The panels show a similar stiffness of approximately 236 kN/mm, and the numerical analysis overpredicts the stiffness by 3.1% on average. The buckling load varies slightly between the panels, which can be caused by differences in initial damage and imperfections. The numerical analysis predicts the buckling load accurately, with a maximum difference of 2.8 %.

The failure load is highly affected by the initial damage, with one and two damages of 40 mm in the middle stringer decreasing the failure load by 11.2 % and 16.6 %, respectively, compared to the pristine panel. The damage in the side stringer decreases the failure load by 14.5%. The numerical analyses predict all failure loads within 10%, with the largest differences for panel 4, with an overprediction of 9.3%. The failure loads of the other three panels are predicted conservatively, with a maximum difference of 6.4%.

The post-buckling strains underneath the stringer and in the bays are highly affected by the buckling shape, which in turn can be affected by the location of the initial damage. Each damaged configuration shows different behaviour due to the different damage locations, and the numerical prediction has difficulty predicting the exact buckling shape.

Table 3.6: Pre-buckling stiffness, buckling load and maximum load from tests and numerical analysis.

	Pre-buckling stiffness			Buckling load			Maximum load		
	Test [kN/mm]	FE [kN/mm]	Diff. [%]	Test [kN]	FE [kN]	Diff. [%]	Test [kN]	FE [kN]	Diff. [%]
Panel 1	236.4	243.9	3.2	172	170	1.2	332	325	2.1
Panel 2	236.8	243.7	2.9	168	170	1.2	295	276	6.4
Panel 3	236.4	243.5	3.0	173	171	1.2	277	261	5.8
Panel 4	236.4	243.8	3.1	177	172	2.8	284	310	9.3

All panels show a four half-wave buckling shape in the test. The fourth half-wave appears gradually for all damaged configurations, while the pristine panel endured a sudden jump from three to four half-waves. The initial damage locations appear to "attract" the half-waves and the opening of the initial damage can be seen from the DIC measurement. The opening seems to grow, indicating that stable separation occurs followed by unstable skin-stringer separation. Indications of stable separation can be heard from the GoPro footage of all panels with initial damage, and most notable on the footage of panel 3. The fracture surface of panel 3 also showed lighter areas around the damage location, indicating stable separation growth. It is however difficult to determine how much separation growth occurs before final failure, without utilising other measurement techniques more specifically for capturing damage growth.

The numerical analysis has difficulty predicting the influence of the initial damage on the buckling shape. Instead of predicting four half-waves, the three half-wave buckling shapes show longer half-wave lengths, for the outwards half-waves close to the locations with initial damage. These structures are highly sensitive to imperfections, and the difference between test and analysis might be caused by how, and which imperfections are included in the analysis. The geometrical imperfections, introduced in the analysis, are measured from the skin-side. Also, the initial damage is modelled as a perfect sharp crack, and no foil is simulated, which can influence the effect of the initial damage on the weld.

All panels fail due to skin-stringer separation. Panel 3, with two initial damages, showed a skin-stringer separation event of the middle stringer, where both welds separated approximately from the bottom to the top damage. This, however, did not lead to stringer failure, and the panel collapsed due to skin-stringer separation after more load was applied.

3.8 CONCLUDING REMARKS

This research analyses and tests four thermoplastic stiffened panels to investigate the damage tolerance of the welded joint.

The sensitivity studies show that the initial damage location mainly influences the skin-stringer separation initiation load for panels with one initial damage, while the final failure load is less affected. When there are two initial damages, the damage at the middle of the panel seems critical for final failure, and the second damage location influences the skin-stringer separation initiation load.

The damage size sensitivity study considered up to a maximum damage size of 100 mm, which allowed for buckling before the start of failure. The geometrical imperfection

lowers the failure load for pristine panels, while the failure load increases for panels with initial damage. Damage sizes above 40 mm show stable separation growth. This seems to delay final failure, as the initiation load decreases more compared to the failure load for larger initial damage.

Then the four panels are tested, three with initial damage and one in pristine condition. The initial damage mainly influences the failure load, with the stiffness and buckling load not considerably affected. The failure load decreased up to 16.6 %, for the panel with two damages. Including a second initial damage location increases the criticality of the initial damage in the middle of the panel, as separation still seems to start from the middle location. The panel with one initial damage in the side stringer showed a lower failure load compared to the panel with initial damage in the middle stringer. This can be considered surprising, as the middle stringer is expected to attract more load and therefore be more critical for damage.

The initial damage seems to make buckling shape changes more gradually, possibly due to the opening of the damage, which can be seen on the DIC measurements. The panels with initial damage also show stable separation growth before final failure.

The panel with two initial damages showed that the middle stringer can endure a considerable skin-stringer separation event without visible damage. This can be aided by the lower load the event occurs at, leading to less load redistribution within the structure. Also, the separation event seemed to be contained by the initial damages.

The numerical analysis is able to predict the overall structural behaviour well. It does, however, have difficulty predicting the buckling shape change to four half-waves. The failure loads of panels with initial damage in the middle stringer are predicted conservatively, while it over-predicts the failure load of the panel with initial damage in the side stringer.

This research shows that the welded joint can withstand buckling deformation far into the post-buckling field with one or two initial damages of 40 mm. It should, however, be said that the damage size was chosen conservatively because of the unknowns concerning the weld strength at the time of manufacturing. Nonetheless, the numerical analysis showed good predictions of failure load, and predicted that panels with larger damage sizes can still withstand load into the post-buckling field. This shows great promise for thermoplastic composite primary structures, also taking into account the damage tolerance behaviour.

ACKNOWLEDGEMENT

This project has received funding from the Clean Sky 2 Joint Undertaking (JU) under grant agreement No 945583. The JU receives support from the European Union's Horizon 2020 research and innovation programme and the Clean Sky 2 JU members other than the Union.

The authors thank GKN Fokker and NLR - Netherlands Aerospace Centre, for their cooperation and manufacturing of the test panels.

DISCLAIMER

The results, opinions, conclusions, etc. presented in this work are those of the authors only and do not necessarily represent the position of the JU; the JU is not responsible for any use made of the information contained herein.

4

DESIGN, ANALYSIS AND TESTING OF THERMOPLASTIC WELDED STIFFENED PANELS TO INVESTIGATE SKIN-STRINGER SEPARATION IN POST-BUCKLING

4

Two aeronautical thermoplastic composite stiffened panels are analysed and tested to investigate the buckling behaviour, the skin-stringer separation and the final failure mode. The panels are made of fast crystallising polyetherketoneketone carbon composite, have three stringers with an angled cap on one side, and are joined to the skin by a short-fibre reinforced butt-joint. The panels contain an initial damage in the middle skin-stringer interface representing barely visible impact damage. Finite element analysis using the virtual crack closure technique are conducted before the test to predict the structural behaviour. During the tests, the deformation of the panels is measured by digital image correlation, the damage propagation is recorded by GoPro cameras and the final failure is captured by high speed cameras. The panels show an initial three half-wave buckling shape in each bay, with damage propagation starting shortly after buckling. A combination of relatively stable and unstable damage propagation is observed until final failure, when the middle stringer separates completely and the panels fail in an unstable manner. The test results are compared to the numerical prediction, which shows great agreement for both the buckling and failure behaviour.

4.1 INTRODUCTION

Composite structures are nowadays used in the aeronautical field for primary structures such as wing and fuselage. These primary structures utilise thin-walled designs, consisting of a skin with stiffening elements which can have a wide variety of shapes with open and closed cross-sections. Thin-walled structures are prone to buckle under compression and shear loads and buckling is generally avoided. Allowing primary structures to operate in the post-buckling field below ultimate loads could lead to a significant reduction of weight. This, however, requires a complete understanding of the structural behaviour in the post-buckling field as it is often seen that failure occurs after buckling [39, 48].

This paper considers the experimental test and analysis of two thermoplastic composite stiffened panels, to get a better understanding of the buckling behaviour and skin-stringer separation of thermoplastic panels. This research contributes to the development of thermoplastic composites for aeronautical structures, and to set the next step towards composite structures designed for post-buckling. The combination of different material properties and different manufacturing techniques of thermoplastic composites, compared to thermoset composites, can lead to considerably different structural behaviour. This difference in failure behaviour has been demonstrated in literature mainly at coupon levels, for example on impact tests [49] and tensile specimens [50]. It is, therefore, not well known if the analysis methods used for the more classical thermoset composites are applicable for thermoplastic composites, and if the interaction between the buckling and failure behaviour shows similarities.

One of the most common failure modes in the post-buckling field for stiffened panels is skin-stringer separation [12]. Due to the skin out-of-plane displacement caused by buckling, high stresses occur in the interface between the skin and stringer, which can lead to separation. Skin-stringer separation is researched mainly on thermoset composite materials, which show a more brittle failure behaviour in comparison to thermoplastic composite materials [14, 15, 37].

Orifici et al. [25, 51] investigated single-stringer specimens with a blade stringer, both in pristine and damaged configuration with a debond, which showed skin-stringer separation in post-buckling. The pristine panels collapsed when separation started, while the damaged panels exhibited debond growth before collapse. Riccio et al. [26] presented a numerical procedure for skin-stringer separation, which included coupon level tests such as Double Cantilever Beam (DCB) and End Notched Flexure (ENF), and also compared the experimental data of Orifici et al. [25, 51] for validation of the single-stringer specimen numerical analysis. The numerical procedure utilised continuum shell elements and skin-stringer separation was modelled by the Cohesive Zone Model (CZM), and achieved excellent correlation. The design and analysis of multi-stringer panels with blade stringers was investigated by Degenhardt et al. [27]. The experimental data of this work were later used by Orifici et al. [28] for validation of the numerical prediction for skin-stringer separation in post-buckling. Correlation of the post-buckling behaviour proved to be difficult due to the influence of geometric imperfections.

Recent work on skin-stringer separation utilises single-stringer specimens with an omega stiffener. Single-Stringer Compression Specimens (SSCS) were designed by Bisagni et al. [29, 40], utilising finite element analysis of multi-stringer panels to determine the desired buckling and failure behaviour of the specimens. A total of six SSCS were tested,

with and without artificial defects, until collapse. The numerical prediction utilised CZM for skin-stringer separation and a continuum damage model for stiffener crippling and showed good correlation with the tests for both failure modes. The SSCS were further numerically investigated by Vescovini et al. [13], to improve computational efficiency by using a simplified model and introducing a global/local damage analysis. These methods allowed for an efficient parametric study of the effect of structural design and numerical parameters on the buckling, post-buckling and failure behaviour. Dávila and Bisagni [52] presented a combined experimental and numerical investigation for damage tolerance, where numerical analysis were conducted to determine a selection of initial damage sizes and load levels for the fatigue tests. The numerical analysis made use of the Virtual Crack Closure Technique (VCCT) to model skin-stringer separation. Raimondo et al. [30] presented a numerical study utilising the experimental results by Dávila and Bisagni [52], investigating skin-stringer separation due to fatigue using a VCCT based approach. Another method of investigating skin-stringer separation on single-stringer specimens is applying directly the out-of-plane displacement on the skin, as researched by Kootte and Bisagni [53], instead of inducing buckling by longitudinal compression.

The majority of research on thermoplastic composite materials for stiffened structures focuses on the design of the structures, the evaluation of manufacturing processes and the resulting performance [18–20]. More research has been conducted on coupons [10, 54] and small elements [55]. The main advantages of thermoplastic materials lay in the high toughness [10], leading to less brittle failure behaviour, the chemical resistance and expanded manufacturing possibilities such as thermoplastic welding [9], hot press forming and co-consolidation processes [3, 4]. These manufacturing techniques can result in cost reduction due to a lower number of parts to assemble and out-of-autoclave manufacturing possibilities.

In recent years two projects on thermoplastic aeronautical structures, TAPAS 1 [3] and TAPAS 2 [4], have been successfully conducted in the Netherlands. TAPAS 1 investigated the required manufacturing technology for thermoplastic primary structures, delivered a fuselage shell demonstrator and torsion box demonstrator, which both use the newly developed butt-joint concept. TAPAS 2 considered a thermoplastic orthogrid fuselage shell with new stiffening and joining methods, including the butt-joint concept. This resulted in a fuselage design without fasteners and it shed the need of a so called "mouse hole" in the frame of the fuselage through which the stringer would pass.

The further development of thermoplastic composites for primary structures is explored in the ongoing Clean Sky 2 "SmarT mUlti-fuNctioNal and INtegrated TP fuselaGe" STUNNING project, which focuses on developing the lower half of a thermoplastic multi-functional fuselage demonstrator [7]. Within STUNNING, the performance of thermoplastic composite structures is linked to the manufacturing processes, such as thermoplastic welding and co-consolidation, and a combined experimental and numerical methodology is under development to analyse primary thermoplastic composite structures in post-buckling [56, 57].

The thermoplastic stiffened panels investigated in this research have three stringers, with a butt-joint and angled cap. The panels are designed and manufactured by GKN Fokker [5]. The panels include an initial damage in the middle skin-stringer interface, that is representative of Barely Visible Impact Damage (BVID). The buckling and failure

behaviour of the panels is analysed by the use of Finite Element (FE) analysis, in which skin-stringer separation is modelled using the VCCT approach [35, 36]. The experimental tests make use of Digital Image Correlation (DIC) to capture the deformation field during buckling. Skin-stringer separation is recorded by cameras, and panel final failure is captured by the use of two high-speed cameras. The FE analysis and the tests were performed at the Delft University of Technology.

Preliminary analysis results of the first panel were presented by van Dooren et al. [56]. The current study includes the refinement of the analysis of the first panel, the analysis of the second panel and the test campaign.

4.2 PANEL GEOMETRY AND MATERIAL

The thermoplastic composite stiffened panels investigated in this work are representative of a business jet fuselage section [5]. The panels have three stringers, with each stringer consisting of a vertical web and an angled side cap, and are joined to the skin with a butt-joint. The panels have two potting tabs, moulded to each end of the panel for load introduction during testing. One of the panels is shown in Figure 4.1.



Figure 4.1: Thermoplastic composite stiffened panel.

The panels are 495.3 mm long including the potting, 445.3 mm long in between the potting, 344.8 mm in width and the stringer spacing is 152.4 mm, as shown in Figure 4.2. The web is 28 mm in height, the cap is 15 mm wide and is angled upwards at 105 degrees w.r.t. the web, as shown in Figure 4.3. Short fibre filler material joins the laminates of the stringer and skin, to constitute the so-called butt-joint. The panels have an initial damage in between the bottom of the filler and the top of the skin at the middle stringer, as highlighted by the red area. The initial damage is approximately 70 mm long and is considered a typical damage size to represent BVID for this design. To determine the BVID size, impact tests were performed by GKN Fokker on a larger structure using an indenter with a diameter of 1/2 inch to obtain an initial indent depth of 1 mm, which is assumed to be at least 0.3 mm after material relaxation [58]. For the larger structure with 15 ply skin, an impact from the inside with a dent depth of 1 mm resulted in a 70 mm crack. Consequently, the initial damage for these three-stringer panels is created by inserting a 40

mm Teflon insert during manufacturing. After manufacturing the damage is extended in a testing machine to a length of approximately 70 mm by applying out-of-plane displacement to the skin. This method creates a sharp crack tip to represent more closely BVID.

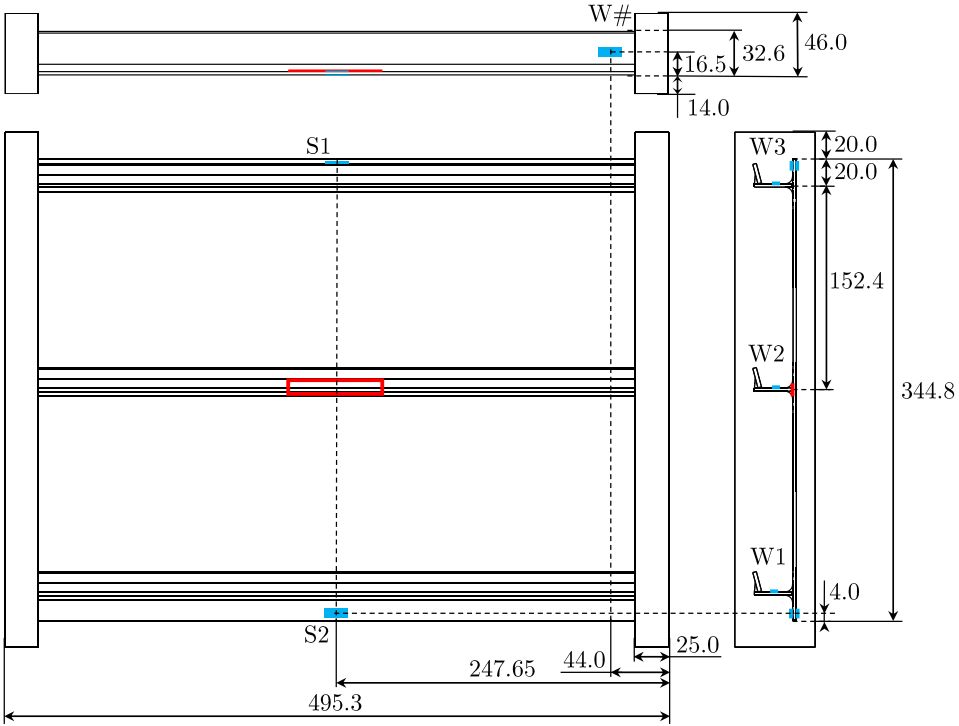


Figure 4.2: Geometry of thermoplastic composite stiffened panel (dimensions in mm), with initial damage location and strain gauges highlighted in red and blue, respectively.

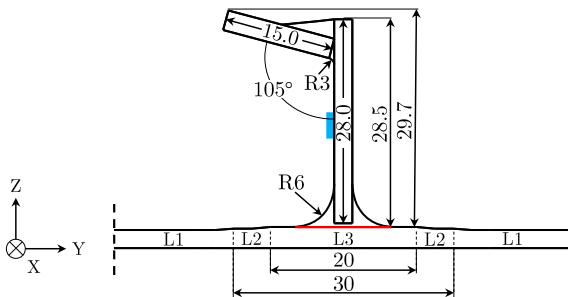


Figure 4.3: Stringer cross-section (dimensions in mm), with initial damage location and strain gauges highlighted in red and blue, respectively.

The skin is manufactured by advanced fibre placement and the stringer sections consist of pre-forms, which are cut by a waterjet from flat laminates. The stringer sections and

filler profiles are assembled in an inner mould and held in place with tooling blocks. The skin is laid on top of the assembled mould with additional glass fibre fabric patches applied on the outer mould side of the skin at the joint locations to improve surface flatness of the skin after manufacturing. The whole section is then vacuum bagged, and co-consolidated in one step in an autoclave. The panels have an additional step purely for test preparation, where epoxy potting is applied to the end of the panels, by placing each end of the panel inside a female rectangular mould which is filled with epoxy.

All the laminated sections are made from Fast Crystallizing PolyEtherKetoneKetone (PEKK-FC) carbon fibre (ASD4) UniDirectional (UD) and are joined by carbon Short Fibre Reinforced Plastic (SFRP) filler PEKK extrusion profiles. The material properties of the AS4D/PEKK-FC UD and the filler are supplied by GKN Fokker, based on internal characterisation, and are reported in Table 4.1 and Table 4.2, respectively. The assumed material properties of the glass fabric PEKK are reported in Table 4.3. The laminated sections consist of quasi-isotropic layups which are reported in Table 4.4. The skin has three different layups, named L1, L2 and L3, due to the additional glass fabric plies in the stringer region.

Table 4.1: AS4D/PEKK-FC carbon UD ply properties.

E_{11} [MPa]	E_{22} [MPa]	ν_{12} [-]	G_{12} [MPa]	ρ [kg/m ³]	t_{ply} [mm]
126100	11200	0.3	5460	1560	0.138

Table 4.2: PEKK carbon SFRP filler properties.

E_{11} [MPa]	$E_{22} = E_{33}$ [MPa]	ν_{12} [-]	G_{12} [MPa]	ρ [kg/m ³]
13252	6579	0.42	2389	1560

Table 4.3: PEKK glass fabric ply properties.

E_{11} [MPa]	E_{22} [MPa]	ν_{12} [-]	G_{12} [MPa]	ρ [kg/m ³]	t_{ply} [mm]
25000	25000	0.3	3000	2200	0.1

Table 4.4: Layups and total nominal thicknesses of panel sections, with C and G superscript for carbon and glass plies respectively.

Section	Thickness [mm]	Layup
Skin L1	2.484	[45/-45/0/45/90/-45/45/0/-45] ^C s
Skin L2	2.684	[0 ₂] ^G [45/-45/0/45/90/-45/45/0/-45] ^C s
Skin L3	2.884	[0 ₄] ^G [45/-45/0/45/90/-45/45/0/-45] ^C s
Web	2.484	[45/90/-45/0/45/0/-45/0/45/-45] ^C s
Cap	2.760	[45/90/-45/0/45/0/-45/0/0/90] ^C s

4.3 GEOMETRICAL IMPERFECTIONS

Before the tests, the geometrical imperfections of the panels, considered as the deviation with respect to the nominal design, are measured. This allows to determine the effect of the manufacturing process, and to implement the imperfections in the FE model to improve the accuracy of the prediction.

The geometrical imperfections are measured by DIC. The nominal design of the skin is flat, and the geometrical imperfections are therefore measured as the out-of-plane deviation of the skin of the panels with respect to the flat plane. The DIC measurement setup uses two stereo camera and additional lighting, and is shown in Figure 4.4.

The measured skin-side imperfections are reported in Figure 4.5, where the out-of-plane deviation is projected onto each panel as a contour plot, and the imperfection is aligned with the z-axis of the axis system reported in Figure 4.3. The measurements show a maximum out-of-plane imperfection of 0.65 and 0.56 mm in the outwards direction, and a maximum of 1.55 and 1.08 mm in the inwards direction, respectively for the two panels. It is possible to note a slightly V-curved shape in the transverse direction and a slight curvature in the longitudinal direction. The curvature in the transverse direction is most likely caused by internal stresses due to the potting curing process and by the mismatch in stiffness of the potting material and composite laminates.

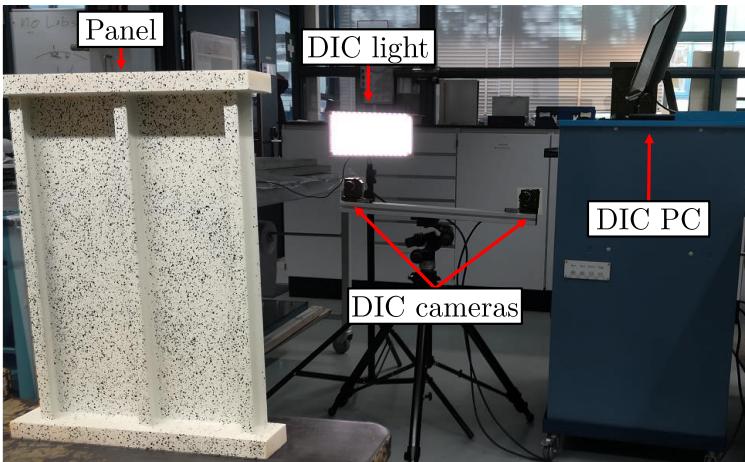


Figure 4.4: DIC measurement setup.

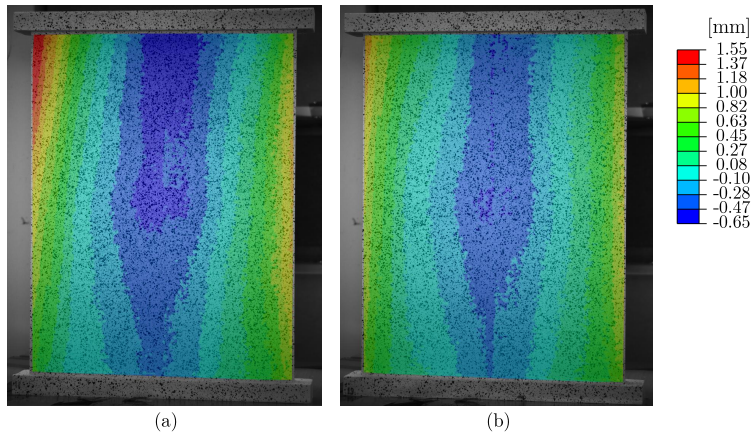


Figure 4.5: Out-of-plane geometrical imperfection of skin-side: (a) panel 1; (b) panel 2.

4.4 FINITE ELEMENT ANALYSIS

The buckling behaviour and skin-stringer separation of the two thermoplastic panels is studied, using Abaqus 2019 [34]. The general mesh size is determined by a mesh size sensitivity study. The study starts with linear buckling eigenvalue analysis for a mesh size ranging from 1.25 mm to 10 mm. This was followed by dynamic implicit analysis for a mesh size of 1.25 mm and 2.5 mm, to investigate the buckling and skin-stringer separation behaviour. A mesh size of 2.5 mm is chosen, as it shows converged results while being computational efficient. The laminated sections consist of continuum shell elements (SC8R). It is chosen to use solid brick elements with incompatible modes (C3D8I) for the filler, which has improved bending behaviour in combination with wedge elements (C3D6). The solid brick elements (C3D8R) are chosen for the potting material for computational efficiency as this element utilises reduced integration.

The modelling approach makes use of shared nodes to connect the different sections, as shown in the stringer cross-section in Figure 4.6. Shared nodes instead of ties shows better computational efficiency and more consistent mesh convergence. The interface between the filler and the skin of the middle stringer is partially bonded by a contact pair definition with VCCT. This area, which is the length of the stringer between the potting, is 445.3 mm long and 9.7 mm wide and has an initial damage of approximately 70 mm in the middle. It is assumed that the pre-crack is present only between the filler and the skin, and that it also only grows in this interface. The possible crack growth into the filler is neglected to lower the complexity of the model. This assumption is based on failure behaviour seen during internal tests by GKN Fokker and three-point bending tests by Baran et al. [55]. It is chosen to use VCCT as it shows good results for a relatively course mesh [26, 35, 56], needed for large structures as in this work, which was also shown by Bertolini et al [14] in a direct comparison between VCCT and CZM. Furthermore, VCCT requires a pre-crack, and this requirement is automatically fulfilled due to the initial damage in the skin-stringer interface.

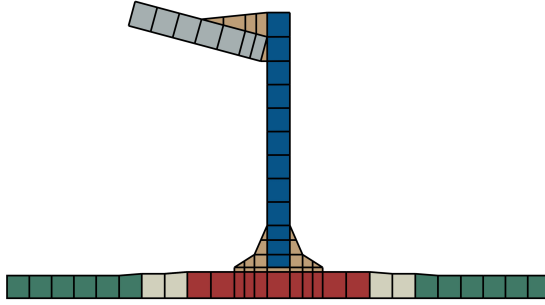


Figure 4.6: FE mesh of the stringer cross-section.

The VCCT definition uses the Benzeggagh Kenane (BK) criterion [34, 59] for mixed-mode interface behaviour. The fracture criterion is shown in Equation 4.1, which allows a node at the crack-tip to fail when it is equal to or higher than 1. The fracture criteria consists of the critical equivalent strain energy release rate G_{equivC} , defined in Equation 4.2, divided by the equivalent strain energy release rate G_{equiv} , given in Equation 4.3. The equivalent strain energy release rate is calculated for each node. The parameters in the equation consist of the strain energy release rates for the three different modes, G_I , G_{II} and G_{III} , which are based on nodal displacements and forces.

The critical equivalent strain energy release rate G_{equivC} is calculated using the interface properties G_{IC} , G_{IIC} and G_{IIIC} , which are reported in Table 4.5. The mode I and II fracture toughness, G_{IC} and G_{IIC} , are based on tests performed by GKN Fokker. The mode III fracture toughness, G_{IIIC} , is assumed to be equal to the mode II fracture toughness. The BK parameter, η , is based on data from literature of a similar material, AS4/PEEK [37].

$$f = \frac{G_{equiv}}{G_{equivC}} \geq 1.0 \quad (4.1)$$

$$G_{equivC} = G_{IC} + (G_{IIC} - G_{IC}) \left(\frac{G_{II} + G_{III}}{G_I + G_{II} + G_{III}} \right)^\eta \quad (4.2)$$

$$G_{equiv} = G_I + G_{II} + G_{III} \quad (4.3)$$

The VCCT definition uses a default fracture tolerance of 0.2 and an unstable crack growth tolerance of 10. This unstable crack growth option is included to improve convergence and computational efficiency when unstable crack growth occurs. The value used for the unstable crack growth tolerance is chosen to limit the amount of nodes released at the same time, and to retain multiple data-points during unstable crack growth. Contact stabilisation is used to stabilise both loss of contact and separation, with a stabilisation factor of $1e-4$, which shows improved convergence and computational efficiency. The contact definition utilises node-to-surface contact discretisation, with the stringer assigned as the master surface and the skin as the slave surface.

The analysis includes first ply failure criteria to determine if material failure could occur in the composite laminates before skin-stringer separation. The following criteria

Table 4.5: Fracture properties of skin-stringer interface.

G_{IC} [kJ/m ²]	G_{IIC} [kJ/m ²]	G_{IIIc} [kJ/m ²]	η [-]
1.41	1.9	1.9	2.3

Table 4.6: Strength properties of AS4D/PEKK-FC carbon UD ply.

XT [MPa]	XC [MPa]	YT [MPa]	YC [MPa]	SL [MPa]
2559	1575	83.1	284	99

4

are used: Hashin, Tsai-Hill, Tsai-Wu and Max-Stress. The strength properties for input in these criteria are reported in Table 4.6, and are based on test results by GKN Fokker.

The geometrical imperfections are included in the FE model, as buckling behaviour of thin-walled structures is known to be sensitive to imperfections. Any residual stresses, for example from the manufacturing process, are neglected. The geometrical imperfections are applied to the nominal mesh by means of a FE linear analysis. The out-of-plane coordinates of the DIC imperfection are translated into boundary conditions for the linear analysis using python. This linear analysis outputs a nodefile that only includes the deformation field. The nodefile can be used to apply the imperfection in the non-linear analysis, without transferring the stress state of the previous linear analysis. The resulting out-of-plane displacement fields of the linear analysis for both panels, which are the geometrical imperfection used for further analysis, are shown in Figure 4.7.

Three types of analysis are performed to determine the structural behaviour of the thermoplastic stiffened panels. Firstly, a linear analysis is used to determine the linear stiffness of the panels, which results in a stiffness of 132 kN/mm. Secondly, a linear buckling eigenvalue analysis is executed to determine the initial buckling shape. The buckling shape is shown in Figure 4.8, and consists of three half-waves per bay with the out-of-plane direction of the half-waves anti-symmetric with respect to the middle stringer. The linear buckling load is 100 kN. Thirdly, a dynamic implicit analysis is used to determine the non-linear post-buckling behaviour. The longitudinal compression load-case is applied by displacement boundary conditions. On each end of the panel a reference point is placed. This reference point is connected to each end of the panel (including potting material) by a rigid-body-tie definition. This allows to apply clamped boundary conditions on one end and longitudinal displacement on the other end on only two nodes.

The dynamic implicit analysis includes the contact definition with VCCT for skin-stringer separation with the initial damage of 70 mm, representing BVID. The dynamic implicit step utilises the quasi-static application, which uses the backward Euler operator. The analysis step time is 1 s, with an initial and maximum time increment size of 0.01 s and a minimum of 1e-08 s. The applied displacement is 3 mm, which results in a displacement rate of 3 mm/s. The maximum number of attempts for an increment in the time incrementation controls is increased to 40, to help convergence once separation starts to occur.

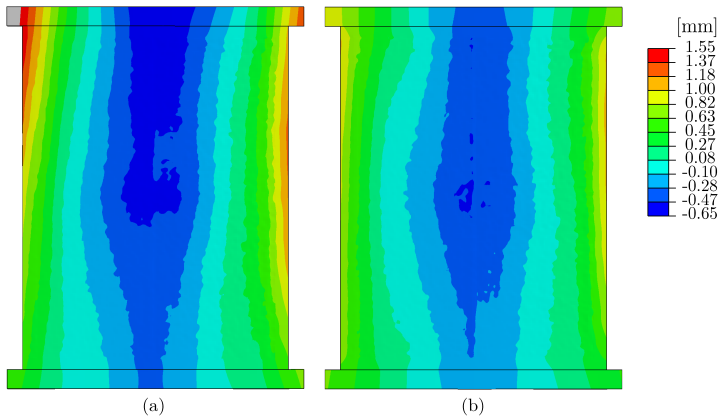


Figure 4.7: FE out-of-plane geometrical imperfection of skin-side: (a) panel 1; (b) panel 2.

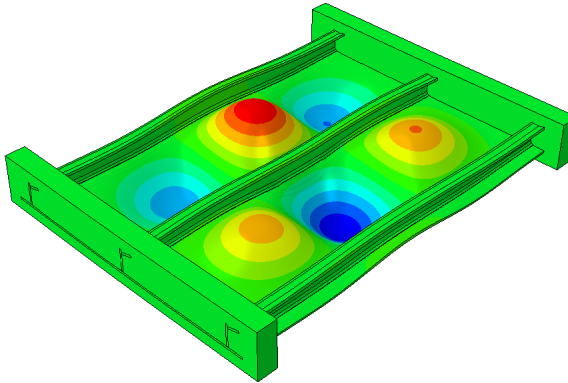


Figure 4.8: FE eigenvalue buckling shape.

4.5 TEST SETUP

The thermoplastic stiffened panels are tested to study the buckling, the post-buckling behaviour, the skin-stringer separation and the final failure mode using a MTS test machine capable of 3500 kN under compression. Furthermore, the experimental test results and the observed phenomena are used to validate the numerical analysis.

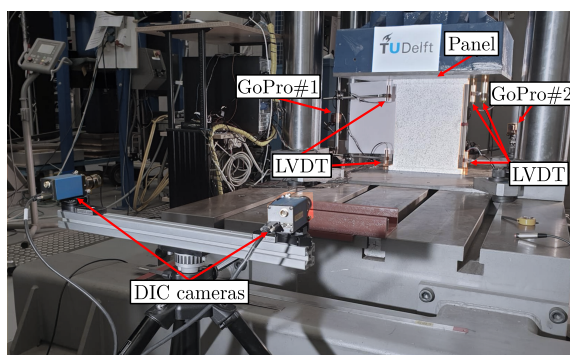
The experimental test setup is shown from the skin-side and stringer-side of the panel in Figure 4.9. The panel is placed between the base and the compression plate of the test machine, after which a low preload of 0.5 kN is applied to keep the panel in place. The tests are performed at a loading rate of 0.1 mm/min until final failure of the panel. The loading automatically stops when the drop in force is measured.

The force and displacement of the compression plate are measured by the load cell and the transducer of the testing machine. Five Linear Variable Differential Transducers (LVDT) are used to measure longitudinal displacement. Two LVDTs are placed on the base

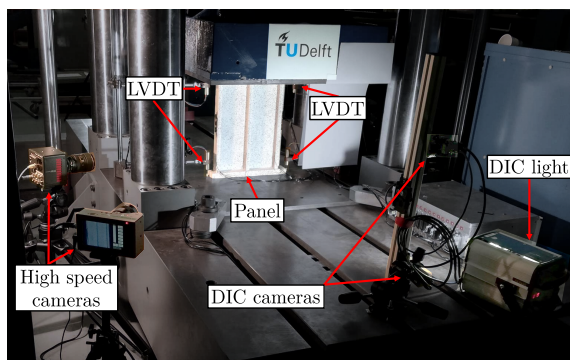
plate and three LVDTs are placed on the compression plate. The different locations are chosen to determine if a loading imperfection is occurring. The measured displacements are recorded every 3 s and combined with the force measured by the load cell of the test machine.

A total of 7 strain gauges are attached to each panel to measure strains. A strain gauge is attached to each web under the cap towards the bottom of the panel, while the other strain gauges are attached back-to-back on the free edges of the skin. The locations of the strain gauges are shown in Figure 4.2 and Figure 4.3, with the strain gauges on the web and on the skin named W# and S#, respectively. The locations are chosen according to the results of the numerical predictions, such that the strain gradient is low at each location. The strain gauges on each web show if each stringer is equally loaded in pre-buckling, and how the load distribution changes in post-buckling due to the growth of the skin-stringer separation. The strain gauges on the skin are used to determine loading imperfections due to bending.

4



(a)



(b)

Figure 4.9: Test setup: (a) skin-side; (b) stringer-side.

Two DIC systems are used to capture the displacement field of both the skin and stringer side of the panels. Each DIC system consists of two stereo cameras and VIC 3D 8

software for post-processing. Each camera is set up to take a picture every 3 s, resulting in approximately 500 pictures per camera. The force measured by the load cell of the test machine is linked to each DIC system to record the corresponding load for each picture. The DIC measurement is used to determine the out-of-plane displacement of the post-buckling shape, and the longitudinal shortening of the panels through the in-plane displacement of the potting.

Three GoPro cameras are used to monitor the test. Two cameras are directed at the initial damage to capture the crack growth behaviour on both sides of the stringer. The third camera is positioned further away to capture the test as a whole.

Two high-speed cameras are used to capture the final failure of the panels. Both cameras are focused on the initial damage at the cap side of the stringer. This side of the stringer is chosen as the numerical predictions show crack growth on this side only. One camera captures a side view of the stringer at 3000 fps, while the second camera is positioned further away to capture the crack growth but also the complete panel at 10000 fps.

4.6 TEST RESULTS AND COMPARISON TO NUMERICAL PREDICTION

This section describes the results of the tests, and compares them to the prediction from the numerical analysis.

4.6.1 LOAD VERSUS DISPLACEMENT CURVES

The load measured from the load cell of the test machine and the longitudinal displacement measured by DIC is used for obtaining the load-displacement curves. The longitudinal displacement by DIC is determined by the difference in displacement from the top and bottom potting. The curves are shown together with the prediction from the numerical analysis in Figure 4.10 for panel 1 and 2.

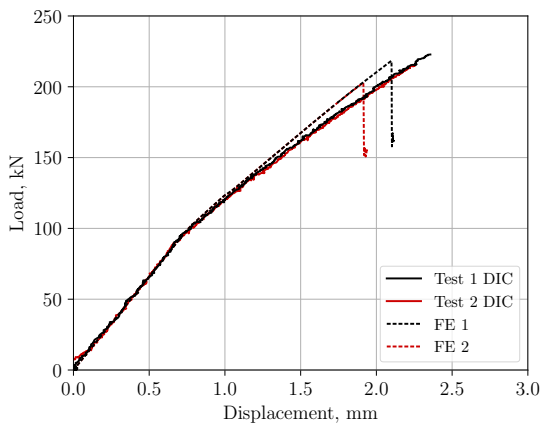


Figure 4.10: Load-displacement curves from tests and numerical predictions.

The panels show slight settling behaviour till a load of approximately 20 kN, after which a linear stiffness of 132 kN/mm is measured until buckling occurs at a load of approximately

94 kN for both panels. In the post-buckling field the stiffness is reduced, and continues to be reduced due to a buckling shape change and the growth of the skin-stringer separation. At a load of approximately 145 kN and 187 kN slight drops in stiffness occur for panel 1, while panel 2 shows only one reduction of stiffness at a load of approximately 138 kN. These stiffness reductions are caused by crack growth events, which could also be heard during the test. The panels fail due to skin-stringer separation at a load of 223.0 kN and 215.9 kN for panel 1 and 2, respectively. The difference in load for both the crack growth events and the final failure between the two panels is most likely caused by the difference in the initial damage shape and size and in the geometrical imperfections.

The numerical prediction shows a linear stiffness of 132 kN/mm, followed by buckling at approximately 99 kN. The linear stiffness is predicted accurately and there is a 5.3 % over-prediction in buckling load. The loss of stiffness due to crack growth in the post-buckling field can also be seen in the numerical prediction, but the stiffness is less affected in comparison to the test results and is slightly overestimated. The final failure load is predicted to be 218.3 kN and 202.8 kN for panel 1 and 2, respectively, with a difference of 2.1 % and 6.0 % compared to the tests. The maximum loads measured during the tests and the loads estimated by the analyses are reported in Table 4.7.

Table 4.7: Maximum loads from tests and numerical predictions.

	Test [kN]	FE [kN]	Difference [%]
Panel 1	223.0	218.3	-2.1
Panel 2	215.9	202.8	-6.0

4.6.2 LOAD VERSUS STRAIN CURVES

The strains measured by the strain gauges on the webs of panel 1 are shown in Figure 4.11(a). It can be seen that initially the pre-buckling strains in the outside webs are slightly higher compared to the middle web, indicating that there is a small loading imperfection. Then, all three webs show the same stiffness until buckling. In the post-buckling field the strains show a decrease in stiffness. At 145 kN and 187 kN small load drops are seen indicating crack growth events. The strains of the webs of panel 2 are shown in Figure 4.11(b). It can be seen that there is more settling compared to panel 1, most likely due to a slightly larger loading imperfection, and there is one load drop indicating a crack growth event at 138 kN.

The numerical predictions capture the load-strain behaviour in the webs well. In the pre-buckling field there is a small difference in the initial settling, as the loading imperfections are not taken into account in the numerical predictions. In post-buckling the strains are slightly over predicted.

The strains in the skin of panel 1 are shown in Figure 4.12(a) and Figure 4.12(b) for location S1 and S2, respectively, with notation IML and OML for inner and outer mould line. At location S1 the measured strains show a small difference between inner and outer mould line indicating a small bending component. At location S2 the influence of bending is more clear, with a larger difference between IML and OML in the post-buckling field. The measured strains at location S1 are considerably higher compared to location S2 in

post-buckling. This difference is most likely caused by the non-symmetric stringer, with S1 being located on the opposite side of the cap and S2 being located underneath the cap.

The strains of the skin of panel 2 are shown in Figure 4.13(a) and Figure 4.13(b) for location S1 and S2 respectively. In pre-buckling, location S2 shows a minor bending component, which is not seen for panel 1. This is most likely caused by a small loading imperfection. For both location S1 and S2 the measured strains of panel 2 show more bending compared to panel 1.

The numerical analysis accurately predicts the strain in pre-buckling for both location S1 and S2. A small difference is seen for panel 2 location S2, due to bending in the measured strains in the pre-buckling field. In post-buckling the strains are under predicted at location S1, while the strains at location S2 are accurately predicted for both panel 1 and 2 in post-buckling.

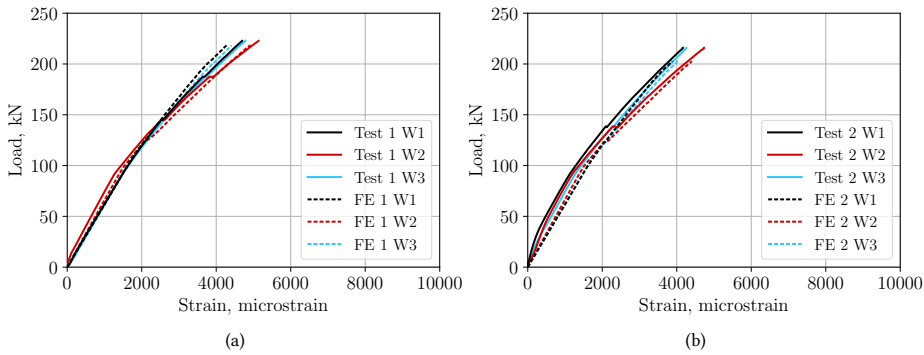


Figure 4.11: Experimental and numerically predicted compressive strains in stringer webs: (a) panel 1; (b) panel 2.

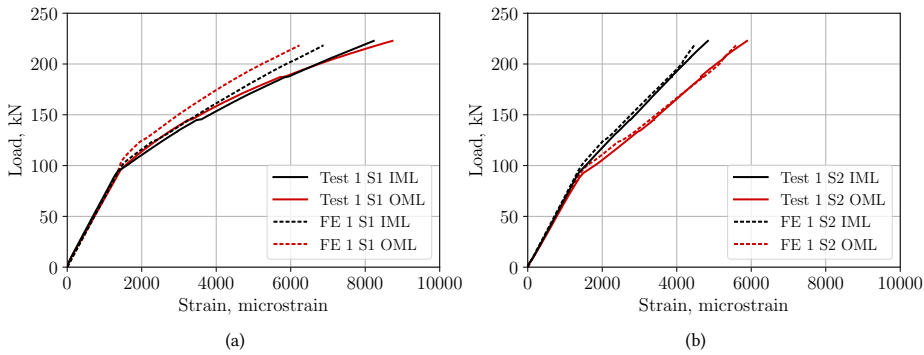


Figure 4.12: Experimental and numerically predicted compressive strains of panel 1: (a) S1; (b) S2.

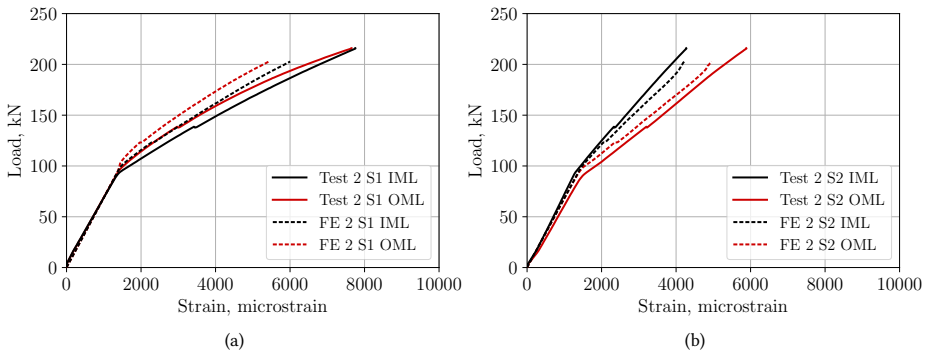


Figure 4.13: Experimental and numerically predicted compressive strains of panel 2: (a) S1; (b) S2.

4.6.3 OUT-OF-PLANE DISPLACEMENT

The out-of-plane displacements of the two panels captured by the DIC system are reported in Figure 4.14 by contour plots at four load levels, to show the evolution of the deformation in the post-buckling field. For each contour plot the maximum and minimum out-of-plane displacement are reported. A positive sign is for displacement in inwards direction towards the stringer, and a negative sign is for outwards direction away from the stringer, in line with the axis system reported in Figure 4.3. The contour plots for both tests are compared with the results of the numerical analysis.

The test of panel 1 shows an initial three half wave buckling mode, antisymmetric with respect to the middle stringer. At higher loads the buckling shape changes slightly, with a fourth half wave appearing at the top of the right bay. It can be noted that there is a higher inward out-of-plane displacement, in the direction of the stringers, compared to the outward displacement. Initially after buckling it is seen that the magnitude of the out-of-plane displacement is approximately equal in both bays. At higher loads the fourth half-wave becomes more prominent and the magnitude of the displacement becomes higher in the left bay in both inwards and outwards direction compared to the right bay. The half-waves in the left bay are also longer compared to the right bay. This difference becomes more prominent when the fourth half-wave appears in the right bay, and the difference continues to increase until final failure.

The test of panel 2 shows the same three half wave buckling shape as panel 1. In comparison to panel 1, the buckling shape changes with a fourth half-wave at the top of the right bay at a higher load, and the fourth half-wave is smaller in magnitude. The out-of-plane displacement at 116 kN of panel 2 is higher in inwards direction and lower in outwards direction compared to panel 1. This difference might be caused by differences in the geometrical imperfections or loading imperfections, and becomes less at higher loads when the out-of-plane displacements of panel 1 and 2 converge.

The three half-wave buckling shape is accurately predicted, with a great level of similarity in terms of half-wave position and length. The buckling shape change with the fourth half-wave at the top of the right bay is also predicted, but it happens at a higher load compared to what is seen in both tests.

The magnitude of the out-of-plane displacements are smaller for inwards direction,

while the outwards displacements are initially larger. The outwards out-of-plane displacements at the maximum load is accurately predicted for both panels, indicating that the amount of crack opening due to the outwards displacements might be the dominating factor for final failure.

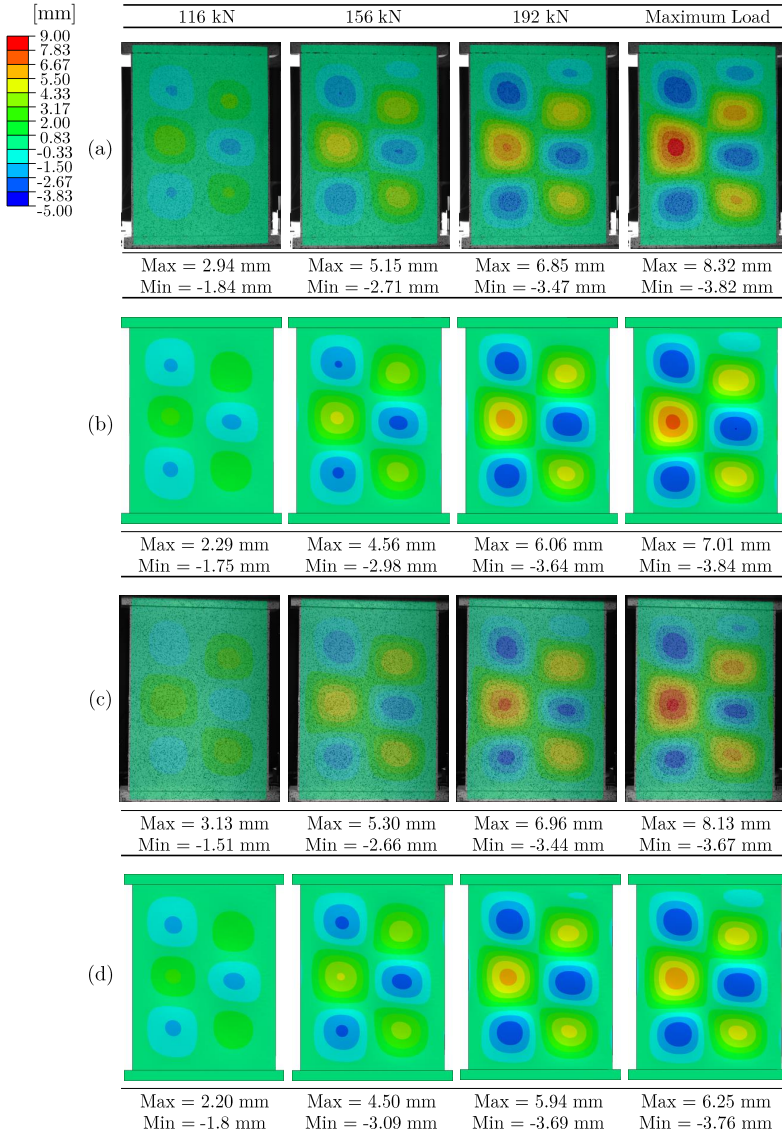


Figure 4.14: Out-of-plane displacement: (a) panel 1 test; (b) panel 1 FE; (c) panel 2 test; (d) panel 2 FE.

4.6.4 SKIN-STRINGER SEPARATION

The skin-stringer separation is analysed in more detail with the help of camera footage from the test and the numerical prediction.

On the camera footage of panel 1 a very small tick is heard at 98 kN, while a slightly louder tick can be heard at 120 kN. At 98 kN no crack opening can be seen and the sound seems to origin from the foil for the initial damage being pulled from the skin and chipping paint. When the tick at 120 kN is heard, crack opening is present and it is therefore considered the start of the crack growth. On the camera footage of panel 2 a small tick is heard at 119 kN which is considered the start of the crack growth. During the tests of both panels loud ticks can be heard in post-buckling where the initial damage grows initially unstable and then continues with stable crack growth.

As panel 1 and panel 2 show very similar behaviour, only camera footage of panel 1 is here reported. At 156 kN, approximately between buckling and final failure, crack opening can be well distinguished, as shown in Figure 4.15. The crack has opened and grown, with more crack growth in downwards direction compared to upwards direction. The cap-side of panel 1 is shown Figure 4.15(c). The opposite side of panel 1, corresponding to the side of the stringer without cap, is shown in Figure 4.16, where no crack opening can be seen. The one-sided crack opening is due to the buckling shape, where the outwards half-wave on the cap-side opens the crack, while the inwards half-wave on the opposite side of the cap tends to close it.

The numerical analysis accurately predicts the combination of stable crack growth and crack growth events. The corresponding views are shown in Figure 4.15(a-b) and Figure 4.16(a-b) for the cap and the opposite side, respectively, for a comparison with the camera footage.

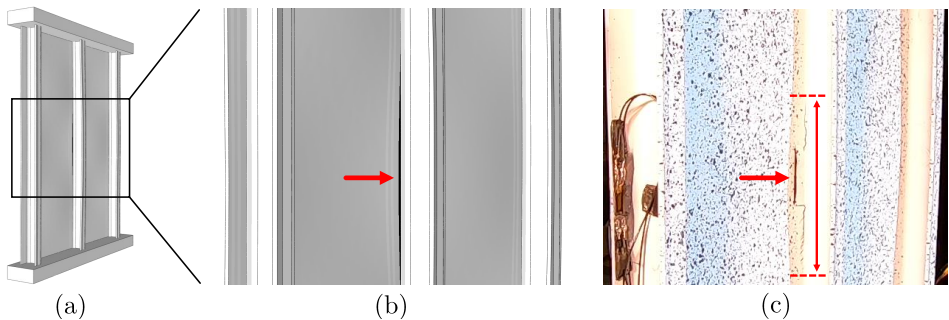


Figure 4.15: Crack opening seen from left side of panel 1 at 156 kN: (a) full view of panel; (b) close-up FE; (c) close-up camera footage with visual separation length marked in red.

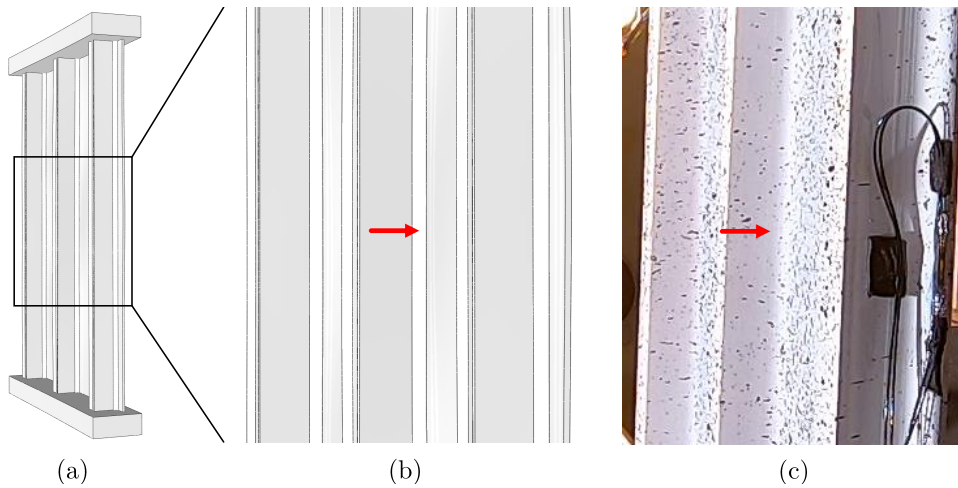


Figure 4.16: Closed crack seen from right side of panel 1 at 156 kN: (a) full view of panel; (b) close-up FE; (c) close-up camera footage.

4.6.5 FRACTURE SURFACE

To further investigate the skin-stringer separation, the fracture surface is analysed. It is shown over a length of 196.5 mm, as highlighted in Figure 4.17(a), which corresponds to the area that is separated before the final failure. The fracture surface of panel 1 is shown in Figure 4.17(b), where the foil inserted in the joint for the initial damage can be noted. The grey marks close to the foil are considered to be caused by the extension process of the initial damage, as the distance between the markings match the initial damage length. Larger grey marks can be seen further away from the foil, with a slight elliptical shape. The shape of these marks is most likely caused by the one-sided crack growth in the post-buckling field.

On the left side there is a delamination of plies from the skin, with only little short-fibre filler material still attached to the skin. On the right side no delamination is seen, and there is more remaining filler material attached to the skin. The remaining filler material is on the opposite side of the stringer, with the cap-side of the stringer showing no remaining filler material. This can be caused by the one-sided crack growth before final failure, followed by the unstable crack growth during final failure where separation also occurs between the web and the filler material.

The fracture surface of panel 2 is shown in Figure 4.17(e). The fracture surface is very similar to panel 1, but it shows less grey marks. This might be due to the single unstable crack growth event in post-buckling compared to panel 1. Also, more filler material remains attached to the skin, and delaminations can be seen on both sides of the foil.

The skin-stringer interface of the numerical analysis for panel 1 is shown for the initial damage and at the load of 156 kN in Figure 4.17(c) and Figure 4.17(d), respectively, where red indicates intact interface, and blue indicates separated interface. The numerical prediction at 156 kN shows a quasi-elliptical crack front shape, with a narrow horizontal line of intact interface.

The skin-stringer interface of the numerical analysis for panel 2 for the initial damage and at the load of 156 kN are shown in Figure 4.17(f) and Figure 4.17(g), respectively. The initial damage is similar to panel 1, but is slightly longer. The interface at 156 kN shows slightly more crack growth compared to panel 1, which might have led to the lower final failure load of panel 2.

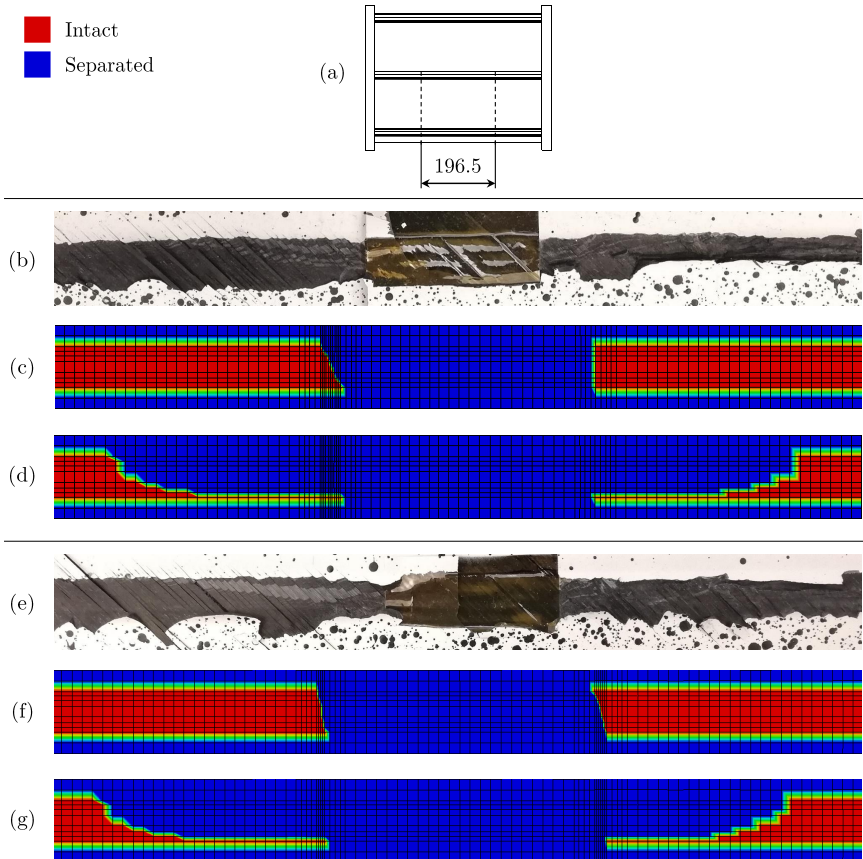


Figure 4.17: Top view skin-stringer interface: (a) interface area of interest; (b) test panel 1 fracture surface; (c) FE panel 1 initial damage; (d) FE panel 1 at 156 kN; (e) test panel 2 fracture surface; (f) FE panel 2 initial damage; (g) FE panel 2 at 156 kN.

4.6.6 MODE-MIXITY

The mode-mixity of the skin-stringer separation obtained from the numerical analysis is investigated, focusing on the results of panel 1 for conciseness as panel 2 shows similar results. The mode-mixity expresses the ratio between peeling (mode I) and shear (mode II/III) loading on the interface. This ratio is of importance as it indicates how the interface is loaded due to buckling, and which type of loading is critical leading to interface failure.

The mode-mixity is determined by using the energy release rates for mode I, II and

III as shown in Equation 4.4, resulting in a value of 0 for pure mode I and a value of 1 for pure mode II/III. In case of an intact interface, a value of -1 is assigned. The interfaces are analysed over a length of 463 mm, as reported in Figure 4.18(a). The mode-mixity of the fracture surface at the start of final failure is shown in Figure 4.18(b). The one-sided crack growth before failure is mode I dominated, with final failure being initiated by a narrow line of mode II/III fracture. The fracture surface after the final failure of the panel is shown in Figure 4.18(c). The crack growth towards the left is mode I dominated while the crack growth towards the right is mode II/III dominated. The majority of the fracture surface is either dominated by mode I or mode II/III, with only small areas of mixed-mode loading.

$$\text{Mode - Mixity} = \frac{G_{II} + G_{III}}{G_I + G_{II} + G_{III}} \quad (4.4)$$

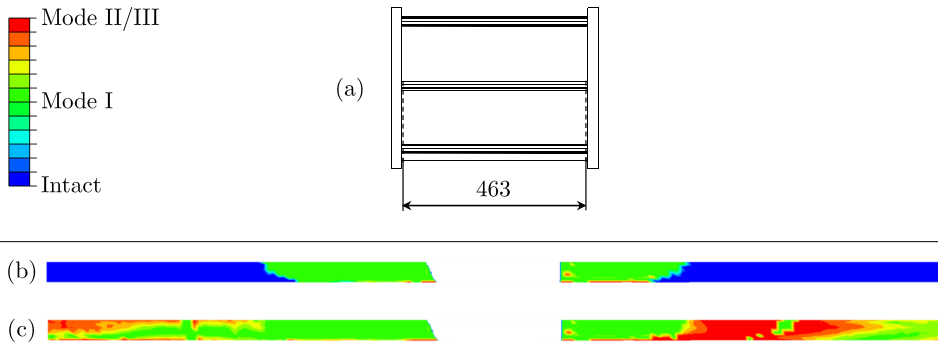


Figure 4.18: Panel 1 mode-mixity: (a) interface area of interest; (b) mode-mixity at start of final failure; (c) mode-mixity after final failure.

4.6.7 FIRST PLY FAILURE

Four first ply failure criteria are included in the numerical analysis to determine if material failure occurs before skin-stringer separation. The values of the most critical ply for each criterion at the maximum load are reported in Table 4.8 for both panels. It is possible to see that none of the criteria show first ply failure before final failure, with the Tsai-Wu criterion reporting the highest value for both panels. The most critical ply according to the Tsai-Wu criterion is the bottom zero ply in the skin, for which the contour plots of both panels are shown in Figure 4.19. It can be noted that the most critical locations are underneath the outer stringers, approximately coinciding with the longitudinal location of outwards half-waves of each corresponding bay.

Table 4.8: Numerical first ply failure criteria values at maximum load.

	Hashin Fibre Compression	Max Stress	Tsai-Hill	Tsai-Wu
Panel 1	0.48	0.72	0.76	0.91
Panel 2	0.37	0.64	0.67	0.82

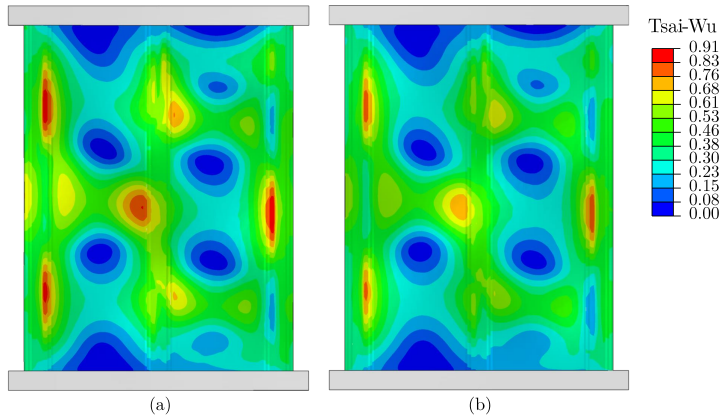


Figure 4.19: Tsai-Wu failure criterion of the skin bottom zero ply from the numerical prediction at maximum load: (a) panel 1; (b) panel 2.

4.6.8 FINAL FAILURE MODE

The final failure mode is captured by two high speed cameras. The area that is recorded by high speed camera 1 is shown on the FE model in Figure 4.20(a). A frame of the 3000 fps high speed footage of panel 1 is shown in Figure 4.20(b). It highlights the behaviour during separation of the middle stringer. The crack in the butt-joint grows in downwards direction and a tunnel forms between two outwards buckling half-waves. Due to the separation of the stringer from the skin, the cap and the web of the stringer also start to show failure, and consequently load carrying capabilities are lost. The numerical prediction of the final failure of the panel is shown in Figure 4.20(c). The analysis also reveals crack growth in downwards direction, with a tunnel between two outwards buckling half-waves, similarly to the failure behaviour seen in the tests.

The sequence of the final failure over the full length of panel 2 is captured by the second high speed camera at 10000 fps, as shown in Figure 4.21. Final failure starts with the crack opening (a). Then the crack grows between the web of the middle stringer and the skin (b), after which the separation between the web of the right stringer and the skin occurs (c). This is followed by the separation between cap and web of the middle stringer (d) and failure of the middle cap (e). Then, the web of the left stringer starts to separate from the skin simultaneously with the separation between cap and web of the right stringer (f). This sequence occurs within 2.1 ms, and shows that the skin-stringer separation is the critical failure mode leading to the final failure of the panel.

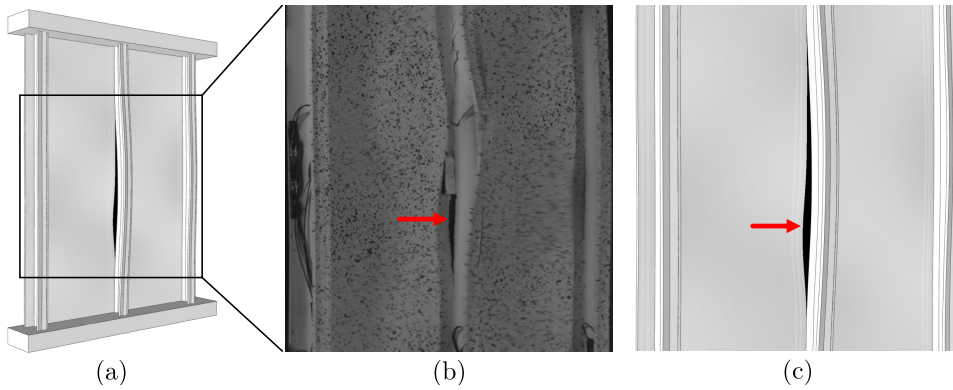


Figure 4.20: Crack opening of panel 1 during final failure: (a) full view of panel; (b) high speed camera; (c) close-up FE.

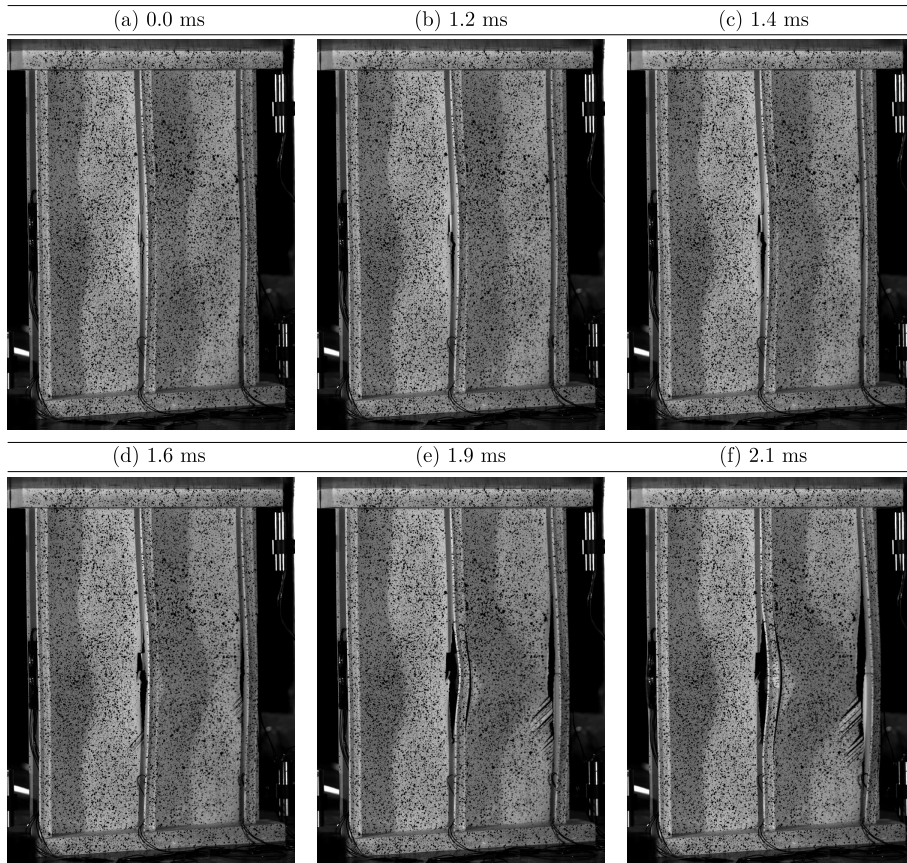


Figure 4.21: Sequence of final failure of panel 2 captured by high speed camera: (a) crack opening of middle stringer; (b) crack propagation of middle stringer; (c) separation of right stringer; (d) separation of middle cap; (e) failure of middle cap; (f) separation of left stringer and separation of right cap.

4.7 CONCLUSIONS

In this research two butt-joint thermoplastic composite stiffened panels with an initial damage in the skin-stringer interface are successfully analysed and tested. The growth of the initial damage occurs during post-buckling, but only leads to panel final failure at considerably higher loads. The skin-stringer separation is heavily influenced by the buckling shape, as the anti-symmetric buckling shape results in crack opening only on the cap-side of the stringer. The combination of stable and unstable crack growth before final failure can be accounted to both the butt-joint stringer design and the ductile behaviour of the thermoplastic composite material. This structural behaviour is considerably different compared to the more classical designs of the stiffened panels made of thermoset composites.

Numerical analyses are conducted using the commercial finite element software Abaqus. Skin-stringer separation is modelled by the use of the Virtual Crack Closure Technique. The structural behaviour is accurately predicted by the numerical analysis. Even if the post-buckling stiffness is slightly over-predicted after the crack growth events, the analysis has accurately predicted the buckling shape, the post-buckling behaviour, the skin stringer separation and the final failure load and sequence. This shows that the developed methodology is a reliable tool for the design of new thermoplastic aeronautical structures.

ACKNOWLEDGEMENT

The authors would like to thank Jaap Willem van Ingen and Ivo Lippers from Fokker/GKN Aerospace and Theodor Baciu from Delft University of Technology for their support during the testing campaign.

This research has partially received funding from the Clean Sky 2 Joint Undertaking (JU) under grant agreement No 945583, STUNNING. The JU receives support from the European Union's Horizon 2020 research and innovation programme and the Clean Sky 2 JU members other than the Union.

DISCLAIMER

The results, opinions, conclusions, etc. presented in this work are those of the authors only and do not necessarily represent the position of the JU; the JU is not responsible for any use made of the information contained herein.

5

BUCKLING AND FAILURE ASSESSMENT OF CURVED BUTT-JOINT STIFFENED THERMOPLASTIC COMPOSITE PANELS WITH ROLLER BOUNDARY CONDITIONS

5

Two curved thermoplastic composite multi-stringer panels with roller boundary conditions are analysed and tested to investigate the buckling and failure behaviour. The panels are made of AS4D/PEKK-FC thermoplastic composite, have five stringers with an angled cap on the side and are joined to the skin with the short-fibre reinforced butt-joint technique. The panels have a roller attached to each loading edge, approximating simply-supported boundary conditions to apply compression and bending. One panel has barely visible impact damage in one of the stringer butt-joints, and one panel is in pristine condition. Finite element analyses are performed to predict the structural behaviour, and different approximations of the roller boundary conditions are compared. The analyses include material damage initiation and evolution. The out-of-plane displacement of the panels is measured by digital image correlation, and failure is captured with high-speed cameras. The panels fail in a sudden manner when the cap separates from the web, followed by web failure and skin-stringer separation in the butt-joint. The numerical analysis predicts the overall structural behaviour but cannot capture well the sudden panel collapse due to material damage.

This chapter is directly based on a manuscript submitted to Elsevier.  Kevin van Dooren, Jan Waleson, Mark Chapman, Chiara Bisagni. Buckling and failure assessment of curved butt-joint stiffened thermoplastic composite panels with roller boundary conditions.

5.1 INTRODUCTION

One of the prominent goals of the aeronautical industry is to lower the environmental impact of flight by reducing fuel consumption, which also reduces costs. One of the ways is to reduce the structural weight, as the weight is directly related to the fuel consumption for flight. The reduction of weight can also lead to a higher passenger capacity per flight, leading to a lower number of flights needed.

This research targets the reduction of the aeronautical structural weight by the use of thermoplastic composites and by allowing these structures to buckle below the ultimate load. Aeronautical structures mostly consist of stiffened, thin-walled designs, which are known to buckle for compression and shear load cases. The current designs of primary structures do not allow for buckling below the ultimate load, as the post-buckling behaviour and failure modes in the post-buckling field are yet to be fully understood. It has been shown that these structures can sustain load deep into the post-buckling field [16, 38], indicating a considerable weight-saving potential.

The use of thermoplastic composites can also lead to a reduction of structural weight due to their structural properties and new manufacturing techniques. They are known to be more ductile and to have a higher toughness compared to their thermoset counterpart [17]. Thermoplastics allow for manufacturing techniques such as welding [9, 22] and co-consolidation [4], which lower the amount of fasteners needed and decrease both the weight and production time [6].

The common failure modes in post-buckling of aerospace stiffened structures consist of material failure [39, 42, 60] and skin-stringer separation [30, 32, 61], which are researched mostly on thermoset composites. The investigations on these failure modes are executed on a wide variety of specimen designs, consisting of single [29] and multi-stringer [41] panels with closed omega stiffeners [31], blade stiffeners [62] and I shaped stiffeners [63]. The tested specimens can be in both pristine and damaged state, where the damage can consist of, for example, impact damage [64] or a foil at the skin-stringer interface to approximate Barely Visible Impact Damage (BVID) [65].

The post-buckling behaviour of co-consolidated multi-stringer panels utilising the butt-joint technique [4, 16] is investigated in this research by analysis and experiments. Two multi-stringer panels are designed and manufactured by GKN Fokker [5]. The panels have a convex curvature and five stringers on the outside of the curvature. One panel is in pristine condition and one panel has initial damage at the skin-stringer interface that represents BVID. The panels are loaded in a mixed bending and compression load case, thanks to the aluminium rollers attached on both loading edges, to which compression is applied in a testing machine. These boundary conditions are uncommon in aeronautics, with literature limited to sandwich structures [66, 67]. Compression tests on aerospace structures usually have boundary conditions for the loading edges that are considered clamped, consisting of epoxy potted edges or similar [12, 40]. Roller boundary conditions are, however, more common in naval and civil applications, for example, for research on stiffened steel plates with single-stringer [68] and multi-stringer specimens [69, 70], but also aluminium plates with both open and closed-section stiffeners [71, 72] and even testing of corrugated board panels of packaging material [73]. The reason for using the roller boundary conditions in this research is two fold. Firstly, testing a panel with curvature in the longitudinal direction in compression with clamped-like conditions achieved by square

loading blocks can lead to tilting and rotation of these blocks due to the resulting moments, and it would not allow achieving structural behaviour in post-buckling representative of an aeronautical structure. Secondly, the rollers allow rotation and consequentially allow to achieve deformations, which would usually require a longer panel with clamped-like boundary conditions.

5.2 PANEL GEOMETRY

The curved multi-stringer panels are representative of the fuselage section of a business jet. The panels are manufactured and potted to the rollers by GKN Fokker and are received as shown in Figure 5.1. The rollers are made of aluminium, and the panels are attached to the rollers with epoxy potting. The panels have an approximate curvature and length of 6277 and 497 mm, respectively, and the total length including rollers is 585 mm, as reported in Figure 5.2(a). The rollers have a radius of 45 mm, and the loading edge and bending neutral axis of the panels coincide with the rollers' centre of curvature. The panels have five stringers, with a stringer spacing of 152.4 mm, which results in a total width of 650 mm, as reported in Figure 5.2(c).

The butt-joint technique is used to join the stringer to the skin. The stringer consists of a web and an angled side cap. The cap is 15 mm wide, angled at an angle of 105 degrees w.r.t. the web, which is 28 mm in height, as reported in Figure 5.2(b). The skin-web joint, which is called the butt-joint, and the web-cap joint consist of carbon Short Fibre Reinforced Plastic (SFRP) filler PolyEtherKetoneKetone (PEKK) extrusion profiles, of which the material properties are reported in Table 5.1. One of the panels has initial damage at the skin-stringer interface that represents a BVID. The location of this BVID is highlighted in red in Figure 5.2(a, b). The BVID is created by including a 40 mm foil at the skin-stringer interface during co-consolidation, after which the BVID is extended to 70 mm by applying out-of-plane displacement to the skin in a test machine [16, 74].

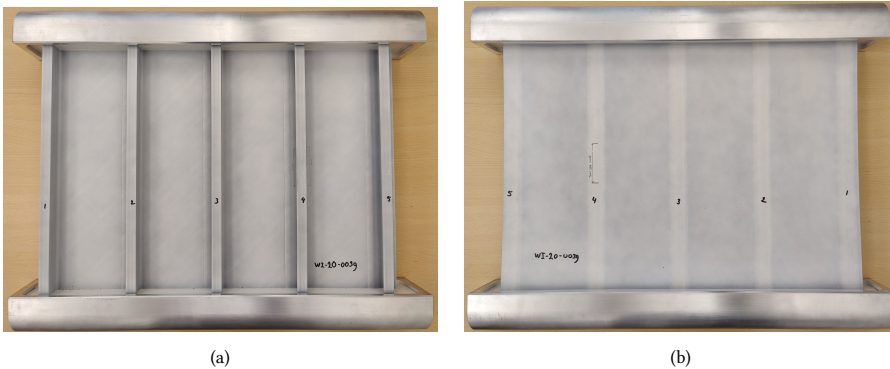


Figure 5.1: Panel: (a) stringer-side; (b) skin-side.

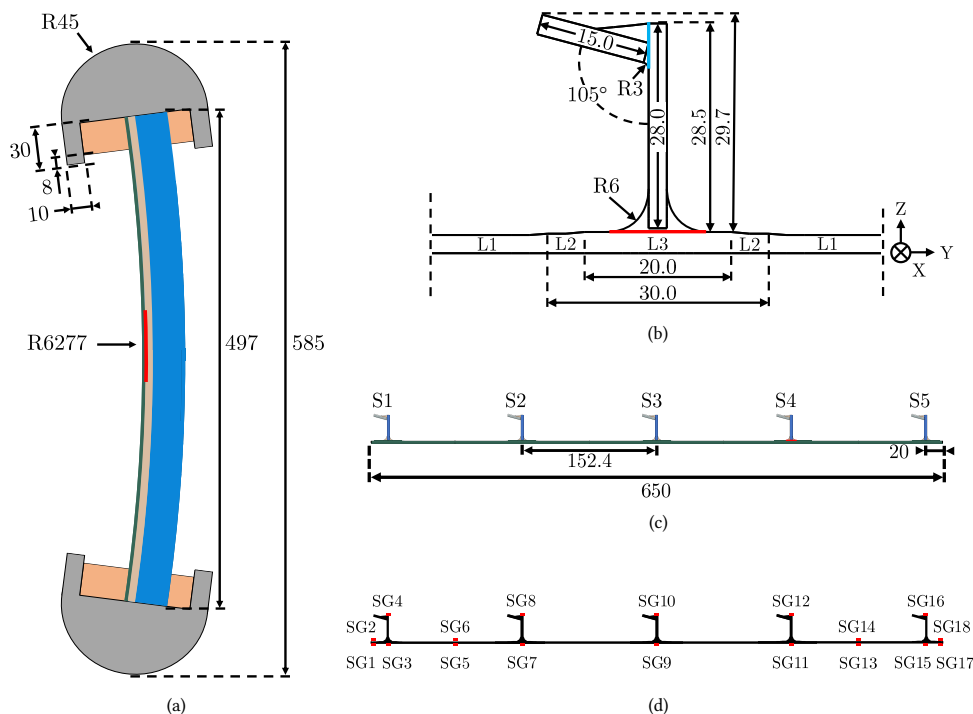


Figure 5.2: Panel geometry: (a) side-view illustration ; (b) stringer cross-section; (c) panel cross-section; (d) strain gauge positions.

Table 5.1: Properties of PEKK carbon SFRP filler [16].

E_{11} [MPa]	$E_{22} = E_{33}$ [MPa]	ν_{12} [-]	G_{12} [MPa]	ρ [kg/m ³]
13252	6579	0.42	2389	1560

The laminated parts are made of Fast Crystallizing PolyEtherKetoneKetone (PEKK-FC) carbon fibre (ASD4) UniDirectional (UD), of which the properties are reported in Table 5.2, and of additional glass fabric patches, of which the assumed properties are reported in Table 5.3. The layups of the laminates are reported in Table 5.4. The three different skin layups are due to the glass fabric patches applied underneath the stringer. The skin is manufactured by advanced fibre placement, while the web and cap laminates are pre-forms cut from a larger laminate. The web and cap are then assembled with the short fibre filler extrusion profiles and tooling blocks in an inner mould. The skin is placed on top of the mould, followed by the placement of the glass fibre patches at the stringer locations. The assembly is then vacuum-bagged and co-consolidated in an autoclave.

The panels are instrumented with 18 strain gauges at the positions reported in Figure 5.2(d), in the middle of the panel along the longitudinal direction. Strain gauges are attached back-to-back on the skin on the free edges, in the middle of the outer bays,

underneath each stringer and on the top of the vertical web. They can capture loading imperfections and allow to determine how the load is redistributed due to buckling, material damage and skin-stringer separation. White paint and black speckles are then applied on both sides of the panels as well as on the flat surfaces of the rollers.

Table 5.2: Ply properties of AS4D/PEKK-FC carbon UD ply [16].

E_{11} [MPa]	E_{22} [MPa]	ν_{12} [-]	G_{12} [MPa]	ρ [kg/m ³]	t_{ply} [mm]
126100	11200	0.3	5460	1560	0.138

Table 5.3: Ply properties of PEKK glass fabric [16].

E_{11} [MPa]	E_{22} [MPa]	ν_{12} [-]	G_{12} [MPa]	ρ [kg/m ³]	t_{ply} [mm]
25000	25000	0.3	3000	2200	0.1

Table 5.4: Layups and nominal thicknesses of laminate sections, with C and G superscript for carbon and glass plies, respectively.

Section	Thickness [mm]	Layup
Skin L1	2.484	[45/-45/0/45/90/-45/45/0/-45] ^C _s
Skin L2	2.684	[0 ₂] ^G [45/-45/0/45/90/-45/45/0/-45] ^C _s
Skin L3	2.884	[0 ₄] ^G [45/-45/0/45/90/-45/45/0/-45] ^C _s
Web	2.484	[45/90/-45/0/45/0/-45/0/45/-45] ^C _s
Cap	2.760	[45/90/-45/0/45/0/-45/0/0/90] ^C _s

5.3 NUMERICAL METHODOLOGY

The post-buckling behaviour of the curved multi-stringer panels is analysed with the commercial Finite Element (FE) software Abaqus 2021 [34].

The model utilizes continuum shell elements (SC8R) for the composite laminates, while solid brick and wedge elements (C3D8I, C3D6) are used for the short fibre filler material. The epoxy potting and aluminium rollers consist of solid brick elements with reduced integration (C3D8R) for better computational efficiency. The mesh of the stringer and skin cross-section is reported in Figure 5.3. Figure 5.3.

Dynamic implicit analysis is used in this study. The implicit step adopts a quasi-static application with a backward Euler operator. The total step time is 1 s, with the initial and maximum time increment size set to 0.01 s and the minimum to 1e-8 s. To improve convergence when separation starts, the maximum number of attempts for an increment is increased to 40 in the time incrementation controls.

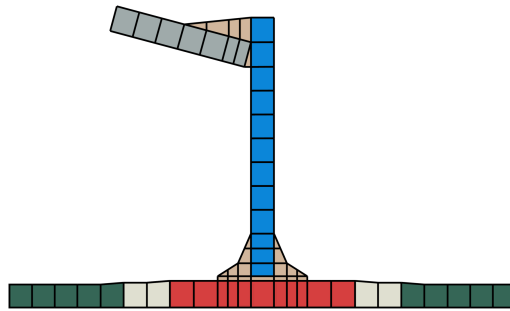


Figure 5.3: Mesh of the stringer cross-section.

5.3.1 COMPARISON OF BOUNDARY CONDITION APPROXIMATION

The roller boundary condition is approximated in three ways, as shown in Figure 5.4.

5

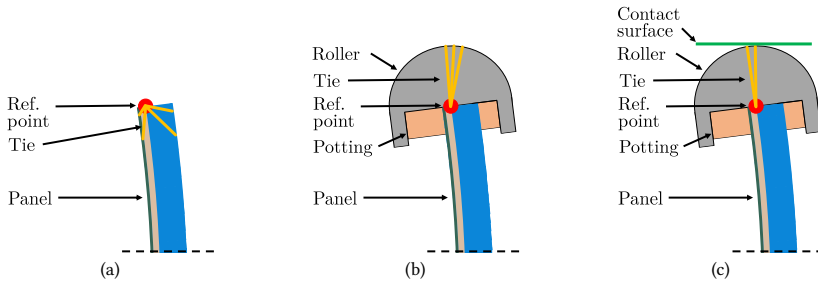


Figure 5.4: Comparison of the three approximations of the roller boundary conditions: (a) method 1, panel only; (b) method 2, roller; (c) method 3, roller with contact.

The first method utilises a reference point in the centre of the roller radius, as shown in Figure 5.4(a). This reference point is tied to the region of the panel that is inside the potting material, but no actual potting material is modelled. The reference point is constrained in all degrees of freedom except for rotation of the axis in the centre of the roller radius, and compression is applied in the longitudinal direction.

The second method models the potting and roller as shown in Figure 5.4(b). The panel, potting and roller are connected with shared nodes. There is a reference point in the centre of the roller radius, which is tied to a small region on the outside of the roller radius. This region is kept small to approximate a contact area. The reference point is free to rotate around the axis in the centre of the roller radius, compression is applied in the longitudinal direction, and the remaining degrees of freedom are constrained. The load is transferred from the reference point to the contact area through the rigid body ties. This method aims to approximate the application of compression through contact without the need for a contact definition and improves computational efficiency.

The third method adds contact between the roller and a contact surface to apply compression, as shown in Figure 5.4(c). This method still uses a reference point in the centre of the roller radius, which is tied to a region on the outside of the roller. This region is to the left of the initial contact point of the roller with the contact surface. It does

not come into contact with the contact surface, as the roller rotates in an anti-clockwise direction under compression. The reference point is constrained in all degrees of freedom except for rotation around the axis in the centre of the roller radius and the longitudinal direction. The purpose of the reference point is to keep the panel in place and shed the need for modelling friction, as it is assumed that there is no slipping of the rollers in the test.

The three models are compared using a mesh size of 2.5 mm for the laminated parts. The models with potting have a variable mesh size for the potting, ranging from 2.5 mm to 10 mm. The mesh size of 2.5 mm is where the potting is connected to the panel with shared nodes, and it increases in size in an outwards direction and is 10 mm in size at the connection with the roller. The roller uses a similar meshing technique, with the mesh size also ranging from 2.5 mm to 10 mm, for the model without contact. The model with contact uses a locally refined mesh at the contact surface of 1 mm.

All analyses use the same total displacement of 6 mm. The analysis of the three models run on the same CPU, and the wall clock time is 1589s, 3837s and 4752s, respectively. It should be noted, however, that the model with contact has an initial clearance between the contact surface and roller and displaces the roller 5.78 mm in total, which could lead to a slightly lower wall clock time.

The load-displacement graph of the three analyses is reported in Figure 5.5(a). The difference in load-displacement behaviour is minimal between the three different boundary condition methods. Method 1 shows an initial higher stiffness compared to methods 2 and 3, but converges with method 3 at higher displacements. Method 2 matches with method 3 initially but shows a slightly lower load at higher displacements. The roller load-rotation of the three analyses is reported in Figure 5.5(b). Only the top roller rotation is reported for conciseness, as the rotation of both rollers is indistinguishable in the analysis. All analyses show similar behaviour, with method 3 initially presenting a higher rotational stiffness and method 2 a lower overall stiffness. The two outer stringers, stringers 1 and 5, displace in the lateral direction during loading, as illustrated in Figure 5.6(a). The maximum lateral displacement of stringer 1 and minimum of stringer 5 are reported in Figure 5.6(b) and (c), respectively. Method 2 and 3 have very similar behaviour, while method 1 has a higher stiffness, especially for stringer 1. This is most likely caused by the rigid body tie in the potting region of method 1, instead of the physical modelling of the potting for method 2 and 3.

This comparison shows that method 1 is an efficient option for a similar load-displacement behaviour compared to method 3, which should be the method closest to reality. However, taking into account the differences in the deformation of the panel and the implementation of damage evolution in the following analyses, method 2 is considered a good compromise in terms of results and computational time. All analysis results in the following sections are obtained using method 2.

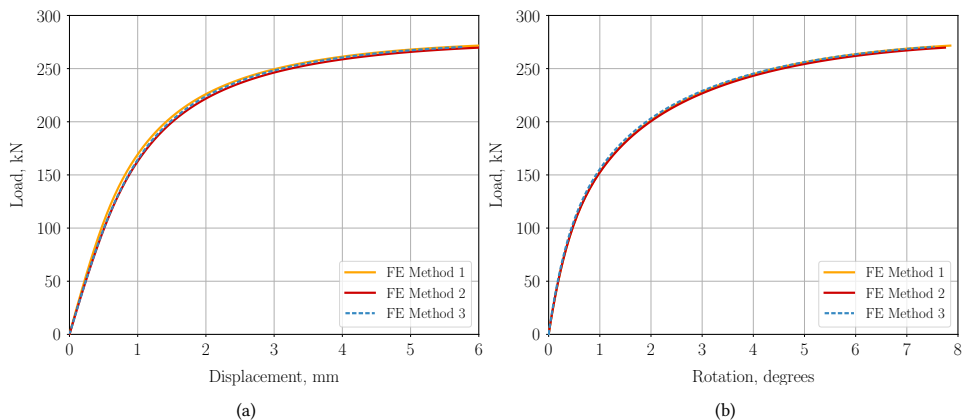


Figure 5.5: Load displacement (a) and rotation (b) curves of the analyses with different boundary conditions.

5

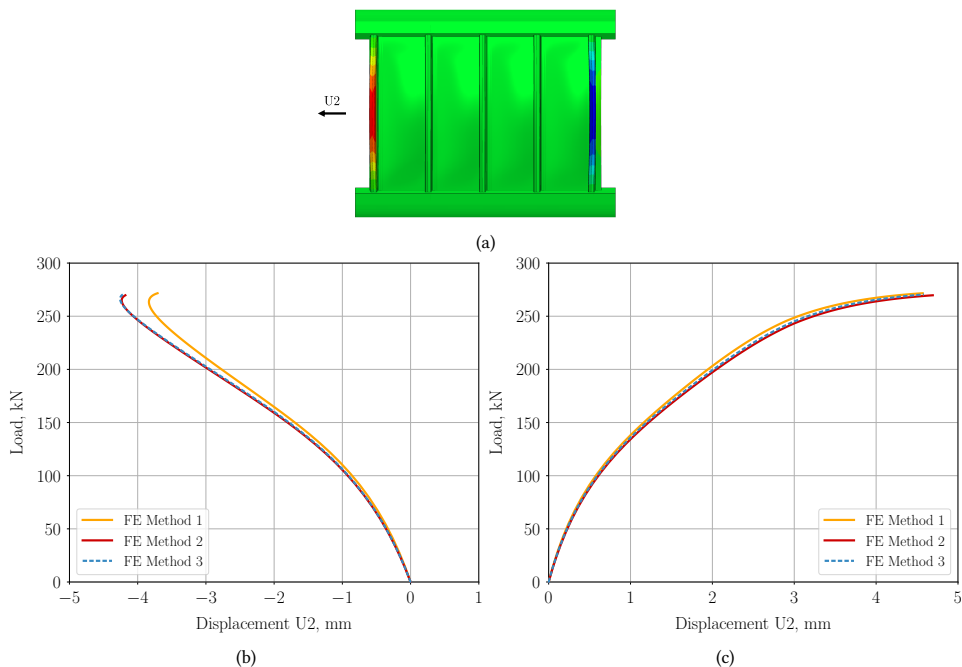


Figure 5.6: Load versus lateral displacement of the analyses with different boundary conditions: (a) contour plot FE method 2; (b) negative displacement; (c) positive displacement.

5.3.2 DAMAGE AND MESH SIZE SENSITIVITY

The Hashin criterion [75] is included in the analysis for initiation of material damage, followed by damage evolution [76]. The criteria for fibre tension, fibre compression, matrix tension, and matrix compression failure are reported in Equation 5.1, Equation 5.2, Equation 5.3 and Equation 5.4. The criteria are expressed as F , with superscript t and c for tension and compression, respectively, and subscript f and m for fibre and matrix, respectively. A value of 1 or higher means the criterion is met. The equations consist of the components $\hat{\sigma}_{11}$, $\hat{\sigma}_{22}$ and $\hat{\tau}_{12}$, for fibre direction, matrix direction and shear, from the effective stress tensor. The remaining terms are the material strengths, with X^T and X^C for fibre tension and compression strength, Y^T and Y^C for matrix tension and compression strength, and lastly, S^L for shear strength. The material strength properties for the criteria and the fracture properties are reported in Table 5.5.

Fiber tension ($\hat{\sigma}_{11} \geq 0$)

$$F_f^t = \left(\frac{\hat{\sigma}_{11}}{X^T} \right)^2 \quad (5.1)$$

Fiber compression ($\hat{\sigma}_{11} < 0$)

$$F_f^c = \left(\frac{\hat{\sigma}_{11}}{X^C} \right)^2 \quad (5.2)$$

Matrix tension ($\hat{\sigma}_{22} \geq 0$)

$$F_m^t = \left(\frac{\hat{\sigma}_{22}}{Y^T} \right)^2 + \left(\frac{\hat{\tau}_{12}}{S^L} \right)^2 \quad (5.3)$$

Matrix compression ($\hat{\sigma}_{22} < 0$)

$$F_m^c = \left(\frac{\hat{\sigma}_{22}}{Y^C} \right)^2 + \left(\frac{\hat{\tau}_{12}}{S^L} \right)^2 \quad (5.4)$$

Table 5.5: Strength and fracture properties of AS4D/PEKK-FC carbon UD ply [9, 16].

X^T [MPa]	X^C [MPa]	Y^T [MPa]	Y^C [MPa]	S^L [MPa]
2559	1575	83.1	284	99
G_{X^T} [kJ/m ²]	G_{X^C} [kJ/m ²]	G_{Icp} [kJ/m ²]	G_{IIcp} [kJ/m ²]	
125	61	1.12	2.35	

A mesh size sensitivity study is executed incorporating material damage and damage evolution, which are also compared to the results without damage evolution. The considered

mesh sizes are 0.75, 1.25 and 2.5 mm, with one element through the thickness of the composite laminates.

The load-displacement results are reported in Figure 5.7. The analyses with damage evolution start to show material softening at 2.56 mm of displacement for a mesh size of 2.50 mm, and at 2.50 mm of displacement for a mesh size of 1.25 and 0.75 mm, which can also be partially attributed to increment timing. At higher displacements, however, there is a sensitivity to mesh size, with a larger mesh size leading to more softening. The difference is more pronounced between the analysis with a mesh size of 1.25 and 2.5 mm, above an applied displacement of 4 mm. Consequently, the analysis results in the following sections are obtained using a mesh size of 1.25 mm.

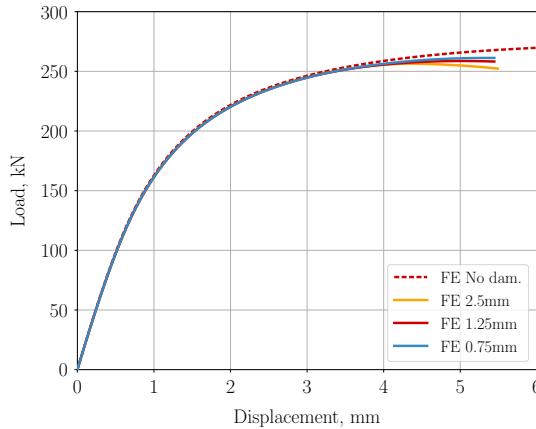


Figure 5.7: Load displacement curves of mesh-size sensitivity study of damage.

5.3.3 SKIN-STRINGER SEPARATION

It is chosen to model skin-stringer separation only in the panel with BVID. The skin-stringer interface of the stringer with BVID is investigated using a contact pair definition with the Virtual Crack Closure Technique (VCCT) for a partial bond. The bonded area is approximately 445 mm long and 9.7 mm wide, with 70 mm not bonded in the middle of this area to account for the BVID. In the model, separation can only occur in between the filler and skin, and no crack migration into the filler is allowed to lower the complexity of the model. This assumption is based on the failure behaviour of compression tests of three-stringer panels [16] and three-point bending tests on single stringer specimens [55]. VCCT is chosen over the cohesive zone method based on results achieved in previous work [16], where VCCT is chosen because of the courser mesh-size requirement [14, 35].

The VCCT definition includes mixed-mode interface behaviour with the Benzeggagh Kenane (BK) criterion [34, 59], for which the equations are reported in Equation 5.5 and Equation 5.6. The equations for the critical equivalent strain energy release rate G_{equivC} and the equivalent strain energy release rate G_{equiv} consist of the fracture toughness of the three different modes: G_{IC} , G_{IIC} and G_{IIIC} , and the strain energy release rates of each mode: G_{I} , G_{II} and G_{III} . Fracture of the interface occurs when G_{equiv} divided by G_{equivC} is equal or greater than one. The strain energy release rates are based on the nodal forces

and displacements. The fracture toughness of mode 1 and 2 are based on internal tests of GKN Fokker, and it is assumed that the fracture toughness of mode 3 is equal to mode 2. The BK parameter, η , of a similar thermoplastic composite is used, of which the properties are available in literature [37]. The interface properties are reported in Table 5.6.

$$G_{equivC} = G_{IC} + (G_{IIC} - G_{IC}) \left(\frac{G_{II} + G_{III}}{G_I + G_{II} + G_{III}} \right)^\eta \quad (5.5)$$

$$G_{equiv} = G_I + G_{II} + G_{III} \quad (5.6)$$

Table 5.6: Fracture properties of skin-stringer interface [16, 37].

G_{IC} [kJ/m ²]	G_{IIC} [kJ/m ²]	G_{IIIC} [kJ/m ²]	η [-]
1.41	1.9	1.9	2.3

The fracture tolerance and unstable crack growth tolerance of the VCCT definition are 0.2 and 10, respectively. The unstable crack growth tolerance allows for multiple nodes to be released within one increment, and can improve convergence and computational efficiency. The contact pair definition uses node-to-surface contact discretization, with the filler material as master and skin as slave surface, and contact stabilisation, for which a stabilisation factor of 1e-4 is used.

5.4 TEST SETUP

The curved multi-stringer panels are tested to investigate the post-buckling behaviour and the final failure mode and to validate the numerical analysis. A MTS test machine is used, which is capable of 3500 kN in compression.

The experimental test setup is shown in Figure 5.8 from the stringer-side of the panel (a), from the skin side (b) and with a top-view illustration (c). A female test fixture is clamped to the top compression plate and base of the test machine. The female test fixture is a machined aluminium profile with vertical uprights to limit the movement of the rollers, and to which white paint and black speckles are applied for Digital Image Correlation (DIC). The top and bottom female text fixtures are aligned such that the uprights on the right side, as seen in Figure 5.8(b), can be used to align the panel at the start of the test. The top fixture has hangers mounted to the side to catch the top roller in case of panel collapse. When compression is applied, the panel rolls to the left. When the panel fails, the female test fixtures are able to keep the panel in place. After panel alignment, a preload of approximately 2kN is applied to keep the panel in place.

The tests of panel 1 and panel 2 are executed at a loading rate of 0.25 mm/min. The force is measured by the load-cell of the MTS test machine and the displacement of the compression plate is measured by three Linear Displacement Sensors (LDS). Two LDS are placed next to the panel and one LDS is placed on the corner of the compression plate. The different locations allow to determine load imperfections, as shown in Figure 5.8(c). The displacement field of the panels is measured by two DIC systems, one system on the

stringer side of the panel and one system on the skin side of the panel. The systems have two cameras each, and the pictures are post-processed with VIC 3D 8. This measurement allows to determine the buckling shape from the out-of-plane displacement of the skin, the longitudinal shortening from the in-plane displacement of the female test fixtures, and the rotation of the rollers from the out-of-plane displacement.

The tests are also captured with four GoPro cameras, one placed on the skin-side, one placed on the stringer-side, and one placed on each lateral side of the panel. The cameras record phenomena such as buckling and skin-stringer separation events, besides capturing the sound of events which might not be visible, such as material failure.

Two high-speed cameras are used to record the final failure of the panels. One camera is placed on the cap-side of the stringers, focusing on the middle three stringers, that captures at 5600 and 5200 fps for the test of panel 1 and 2, respectively. The second high-speed camera is placed next to DIC system 2, which captures the whole panel at 10000 fps for panel 1 and 9600 fps for panel 2.

5

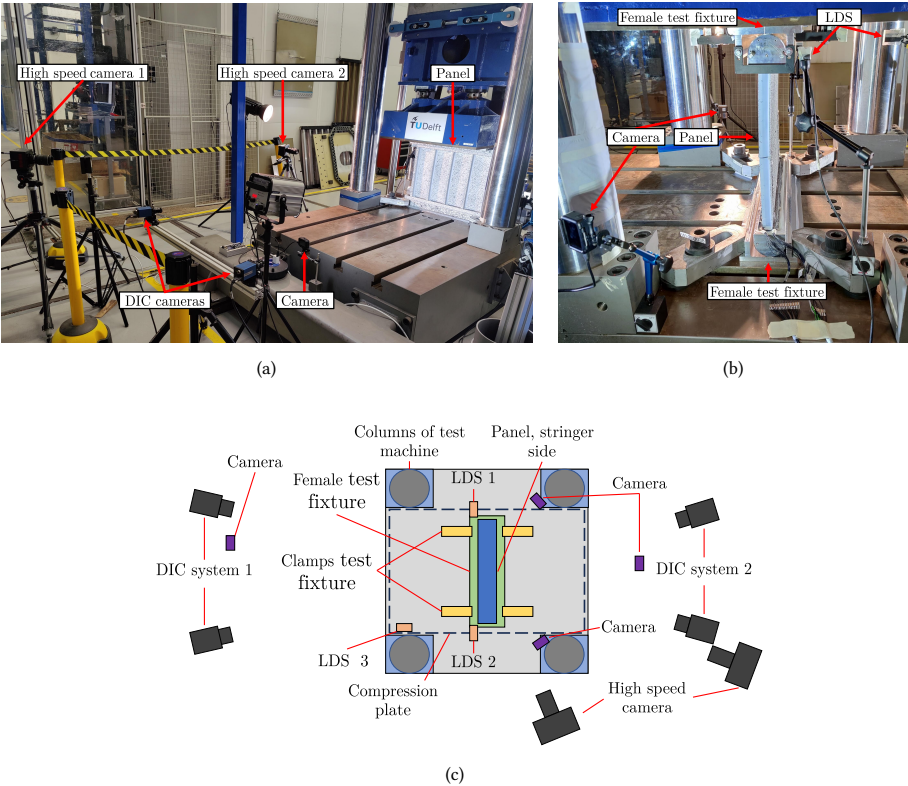


Figure 5.8: Test setup: (a) stringer side; (b) side-view; (c) top-view illustration.

5.5 TEST AND NUMERICAL RESULTS

This section discusses the results of the tests till failure of the two panels and compares them to the numerical analysis. Panel 1 was pre-tested till a displacement of 4.56 mm, which did not lead to failure, and the panel was then tested till failure. This section will only include the results of the test till failure for conciseness.

5.5.1 LOAD VERSUS DISPLACEMENT CURVES

The load-displacement curves of the tests and numerical analysis are reported in Figure 5.9. The panels show a decreasing stiffness due to the curved geometry and roller boundary condition, clearly seen at loads above approximately 120 kN. At higher loads close to failure, the load-displacement behaviour starts to plateau. The stiffness of panel 1 and panel 2 are similar. The stiffness of panel 1 is slightly lower between approximately 1 and 4 mm of displacement, which can be caused by material softening due to the pretest. Panel 1, with BVID, fails at a load of 251 kN and 5.22 mm of displacement, while panel 2 fails at a load of 249 kN and 5.06 mm of displacement. Unexpectedly, the panel with BVID shows a slightly higher failure load and displacement, which indicates that the BVID is not critical for the failure mode that causes the collapse.

The numerical analysis predicts the initial stiffness well, but above 100 kN it starts to over-predict the stiffness. However, the plateau behaviour at higher loads is predicted well. The analysis with VCCT is conservative in predicting failure due to skin-stringer separation, which did not appear to be the critical failure mode in the test. The following sections, therefore, only show results from the analysis without VCCT.

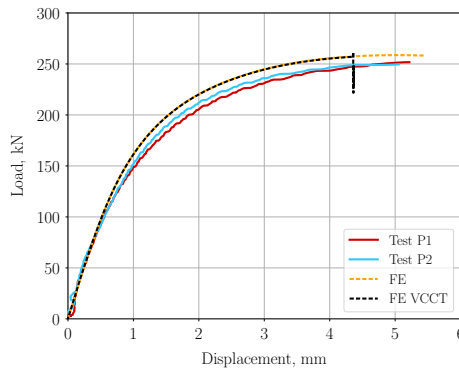


Figure 5.9: Load-displacement curves from tests and numerical analysis.

5.5.2 LOAD VERSUS ROTATION CURVES

The rotation is calculated from the average out-of-plane location of the top and bottom half of the flat vertical plane of the rollers, as measured by DIC, in combination with the height of this plane. The load-rotation curves of the tests and numerical analysis are reported in Figure 5.10. The load-rotation curves are similar to the load-displacement curves, with a decreasing stiffness with an increase in load and a plateau at higher applied displacements. There is a small difference in rotation between the top and bottom rollers initially for all

tests, which stays constant after settling. Panel 1 seems to have a slightly lower amount of rotation than panel 2, indicating a higher bending stiffness.

The numerical analysis predicts the rotation of the rollers well, with an under-prediction of the rotation at higher loads, above approximately 1.5 and 3 degrees of rotation for panels 1 and 2, respectively.

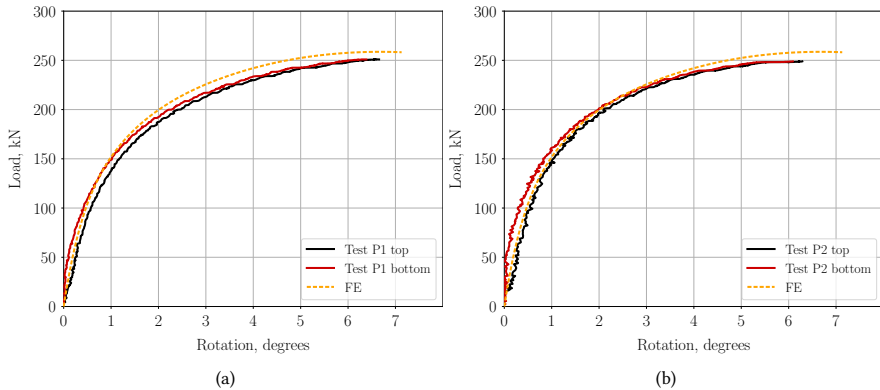


Figure 5.10: Load-rotation curves from tests and numerical analysis: (a) panel 1; (b) panel 2.

5.5.3 STRAIN GAUGE CURVES

The measured strains of the test till failure of panel 1 are reported in Figure 5.11. The strains measured by the skin strain gauges show negative strains, indicating compression, and the strain gauges on top of the stringer webs show positive strains, indicating tension. This is due to the combined compression and bending loading. The strains also reach higher values than the more typical compression tests, with strains up to 19400 microstrain. The strains show a slight loading imperfection in the skin, while the stringers are equally loaded. The outer stringers, strain gauges 4 and 16, do show differences, but this can also be caused by geometric differences instead of a loading imperfection. The highest strains are in the stringer area and free edges, with lower strains in the middle of the bay.

The measured strains of the test till failure of panel 2 are reported in Figure 5.12. The behaviour is very similar to panel 1. When the results of strain gauge 10 and 11 are compared between panel 1 and 2, no clear influence of the BVID of panel 1 can be distinguished.

The numerical analysis predicts the overall behaviour well, with a similar over-prediction of stiffness, and thus under-prediction of strain, at higher loads as for the load-displacement curves. The analysis does not consider loading imperfections, which is most noticeable for strain gauges 17 and 18. The strains in the stringer region seem slightly better predicted than in the skin region.

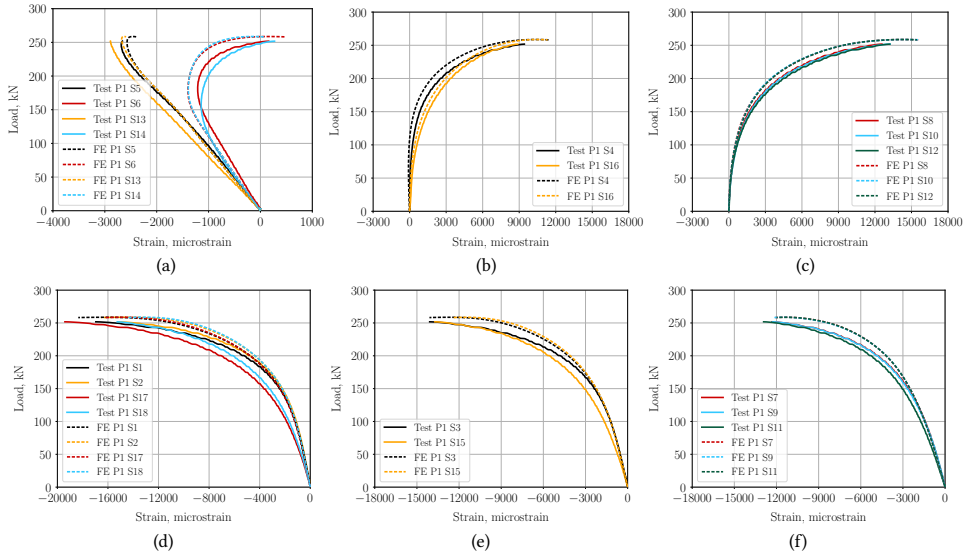


Figure 5.11: Experimental and numerical compressive strains of panel 1 with initial damage: (a) bays; (b) top of side stringers; (c) top of middle three stringers; (d) free edges; (e) bottom of side stringers; (f) bottom of middle three stringers.

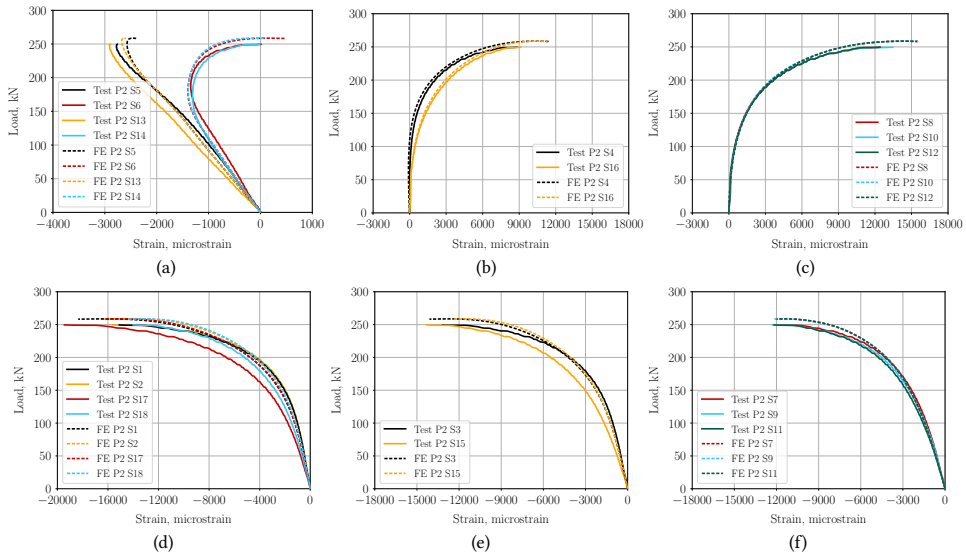


Figure 5.12: Experimental and numerical compressive strains of panel 2 in pristine condition: (a) bays; (b) top of side stringers; (c) top of middle three stringers; (d) free edges; (e) bottom of side stringers; (f) bottom of middle three stringers.

5.5.4 OUT-OF-PLANE DISPLACEMENT

The out-of-plane displacement of the skin is measured during the tests by DIC, and is reported in Figure 5.13. Negative displacement corresponds to an outward direction, and positive displacement corresponds to an inward direction, in line with the axis system reported in Figure 5.2(b). The scale of the contour plot is based on the out-of-plane displacement of the skin at the maximum load. For each plot, an offset is applied to the displacement field, such that the scale's maximum is at the maximum out-of-plane displacement point of the panel. This eliminates the contribution of the rolling motion of the panels to the out-of-plane displacement and results in a clearer comparison.

The out-of-plane displacement of the test of panel 1 is plotted in Figure 5.13(a-e) in steps of 1 mm of longitudinal applied displacement and at the maximum applied displacement. The panel shows a single half-wave in each bay, with the highest out-of-plane displacement at the left side of the panel. The evolution of the out-of-plane displacement is gradual, with an exponential increase of displacement w.r.t. the load. The three bays on the right initially have similar out-of-plane displacement, but at higher applied displacement, the bay on the rightmost side starts to have higher displacement than the middle two bays. At the maximum applied displacement, the difference in out-of-plane displacement is 2-2.5 mm between the middle two bays and most left bay, and a 1 mm difference between the most left and right bay. These differences can be due to loading imperfections but are also due to geometric differences. The middle two bays are stiffer due to the adjacent bays, while the two outside bays have a free edge nearby. The difference between the most left and right bay is partly due to the anti-symmetric stringer, which provides more stiffness when the cap is pointed towards the bay. In terms of loading imperfections, the differences can be due to both the difference in applied compression between left and right, in terms of roller rotation and the resulting out-of-plane displacement of the roller itself. With only a 1 mm difference in out-of-plane displacement between the most left and right bay, and considering the geometric differences, the loading imperfections are estimated to be small.

The out-of-plane displacement of the test of panel 2 till failure is plotted in Figure 5.13(f-j). The out-of-plane displacement behaviour of panel 2 is similar to panel 1, in terms of total out-of-plane displacement and the differences between the four bays. There is no visible difference in the out-of-plane displacement of panel 1 and 2 due to the BVID of panel 1.

The out-of-plane displacement of the numerical prediction is reported in Figure 5.13(k-o). The numerical analysis accurately predicts the out-of-plane displacement behaviour, with only minimal differences due to loading and geometric imperfections not considered in the analysis. The differences between the bays are lower than what is measured in the tests, with the most left and right bay having a 0.3 mm difference in out-of-plane displacement at 5 mm of applied displacement, and the middle two bays a 1 mm difference compared to the outer bays.

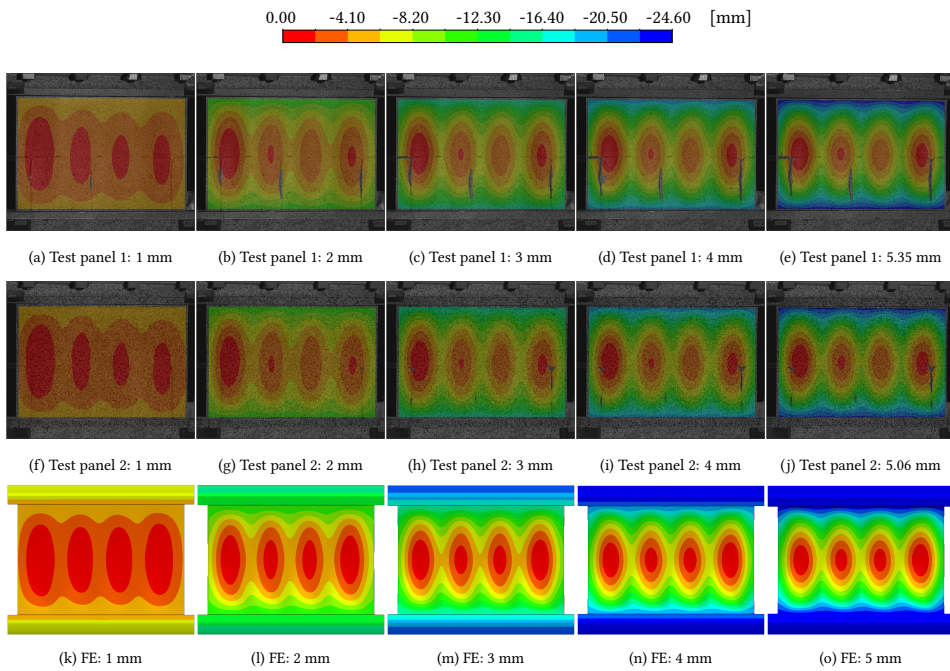


Figure 5.13: Out-of-plane displacement: (a-e) test panel 1; (f-j) test panel 2; (k-o) FE.

5.5.5 PANEL COLLAPSE

High-speed cameras are used to capture the collapse of the panels at a frame rate of 10000 fps for panel 1 and 9600 fps for panel 2. For the test of panel 1, the camera is positioned such that the BVID in the butt-joint is visible from the cap-side of the stringers, which results in only four visible stringers. This is, however, considered acceptable, as the stringers at the edges are not the main priority. The camera is positioned to the right side during the test of panel 2. The whole panel is captured, which requires lowering the frame rate to 9600 fps to compensate for the higher resolution.

The panel collapse sequence of panel 1 is reported in Figure 5.14 over a total time period of 1.1 ms. Panel collapse starts with the cap separating from the web of stringer 4 (a), the stringer with a BVID in the butt-joint skin-stringer interface. The cap completely separates in the following two frames and fractures at the top of the panel (b-c), followed by failure of the web (d). Then, the cap of stringer 3 separates from the web (e), and the cap fractures at the bottom of the panel (f). The web of stringer 3 fails next, and the web of stringer 2 shows delaminated plies at the web-cap interface (g). The cap of stringer 2 then separates almost completely from the web within one frame (h). The butt-joint of stringer 5 is the first visible skin-stringer interface that shows failure (i), with the failure occurring at the top of the panel. Due to the separation of the caps from the webs, most butt-joints can no longer be seen. After the butt-joint failure, the cap of stringer 5 separates from the web, simultaneously with the web fracture of stringer 2 (j-k). Lastly, the web of stringer 5 fails (l).

The frames of the high-speed footage are further analysed. When the caps separate from the web, the caps displace towards the skin in the middle of the panel. The caps hit the skin once or multiple times, with the skin also displacing out-of-plane in waves. When web fracture occurs, a few caps detach further and pull partially out of the potting material. After failure is completed, the caps return close to their initial position.

The panel collapse sequence of panel 2 is reported in Figure 5.15 over a total time period of 2.3 ms, as every 2nd frame is reported. Panel collapse starts with the separation of the cap of stringer 2 in the middle of the panel (a-b), with a fracture in the cap at the bottom of the panel. The butt-joint of stringer 2 then separates from the skin at the bottom of the panel (c), which grows in an upward direction and is followed by fracture of the web (d). The cap of stringer 2 then separates from the web and fractures at the bottom of the panel (e). The butt-joint of stringer 2 fails at two locations, in the middle and bottom of the panel, and the web fractures (f). In the same frame, the cap of stringer 4 starts to separate, followed by further separation and fracture of the cap and failure in the butt-joint (g). The web of stringer 4 then separates, while the cap of stringer 1 also separates from the web (h-i). The web of stringer 1 then fails and the cap of stringer 5 separates from the web (j). The butt-joint of both stringer 1 and 5 then fails (k), and lastly, the web of stringer 5 fractures (l).

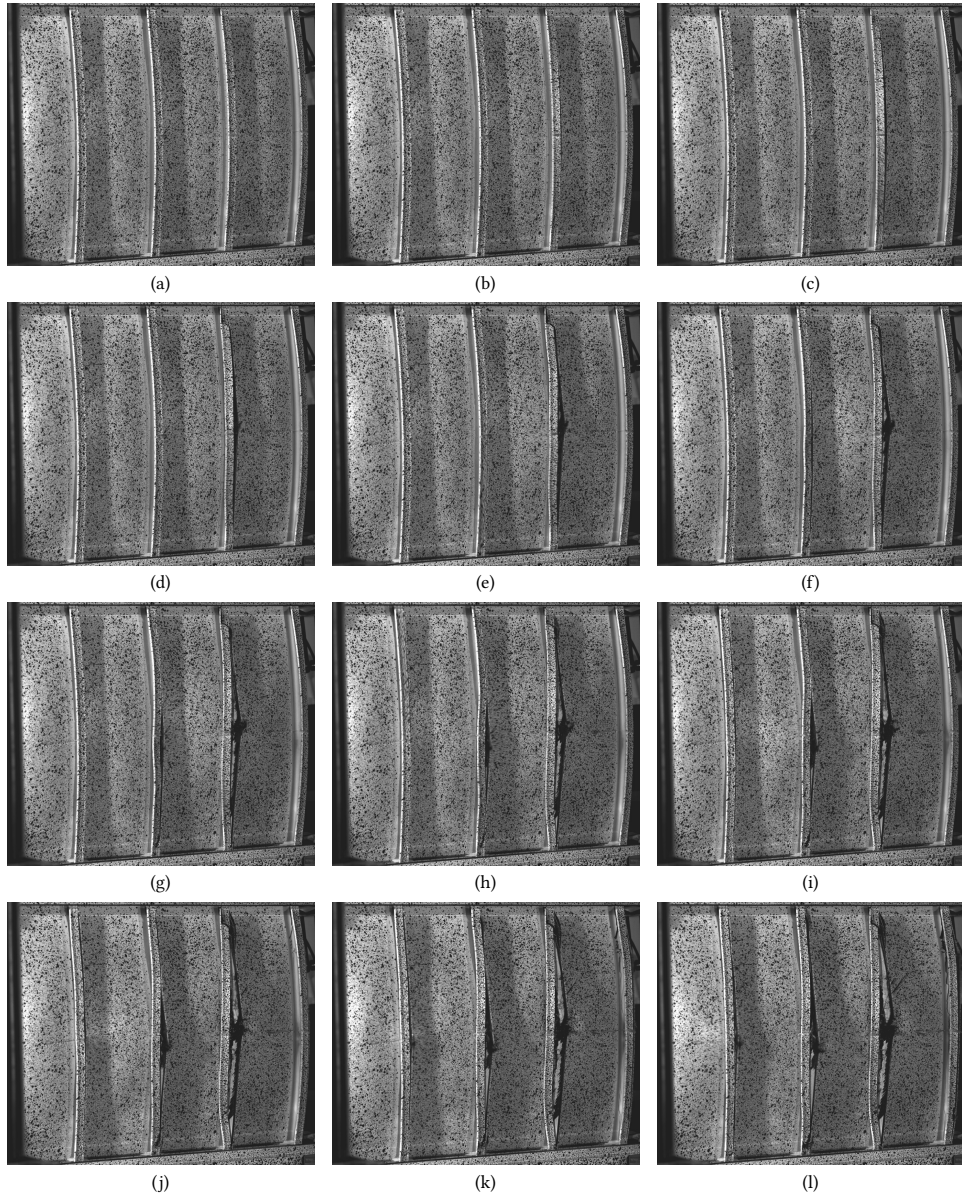


Figure 5.14: High-speed footage panel 1: (a-b-c) stringer 4 cap separation; (d) stringer 4 web fracture; (e-f) stringer 4 cap separation; (g) stringer 3 web fracture; (h) stringer 2 cap separation; (i) stringer 5 butt-joint failure; (j-k) stringer 2 web fracture, stringer 5 cap separation; (l) stringer 5 web failure.

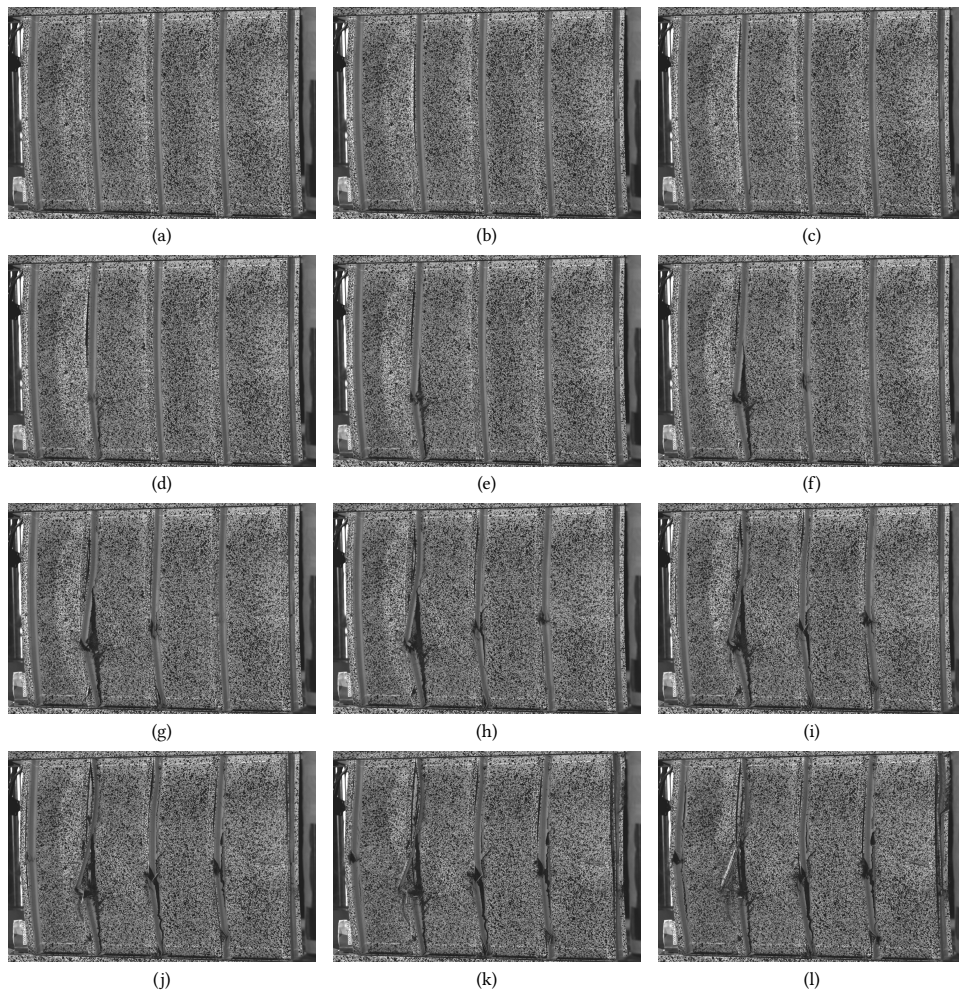


Figure 5.15: High-speed footage panel 2: (a-b) stringer 2 cap separation; (c) stringer 2 butt-joint failure; (d) stringer 2 web fracture; (e) stringer 3 cap separation; (f) stringer 3 butt-joint and web failure, stringer 4 cap separation; (g) stringer 4 butt-joint failure; (h-i) stringer 4 fracture, stringer 1 cap separation; (j) stringer 5 cap separation, stringer 1 web fracture; (k) stringer 1 and 5 butt-joint failure; (l) stringer 5 web fracture.

5.5.6 POST-FAILURE INVESTIGATION

Photos of panel 1 after failure are reported in Figure 5.16(a-c). The caps, once separated from the webs, show fractures in several locations. The caps of stringers 1, 2 and 5 are also partially pulled out from the potting material. The failure between cap and web seems to occur in two different ways, with the top ply of the web being delaminated and pulled off partially, and with separation between web and the short fibre filler. In the middle of the panel, it seems that failure and delamination of the web plies is more common, with small pieces of the ply still attached to the cap, while towards the top and bottom of the panel, failure occurs at the interface between the web and short fibre filler. All the webs separated from the skin at the butt-joint. The webs present one or more fractures in each web and parts of the web are no longer attached to the panel. The failure in the web and skin region is mostly in the butt-joint. Stringer 1 has a part of the ply delaminated from the skin at the bottom of the panel, and the remaining butt-joints only show minimal pulled-off fibres. Failure in the butt-joint can be roughly divided into three types of failure: failure at the interface between skin and butt-joint, failure in the short fibre filler and failure at the interface between web and butt-joint. There are no visible fractures in the skin, but there is likely damage inside the laminate. There are indications of damage at the back of the skin, with paint chipped off.

Photos of panel 2 after failure are reported in Figure 5.16(d-f). The failure modes, that are initially visible, are similar to panel 1. Stringer 2 fails first and has considerable amounts of fibre pullout from the skin, especially towards the top of the panel. The biggest difference, however, is that the edge of the skin, on the side of stringer 5, shows a large fracture. A close-up picture of this fracture is reported in Figure 5.17. The skin is fractured across the thickness of the laminate and has a visible length of approximately 60 mm as seen from the stringer-side of the panel. Further propagation is visible on the back side of the skin, with propagation in a downward direction, leading to a total visible length of approximately 100 mm.

Both panels show failure first in the web-cap joint area. The cap-web failure of panel 1 occurs in the stringer with a BVID in the butt-joint, but the BVID itself is not necessarily critical, with no indication of crack growth before panel collapse. From panel 1, a close-up of the stringer 4 cap and of the web is reported in Figure 5.18(a-b). There are web plies still attached to the cap, both the -45 ply and parts of the 90 ply, which indicate that the critical failure mode is a combination of both the failure of these plies and delamination. Panel 2 fails in stringer 2, and the criticality of this stringer out of the three middle stringers is most likely due to imperfections. The stringer 2 web of panel 2, as reported in Figure 5.18(c), shows similar damage as stringer 4 of panel 1. The 45 ply is visible at the top of the web, as the -45 ply and 90 ply present failure as well as delamination, indicating the same failure mode as panel 1.



Figure 5.16: Post-failure photos: (a) panel 1 left-view; (b) panel 1 right-view; (c) panel 1 side-view; (d) panel 2 left-view; (e) panel 2 right-view; (f) panel 2 side-view.



Figure 5.17: Skin fracture of panel 2.

Although the numerical model is not able to predict the sudden failure of the panel, as it does not take into account delamination between each ply, it is able to correctly identify the critical plies. Contour plots of the Hashin matrix tensile damage variable are reported in Figure 5.19 for the middle three webs (a), the skin (b) and the full panel (c). The top -45 ply is most critical in the web, closely followed by the 45 ply. At 5.26 mm of displacement, the area with a damage variable higher than 0.99 for the -45 ply reaches the bottom of the cap-web joint. This means that the short fibre filler joint is locally connected only to a failed ply, at the free edge of the web laminate.

The skin also has areas with a damage variable above 0.99, and the top 45 ply is the most critical. However, this can be considered less critical than the web, as the top skin plies are in tension, with no free edge and continuous fibres underneath the joint, making it less likely for this ply to delaminate compared to the web plies.

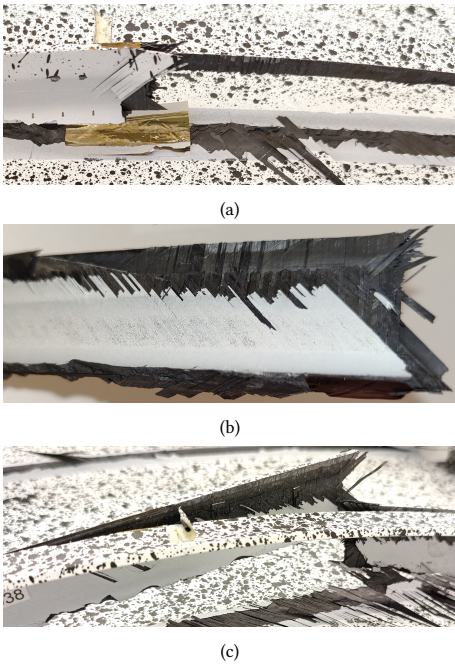


Figure 5.18: Fracture photos: (a) panel 1 web and stringer; (b) panel 1 web; (c) panel 2 web and cap.

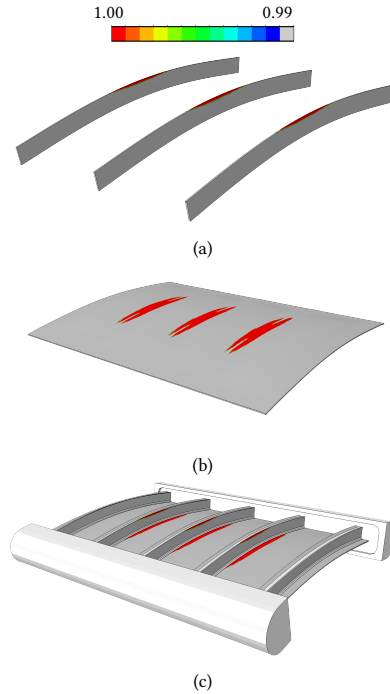


Figure 5.19: Matrix tensile damage variable contour plot, at 5.26 mm of displacement: (a) middle three webs; (b) skin; (c) panel.

5.6 CONCLUDING REMARKS

Two curved multi-stringer panels with butt-joint and roller boundary conditions were successfully tested and analysed, with one panel in pristine condition and one with initial damage in the butt-joint representing BVID.

The load-displacement behaviour of the panels shows a gradual decrease in stiffness for an increase in applied displacement due to the initial curvature, roller boundary condition and buckling of the bays. The bays show a single half-wave buckling shape, with a slight variation in out-of-plane displacement between the bays, due to the anti-symmetric stringer and a small loading imperfection. The load-displacement curve starts to plateau at higher applied displacement, followed by panel collapse. The panels can sustain considerably high strains before failure, up to 19400 microstrain. The panels fail when the caps separate from the web, followed by failure in the skin-stringer butt-joint and web fracture.

Three different approximations of the roller boundary conditions were analysed and compared, and the Hashin damage criterion is included in the analysis to determine damage initiation followed by evolution.

The analysis can predict the load-displacement and buckling behaviour well, but cannot predict the panel collapse and sudden loss of load-carrying capability due to the cap-web failure. The model with VCCT for skin-stringer separation predicts a conservative failure load, which might be caused by the idealized BVID with frictionless contact. Predicting the cap-web failure would require a more detailed model to allow each ply to delaminate. However, the model predicts the correct critical plies and shows that these have almost fully softened in the joint area, close to the failure displacement of the tests. This shows great promise for the ability to predict such a complex test and failure behaviour.

This research demonstrates that the roller boundary conditions approximate a loading condition that is likely to be more representative of aeronautical flight, and showcase the excellent capabilities of thermoplastic composites for primary structures in post-buckling.

6

CONCLUSIONS AND RECOMMENDATIONS

6.1 CONCLUSIONS

This thesis presents analyses and testing of thermoplastic composite stiffened panels in post-buckling, investigating skin-stringer separation. Two different configurations of stiffeners are considered. First, panels with welded interfaces are designed based on the structural behaviour of a fuselage panel and further analysed for damage tolerance. Then, a more non-conventional stringer design with butt-joint skin-stringer interface is analysed and tested. The research demonstrates the extensive possibilities w.r.t. designs and manufacturing of thermoplastic composites for stiffened panels and the robustness of using classical analysis methods developed initially for thermoset composites. The conclusions of each chapter are summarised as follows:

- In *chapter 2*, the conduction welded skin-stringer interface of the thermoplastic composite fuselage demonstrator of the STUNNING project is investigated, by the design, analysis, and testing of three-stringer panels. Initial analysis of a fuselage section is the reference for the panel design, with emphasis on the post-buckling behaviour and failure. The critical failure mode of the fuselage is skin-stringer separation, which starts from underneath the stringer, and grows towards the bay. The initial analysis of the three-stringer panel design indicates a high level of similarity in structural behaviour with the fuselage section, albeit with a higher number of failure locations, possibly due to the differences in boundary conditions.

Two pristine three-stringer panels are manufactured and tested, presenting consistent pre-buckling stiffness, buckling load, and an initial buckling shape of three half-waves. One of the panels shows a buckling shape transition to four half-waves, while the buckling shape of the other panel remains three half-waves. This can be due to differences in geometrical imperfections or loading imperfections. The welded joints demonstrate great performance in post-buckling, with the ability to sustain the deformation of buckling far into the post-buckling field. The buckling

load and final failure load ratio reaches 1.94 and 1.87 for panels 1 and 2, respectively. The high-speed footage indicates that skin-stringer separation is the critical failure mode, which starts from underneath the stringer and develops in both outward and longitudinal directions. Both panels show the number of half-waves increasing beneath the stringer before the final failure, highlighting the importance of this region's buckling shape.

The numerical analyses, with geometrical imperfections included, accurately predict the structural behaviour, with a minor difference in the evolution of the panel 1 buckling shape and a high level of similarity for the skin-stringer separation behaviour. These findings establish the methodology as a reliable tool for the post-buckling analysis of panels with welded interfaces. Furthermore, the impressive post-buckling performance and predictability of the structural behaviour hold promise for the application of thermoplastic composites in primary aeronautical structures.

- In *chapter 3*, four thermoplastic stiffened panels are analysed and tested to investigate the welded interface damage tolerance.

The sensitivity studies reveal that for one initial damage, the initial damage location mainly affects the initiation of skin-stringer separation, while its impact on the final failure load is considered minimal. When two initial damages are present, the damage in the middle of the panel remains critical for final failure. However, the initiation load for skin-stringer separation is influenced by the damage location that is off-centre.

The maximum damage size for the sensitivity study was 100 mm, chosen such that buckling can still occur before final failure. The study demonstrated that geometrical imperfections decreased the failure load of pristine panels, while it increased the loads for panels with initial damage. Stable separation growth occurs for damage sizes above 40 mm, and appears to delay final failure, as larger damages affect the initiation load more than the failure load.

Then, three panels with initial damage and one panel in pristine condition were tested. The initial damage primarily affects the failure load, with minimal effects on the stiffness and buckling load. The maximum decrease of the failure load due to initial damage is 16.6%, for the panel with two damages. Initial damage in the middle of the panel remains critical when a second initial damage is present off-centre. However, the off-centre damage increases the criticality of the initial damage in the middle of the panel. Damage in the side stringer appears more critical for one initial damage, with a lower failure load than the panel with initial damage in the middle stringer. This is unexpected, as the middle stringer should attract more load and consequently be more critical for damage.

The introduction of initial damage appears to make buckling shape changes more gradual, possibly caused by the opening of the damage, which was evident from the DIC measurement. Panels with initial damage present stable separation growth before final failure. The panel with two initial damages demonstrated that the middle stringer can withstand a considerable skin-stringer separation event without showing signs of damage. However, due to the lower skin-stringer separation load, there is also less load to redistribute within the panel. Additionally, the separation

growth seems to be stopped at the initial damages.

The numerical analysis is capable of predicting the overall structural behaviour well but has difficulty predicting the buckling shape evolution to four half-waves. The predictions of failure loads are conservative for panels with initial damage in the middle stringer, while the failure load of the panel with initial damage in the side stringer is over-predicted.

This research demonstrates that the welded joints can endure considerable buckling deformation well into the post-buckling field with one or two initial damages of 40 mm. It should be noted that the chosen damage size was conservative due to uncertainties regarding weld strength when manufacturing started. Nevertheless, the failure loads are predicted well by the numerical analyses, and the sensitivity study showed that panels with larger damage sizes can still withstand load into post-buckling. This work underlines the great potential for thermoplastic composite primary structures, also considering the damage tolerance behaviour.

- *Chapter 4* reports the study on thermoplastic composite stiffened panels that use the butt-joint technique. They are tested and analysed with a representation of Barely Visible Impact Damage (BVID) in the skin-stringer interface. The panels present an anti-symmetric three half-wave buckling shape, with a fourth half-wave appearing in one bay at higher loads. The buckling shape greatly influences the skin-stringer separation behaviour, as the crack is opened on the cap-side of the stringer and closed on the other side due to the anti-symmetry. The initial damage separates further in post-buckling, consisting of stable growth and unstable separation events. This can be attributed to both the thermoplastic composite material and the design of the butt-joint and stringer. This behaviour continues till more than double the buckling load, when the middle stringer separates in an unstable manner, and the panel collapses. The behaviour in the post-buckling field differs considerably from the more conventional designs of thermoset stiffened panels.

Finite Element analyses are performed, which include the Virtual Crack Closure Technique (VCCT) to model skin-stringer separation. The analyses accurately predict the structural behaviour, with the post-buckling stiffness slightly over-predicted following separation events. However, the analysis accurately predicts the buckling shape, the behaviour in the post-buckling field, the skin-stringer separation behaviour and the final failure load and sequence. The results demonstrate that the numerical analyses are a reliable design tool for thermoplastic aeronautical structures.

- *Chapter 5* investigates curved multi-stringer panels with the butt-joint technique, featuring roller boundary conditions, by test and analysis. One panel has initial damage in the skin-stringer interface, representing BVID, and one panel is in pristine condition. The panels show load-displacement behaviour with a gradual stiffness decrease with increasing applied displacement. This behaviour can be attributed to the roller boundary conditions, the initial curvature and the buckling of the bays. The bays buckle with a single half-wave buckling shape, with minor differences in out-of-plane displacement for each bay. These differences are most likely caused by the anti-symmetric stringer design and slight loading imperfections. At higher

applied displacement, the load-displacement curve reaches a plateau before the panel collapses. The panels are able to withstand considerably high strains before the collapse, with the strain gauges measuring up to 19400 microstrain at the free edges of the skin.

Panel collapse starts with the cap separating from the web, after which the butt-joint fails and the web fractures. The BVID is not the critical factor leading to failure, as there is no visible indication of the damage growing before the panel collapses. Further investigation of the failed panels indicates that the failure of the cap-web joint is caused by failure and delaminations of the top plies of the web, which remain attached to the cap at the initial failure locations.

The roller boundary conditions are approximated by three different methods in the numerical analyses. The method that models the roller and connects the roller contact surface to a reference point is considered the best. This eliminates the need to model contact for better computational efficiency while maintaining an accurate prediction of the structural behaviour. Initiation of material damage is modelled with the Hashin damage criterion.

While the analysis is capable of predicting the load-displacement and buckling behaviour, it is not able to predict panel collapse and abrupt loss of load-carrying ability due to the failure of the cap-web joint. However, the analysis predicts the critical plies, with almost complete softening in the joint area, close to the failure displacement of the tests. This indicates great promise for further developments to predict this complex failure mode.

This research highlights the excellent structural capabilities of thermoplastic composites in post-buckling for primary aeronautical structures. Using the more complex roller boundary conditions allows for more representative loading conditions for curved aeronautical structures.

The extensive analysis and testing of thermoplastic composite stiffened structures in this thesis highlight the great potential for thermoplastic aeronautical primary structures. The panels demonstrate great load-carrying capabilities in post-buckling, also when initial damage is present, and failure loads of almost double the buckling load are achievable. The tests have a high level of repeatability, demonstrating the maturity and high quality of the manufacturing processes.

The different design philosophies of the investigated stiffened structures caused considerably different behaviour in post-buckling, both in terms of the buckling shape evolution and the skin-stringer separation behaviour.

The omega stringer displays quite complex buckling behaviour, with more possibilities in terms of buckling shapes in the bay and underneath the stringer, and shape changes occurring both gradually and suddenly. Although there are indications of stable separation growth, the majority of separation events with the omega stringer are unstable and sudden, both for pristine panels and panels with initial damage.

The stiffened panels with butt-joint tested in pure compression showed more gradual buckling behaviour, with no sudden shape changes. The only shape evolution is an additional fourth half-wave in one bay at higher loads. The separation behaviour in post-buckling displayed a considerable amount of stable separation growth before panel collapse, with the growth clearly visible from the cap-side of the stringer.

The test with curved butt-joint panels on rollers allowed to investigate a different testing method and the resulting failure mode. The panels demonstrated the ability to withstand considerably high strains before the collapse, highlighting the performance of joints with short fibre filler material such as the butt-joint technique. The testing method is demonstrated to be reliable, even though it's a more complex boundary condition, with a relatively small contact surface being loaded and a rolling motion. The complex boundary conditions did not hinder the ability to predict the structural behaviour with numerical analysis.

The numerical modelling approach demonstrated capabilities to model different structural behaviours in post-buckling, depending on the geometry and materials. The modelling of skin-stringer separation with VCCT is usually limited to structures with initial damage, which is overcome by the presented approach for pristine welded interfaces. This allows for efficient modelling of larger pristine structures. The unconventional skin-stringer interface of the butt-joint technique is approximated with solid elements for the short-fibre filler and shell elements for the laminates, with the VCCT at the interface. The complex separation behaviour is predicted accurately compared to the tests and shows the robustness of such techniques, even for unconventional designs resulting from new manufacturing techniques.

This work shows great promise for thermoplastic composites, the ability to predict their structural behaviour, design tests by numerical analysis, and limit the number of tests needed in the development of new aeronautical structures for sustainable aviation.

6.2 RECOMMENDATIONS

The work presented in this thesis describes methods for the testing and analysis of thermoplastic composite stiffened structures, a method for designing representative panels and a wide variety of test results and numerical predictions. Recommendations are formulated based on this research, separated into recommendations for testing and numerical work, which are as follows:

Testing

- The current testing methodology utilises cameras, high-speed cameras, strain gauges and digital image correlation to capture the structural behaviour of the panels, such as buckling and skin-stringer separation events. To capture local phenomena in more detail, techniques such as acoustic emission monitoring, optic strain sensors and thermography could be interesting. The tests of the welded stiffened panels, both in pristine and with initial damage, indicated stable separation growth, but the extent of this growth is difficult to determine. The proposed methods would provide a higher level of detail to investigate the local phenomena and provide more details for further developments and improvements of the numerical analyses. Testing at panel level is an expensive venture, and maximising the knowledge gained per test is therefore of utmost importance.
- The stiffened panels in this thesis are tested under quasi-static conditions. The panels have shown that stable separation growth can occur in the post-buckling field, both relatively early after buckling and far into the post-buckling field, depending on stringer geometry and the initial damage, and it is therefore recommended to test the panels for fatigue in post-buckling. There is extensive literature on the fatigue behaviour of thermoset composite stiffened panels, but very minimal, if any, literature on the thermoplastic counterpart. These tests will increase the required knowledge of thermoplastic composites and aid in developing thermoplastic primary structures while providing more data to extend the numerical tools.

Numerical

- The geometrical imperfections are included in the numerical analysis of most panels efficiently with a linear analysis to create a nodefile. The imperfections are measured by DIC from the skin-side of the panels and applied to the skin-side of the numerical models. This method was initially developed for the panels with butt-joint stringers, and also applied to the welded panels with omega stringers. The panels with omega stringers seem more sensitive to imperfections and have a wider variety of buckling shapes, which can increase the importance of including imperfections. This leads to the recommendation to study the effect of including imperfections on the stringer side of the panels, mainly consisting of the shape of the omega web and cap. This will require combining DIC measurements of both sides of the panel, to create a realistic representation of the panels with imperfections. The new approach could first apply the imperfections of each stringer while keeping the skin flat, followed by restraining the imperfect stringer shape and allowing it to move as a rigid body while applying the skin-side imperfection.

- For the numerical analysis of panels with butt-joint technology, it could be of interest to explore alternative modelling techniques for pristine joints, such as the cohesive zone method. It could also be considered to combine modelling techniques, for example, to model initiation with the cohesive zone method in critical areas and model propagation with the VCCT to retain a coarser mesh in less critical areas.
- The current implementation of VCCT in the numerical analysis is based on a single fracture toughness value per mode of interface loading. It can be of interest to separate the behaviour for initiation and propagation, as VCCT is used to model both pristine interfaces and interfaces with initial damage. The commercial software package Abaqus, as used in this work, does support initiation and propagation values with the enhanced VCCT implementation, which can be further explored but requires more material data.
- The test and analysis of the curved multi-stringer panels presented material failure and delamination of plies in the web, which led to the failure of the web-cap joint. Modelling each ply separately to allow for failure and delamination is complex and computationally inefficient, especially for larger structures. It would, therefore, be interesting to investigate how this type of failure mode can be modelled efficiently.

BIBLIOGRAPHY

URLs in this thesis have been archived on Archive.org. Their link target in digital editions refers to this timestamped version.

REFERENCES

- [1] Thomas de Bruijn and Ferrie van Hattum. Rotorcraft access panel from recycled carbon pps – the world’s first flying fully recycled thermoplastic composite application in aerospace. *Reinforced Plastics*, 65(3):148–150, 2021.
- [2] Maxime Roux, Nicolas Eguémann, Clemens Dransfeld, Frédéric Thiébaud, and Dominique Perreux. Thermoplastic carbon fibre-reinforced polymer recycling with electrodynamical fragmentation: From cradle to cradle. *Journal of Thermoplastic Composite Materials*, 30(3):381–403, 2017.
- [3] A. Offringa, J.W. van Ingen, and A. Buitenhuis. Butt-joined, thermoplastic stiffened-skin concept development. *SAMPE Journal*, 48(2):7–15, 2012.
- [4] J.W. van Ingen. Thermoplastic orthogrid fuselage shell. *SAMPE Journal*, 52(5):7–15, 2016.
- [5] J.W. van Ingen, J.E.A. Waleson, A. Offringa, and M. Chapman. Double curved thermoplastic orthogrid rear fuselage shell. In *SAMPE Europe Conference. Nantes, France*, pages 1–10, 2019.
- [6] S.L. Omairey, S. Sampethai, L. Hans, C. Worrall, S. Lewis, D. Negro, T. Sattar, E. Ferrera, E. Blanco, J. Wighton, L. Muijs, S.L. Veldman, M. Doldersum, R. Tonnaer, N. Jayasree, and M. Kazilas. Development of innovative automated solutions for the assembly of multifunctional thermoplastic composite fuselage. *The International Journal of Advanced Manufacturing Technology*, 117(5):1721–1738, 2021.
- [7] B.H.A.H. Tijs, K.S. van Dooren, and C. Bisagni. Development of a numerical framework for virtual testing to support design of a next generation thermoplastic multifunctional fuselage. In *II European Conference On Multifunctional Structures (EMuS2020)*, pages 90–95, 2020.
- [8] Composites World. STUNNING project completes lower half of MFFD, 2023.
- [9] B.H.A.H. Tijs, M.H.J. Doldersum, A. Turon, J.E.A. Waleson, and C. Bisagni. Experimental and numerical evaluation of conduction welded thermoplastic composite joints. *Composite Structures*, 281:114964, 2022.

- [10] B.H.A.H. Tijs, S. Abdel-Monsef, J. Renart, A. Turon, and C. Bisagni. Characterization and analysis of the interlaminar behavior of thermoplastic composites considering fiber bridging and R-curve effects. *Composites Part A: Applied Science and Manufacturing*, 162:107101, 2022.
- [11] N. Li and P. Chen. Prediction of Compression-After-Edge-Impact (CAEI) behaviour in composite panel stiffened with i-shaped stiffeners. *Composites Part B: Engineering*, 110:402–419, 2017.
- [12] C. Meeks, E. Greenhalgh, and B. G. Falzon. Stiffener debonding mechanisms in post-buckled CFRP aerospace panels. *Composites: Part A*, 36:934–946, 2005.
- [13] R. Vescovini, C.G. Dávila, and C. Bisagni. Failure analysis of composite multi-stringer panels using simplified models. *Composites: Part B*, 45:939–951, 2013.
- [14] J. Bertolini, Br. Castanié, J. J. Barrau, and J. P. Navarro. Multi-level experimental and numerical analysis of composite stiffener debonding. part 1: Non-specific specimen level. *Composite Structures*, 90(4):381–391, 2009.
- [15] J. Bertolini, B. Castanié, J. J. Barrau, J. P. Navarro, and C. Petiot. Multi-level experimental and numerical analysis of composite stiffener debonding. part 2: Element and panel level. *Composite Structures*, 90:392–403, 2009.
- [16] K.S. van Dooren, B.H.A.H. Tijs, J.E.A. Waleson, and C. Bisagni. Skin-stringer separation in post-buckling of butt-joint stiffened thermoplastic composite panels. *Composite Structures*, 304:116294, 2023.
- [17] J.R. Reeder. An evaluation of mixed-mode delamination failure criteria. *NASA Technical Memorandum*, NASA-TM-104210, 1992.
- [18] M. Flanagan, A. Doyle, K. Doyle, M. Ward, M. Bizeul, R. Canavan, B. Weaver, C.M. Ó Brádaigh, N.M. Harrison, and J. Goggins. Comparative manufacture and testing of induction welded and adhesively bonded carbon fibre peek stiffened panels. *Journal of Thermoplastic Composite Materials*, 32(12):1622–1649, 2018.
- [19] D. Peeters, G. Clancy, V. Oliveri, R. O’Higgins, D. Jones, and P.M. Weaver. Concurrent design and manufacture of a thermoplastic composite stiffener. *Composite Structures*, 212:271–280, 2019.
- [20] V. Oliveri, G. Zucco, D. Peeters, G. Clancy, R. Telford, M. Rouhi, C. McHale, R. M. O’Higgins, T. M. Young, and P. M. Weaver. Design, manufacture and test of an in-situ consolidated thermoplastic variable-stiffness wingbox. *AIAA Journal*, 57(4):1671–1683, 2019.
- [21] C.B.G. Brito, J. Teuwen, C.A. Dransfeld, and I.F. Villegas. The effects of misaligned adherends on static ultrasonic welding of thermoplastic composites. *Composites Part A: Applied Science and Manufacturing*, 155:106810, 2022.

- [22] C.B.G. Brito, J. Teuwen, C.A. Dransfeld, and I.F. Villegas. On improving process efficiency and weld quality in ultrasonic welding of misaligned thermoplastic composite adherends. *Composite Structures*, 304:116342, 2023.
- [23] N.R. Kolanu, G. Raju, and M. Ramji. A unified numerical approach for the simulation of intra and inter laminar damage evolution in stiffened CFRP panels under compression. *Composites Part B*, 190 (2020)(107931), 2020.
- [24] Y. Mo, D. Ge, and B. He. Experiment and optimization of the hat-stringer-stiffened composite panels under axial compression. *Composites Part B: Engineering*, 84:285–293, 2016.
- [25] A.C. Orifici, I.O. de Zarate Alberdi, R.S. Thomson, and J. Bayandor. Compression and post-buckling damage growth and collapse analysis of flat composite stiffened panels. *Composites Science and Technology*, 68:3150–3160, 2008.
- [26] A. Riccio, A. Raimondo, G. Di Felice, and F. Scaramuzzino. A numerical procedure for the simulation of skin–stringer debonding growth in stiffened composite panels. *Aerospace Science and Technology*, 39:307–314, 2014.
- [27] R. Degenhardt, A. Kling, K. Rohwer, A. C. Orifici, and R. S. Thomson. Design and analysis of stiffened composite panels including post-buckling and collapse. *Computers & Structures*, 86(9):919–929, 2008. Composites.
- [28] A.C. Orifici, R.S. Thomson, R. Degenhardt, A. Kling, K. Rohwer, and J. Bayandor. Degradation investigation in a postbuckling composite stiffened fuselage panel. *Composite Structures*, 82(2):217–224, 2008.
- [29] C. Bisagni, R. Vescovini, and C.G. Dávila. Single-stringer compression specimen for the assessment of damage tolerance of postbuckled structures. *Journal of Aircraft*, 48(2):495–502, 2011.
- [30] A. Raimondo, S.A. Doesburg, and C. Bisagni. Numerical study of quasi-static and fatigue delamination growth in a post-buckled composite stiffened panel. *Composites Part B*, 182 (2020)(107589), 2020.
- [31] J. Paz, A. Raimondo, and C. Bisagni. Experimental study of post-buckled single-stringer composite specimens under fatigue loads with different load levels and load ratios. *Composites Part B: Engineering*, page 110606, 2023.
- [32] L.J. Kootte. A methodology to reproduce postbuckling in composite panels to study skin stringer separation. 2023.
- [33] N.C.A.M.P, Wichita State University. Medium Toughness PAEK thermoplastics Toray (Formerly TenCate) Cetex TC1225 (LM PAEK) T700GC 12K T1E Unidirectional Tape 145 gsm 34% RC Qualification Material Property Data Report. 25-5-2020.
- [34] Abaqus 2021 documentation. *Dassault Systemes Simulia Corp.*, 2021.

- [35] R. Krueger. An approach to assess delamination propagation simulation capabilities in commercial finite element codes. *NASA Technical Memorandum*, NASA/TM-2008-215123, 2008.
- [36] R. Krueger. A summary of benchmark examples to assess the performance of quasi-static delamination propagation prediction capabilities in finite element codes. *Journal of Composite Materials*, 49:3297–3316, 2014.
- [37] P. P. Camanho, C. G. Dávila, and M. F. de Moura. Numerical simulation of mixed-mode progressive delamination in composite materials. *Journal of Composite Materials*, 37(16):1415–1438, 2003.
- [38] K.S. van Dooren and C. Bisagni. Design, analysis and testing of thermoplastic welded stiffened panels to investigate skin-stringer separation in post-buckling. *Composites Part B: Engineering*, 267:111033, 2023.
- [39] B.G. Falzon, K.A. Stevens, and G.O. Davies. Postbuckling behaviour of a blade-stiffened composite panel loaded in uniaxial compression. *Composites: Part A*, 31:459–468, 2000.
- [40] C. Bisagni and C.G. Dávila. Experimental investigation of the postbuckling response and collapse of a single-stringer specimen. *Composite Structures*, 19:493–503, 2014.
- [41] J. Action and F. A. Leone. Progressive damage failure analysis of a multi-stringer post-buckled panel. *AIAA SciTech 2020 Forum*, (2020-1481), 2020.
- [42] Y. Mo, D. Ge, and J. Zhou. Experiment and analysis of hat-stringer-stiffened composite curved panels under axial compression. *Composite Structures*, 123:150–160, 2015.
- [43] Y. Feng, H. Zhang, X. Tan, Y. He, T. An, and J. Zheng. Effect of impact damage positions on the buckling and post-buckling behaviors of stiffened composite panel. *Composite Structures*, 155:184–196, 2016.
- [44] R. Sepe, A. De Luca, G. Lamanna, and F. Caputo. Numerical and experimental investigation of residual strength of a LVI damaged CFRP omega stiffened panel with a cut-out. *Composites Part B: Engineering*, 102:38–56, 2016.
- [45] T. Ishikawa and M. Matsushima. Compression after impact (CAI) properties of hat stiffened CF/PEEK panels fabricated through a route without autoclave. *Proc. 11th Int. Conf. on Composite Materials*, 2:1–9, 1997.
- [46] R. Ji, L. Zhao, K. Wang, F. Liu, Y. Gong, and J. Zhang. Effects of debonding defects on the postbuckling and failure behaviors of composite stiffened panel under uniaxial compression. *Composite Structures*, 256:113121, 2021.
- [47] J.E. Yetman, A.J. Sobey, J.I.R. Blake, and R.A. Shenoi. Investigation into skin stiffener debonding of top-hat stiffened composite structures. *Composite Structures*, 132:1168–1181, 2015.

- [48] C. Bisagni and P. Cordisco. An experimental investigation into the buckling and post-buckling of CFRP shells under combined axial and torsion loading. *Composite Structures*, 60(4):391–402, 2003.
- [49] B. Vieille, V. M. Casado, and C. Bouvet. About the impact behavior of woven-ply carbon fiber-reinforced thermoplastic- and thermosetting-composites: A comparative study. *Composite Structures*, 101:9–21, 2013.
- [50] T.P.A. Hernandez, A.R. Mills, and H. Yazdani Nezhad. Shear driven deformation and damage mechanisms in high-performance carbon fibre-reinforced thermoplastic and toughened thermoset composites subjected to high strain loading. *Composite Structures*, 261:113289, 2021.
- [51] A.C. Orifici, R.S. Thomson, I. Herszberg, T. Weller, R. Degenhardt, and J. Bayandor. An analysis methodology for failure in postbuckling skin–stiffener interfaces. *Composite Structures*, 86(1):186–193, 2008. Fourteenth International Conference on Composite Structures.
- [52] C. G. Dávila and C. Bisagni. Fatigue life and damage tolerance of postbuckled composite stiffened structures with initial delamination. *Composite Structures*, 161:73–84, 2017.
- [53] L.J. Kootte and C. Bisagni. A methodology to investigate skin-stringer separation in postbuckled composite stiffened panels. *AIAA SciTech 2020 Forum*, (2020-0477), 2020.
- [54] W.J. Vankan, B.H.A.H. Tijs, G.J. de Jong, H.C. de Frel, and N.K. Singh. Strength of notched and un-notched thermoplastic composite laminate in biaxial tension and compression. *Journal of Composite Materials*, 50(25):3477–3500, 2016.
- [55] I. Baran, L.L. Warnet, and R. Akkerman. Assessment of failure and cohesive zone length in co-consolidated hybrid C/PEKK butt joint. *Engineering Structures*, 168:420–430, 2018.
- [56] K.S. van Dooren, E. Labans, B.H.A.H. Tijs, J.E.A. Waleson, and C. Bisagni. Analysis and testing of a thermoplastic composite stiffened panel under compression. *Proceedings of ICCM22 – 22nd International Conference on Composite Materials*, (5108-2), 2019.
- [57] K.S. van Dooren and C. Bisagni. Design and analysis of thermoplastic welded stiffened panels in post-buckling. In *ASC 36TH Annual Technical VIRTUAL Conference: Composites Ingenuity Taking on Challenges in Environment-Energy-Economy*, pages 406–417, 2021.
- [58] C. Fualdes. Composites@Airbus. Damage Tolerance Philosophy. FAA Workshop for Composite Damage Tolerance and Maintenance, July 19-21, 2006. 2016.
- [59] M.L. Benzeggagh and M. Kenane. Measurement of mixed-mode delamination fracture toughness of unidirectional glass/epoxy composites with mixed-mode bending apparatus. *Composites Science and Technology*, 56:439–449, 1996.

- [60] L. Zhao, K. Wang, F. Ding, T. Qin, J. Xu, F. Liu, and J. Zhang. A post-buckling compressive failure analysis framework for composite stiffened panels considering intra-, inter-laminar damage and stiffener debonding. *Results in Physics*, 13:102205, 2019.
- [61] C.G. Dávila and C. Bisagni. Fatigue life and damage tolerance of postbuckled composite stiffened structures with indentation damage. *Journal of Composite Materials*, 52(7):931–943, 2017.
- [62] W. Wagner and C. Balzani. Prediction of the postbuckling response of composite airframe panels including ply failure. *Engineering Fracture Mechanics*, 77(18):3648–3657, 2010.
- [63] X.M. Wang, W. Cao, C.H. Deng, P.Y. Wang, and Z.F. Yue. Experimental and numerical analysis for the post-buckling behavior of stiffened composite panels with impact damage. *Composite Structures*, 133:840–846, 2015.
- [64] J. Zou, Z. Lei, R. Bai, D. Liu, H. Jiang, J. Liu, and C. Yan. Damage and failure analysis of composite stiffened panels under low-velocity impact and compression after impact. *Composite Structures*, 262:113333, 2021.
- [65] S. Lauterbach, A.C. Orifici, W. Wagner, C. Balzani, H. Abramovich, and R. Thomson. Damage sensitivity of axially loaded stringer-stiffened curved CFRP panels. *Composites Science and Technology*, 70(2):240–248, 2010.
- [66] W.D. Kroll, L. Mordfin, and W.A. Garland. Investigation of sandwich construction under lateral and axial loads. *NACA Technical Note*, NACA-TN-3090, 1953.
- [67] C.C. Chang and M.J. Timmons Jr. Compression tests of sandwich panels with facings at different temperatures: Experimental deflection pattern found to correlate well with the assumed orthogonal sine-wave deflection pattern. *Experimental Mechanics*, 2(8):249–256, 1962.
- [68] G.Y. Grondin, Q. Chen, A.E. Elwi, and J.J. Cheng. Stiffened steel plates under compression and bending. *Journal of Constructional Steel Research*, 45(2):125–148, 1998.
- [69] Y. Tanaka and H. Endo. Ultimate strength of stiffened plates with their stiffeners locally buckled in compression. *Journal of the Society of Naval Architects of Japan*, 1988(164):456–467, 1988.
- [70] B.H. Choi, M. Hwang, T. Yoon, and C.H. Yoo. Experimental study of inelastic buckling strength and stiffness requirements for longitudinally stiffened panels. *Engineering Structures*, 31(5):1141–1153, 2009.
- [71] A. Aalberg, M. Langseth, and P.K. Larsen. Stiffened aluminium panels subjected to axial compression. *Thin-Walled Structures*, 39(10):861–885, 2001.
- [72] T. Zha, Y. Moan. Experimental and numerical prediction of collapse of flatbar stiffeners in aluminum panels. *Journal of Structural Engineering*, 129(2):160–168, 2003.

-
- [73] E.K. Hahn, L.A. Carlsson, and B.S. Westerlind. Edge-compression fixture for buckling studies of corrugated board panels. *Experimental Mechanics*, 32:252–258, 1992.
- [74] J.W. van Ingen, P. Lantermans, and I. Lippers. Impact behaviour of a butt jointed thermoplastic stiffened skin panel. *SAMPE 2012 International Symposium and Exhibition*, 2012.
- [75] Z. Hashin and A. Rotem. A fatigue failure criterion for fiber reinforced materials. *Journal of Composite Materials*, 7(4):448–464, 1973.
- [76] I. Lapczyk and J.A. Hurtado. Progressive damage modeling in fiber-reinforced materials. *Composites Part A: Applied Science and Manufacturing*, 38(11):2333–2341, 2007.

LIST OF PUBLICATIONS

Journal publications

1. Kevin van Dooren, Jan Waleson, Mark Chapman, Chiara Bisagni. Buckling and failure assessment of curved butt-joint stiffened thermoplastic composite panels with roller boundary conditions. *Manuscript submitted to Elsevier*, 2024.
2. Kevin van Dooren and Chiara Bisagni. Post-buckling damage tolerance of welded omega-stiffened thermoplastic panels with initial damage. *Manuscript submitted to Elsevier*, 2023.
3. Kevin van Dooren and Chiara Bisagni. Design, analysis and testing of thermoplastic welded stiffened panels to investigate skin-stringer separation in post-buckling. *Composites Part B: Engineering* , 267:111033, 2023.
4. K.S. van Dooren, B.H.A.H. Tijs, J.E.A. Waleson, and C. Bisagni. Skin-stringer separation in post-buckling of butt-joint stiffened thermoplastic composite panels. *Composite Structures*, 304:116294, 2023.

Conference proceedings

1. K.S. van Dooren and C. Bisagni. Design and analysis of thermoplastic welded stiffened panels in post-buckling. In *ASC 36TH Annual Technical VIRTUAL Conference: Composites Ingenuity Taking on Challenges in Environment-Energy-Economy*, pages 406–417, 2021.
2. B.H.A.H. Tijs, K.S. van Dooren, and C. Bisagni. Development of a numerical framework for virtual testing to support design of a next generation thermoplastic multifunctional fuselage. In *European Conference On Multifunctional Structures (EMuS2020)*, pages 90–95, 2020.
3. K.S. Van Dooren, E. Labans, B.H.A.H. Tijs, C. Bisagni, and J. Waleson. Analysis and testing of a thermoplastic composite stiffened panel under compression. In *Proceedings of 22nd International Conference on Composite Materials (ICCM22)*, Melbourne, AU, August 11-16, 2019.

 Included in this thesis.

ACKNOWLEDGMENTS

Obtaining a doctoral degree is not only an individual accomplishment; it is also a shared achievement due to the support of those around you. Throughout my time at Delft University of Technology, I've had the pleasure of working with great colleagues. I greatly enjoyed having interesting discussions on subjects related to this dissertation, as well as dabbling into topics that are a mystery to me at times, like aerodynamics. While I've always appreciated the work-related activities and discussions with colleagues, the social aspect got me through the challenges of the PhD journey. Sometimes, a simple "how are you?" is the perfect remedy on a tough day.

Firstly, I would like to thank my promotor and daily supervisor, Prof Chiara Bisagni. I greatly appreciate the opportunities you gave me during the six years we've worked together. I got to do research as part of amazing projects, meet and work with great people, and become a more complete and independent researcher under your supervision. Your supervision and the collaborations with research institutes and industry partners you made possible gave me valuable insight and perspectives for the research. This ensured not only the relevance of the research both within and outside of academia but also really drew me into the topic. I wish you the best of luck with your new position, and I hope our paths will cross in the future.

I would also like to thank my promotor, Dr. Sergio Turteltaub. I've always enjoyed your interesting and engaging lectures, with the occasional topic-related puns and jokes. Your valuable input during the yearly meetings provided me with an independent viewpoint regarding my progress, what aspects I should focus on and the remaining steps necessary to obtain my PhD.

I would like to express my gratitude to the committee members: Bert, Chiara, Kai-Uwe, Matthijs, Richard, Richard, and Sergio, for taking the time to be part of the committee and showing interest in my work. I'm looking forward to the defence.

I've had the pleasure of collaborating with industry partners during my PhD, which gave me many research opportunities and helped me greatly. I want to thank Jan, Jaap Willem, Ivo, Bas, and Salvador for providing input to my research, for the test specimens and for always taking the time to answer my questions and discuss the research. I also want to thank Vipul and Carlos for showing interest in my research and the following discussions during their visit(s), I greatly appreciate it.

My time as a PhD researcher would not have been so memorable, fun, and educational without my dear friend, colleague and former housemate, Luc. I could always count on my consultancy partner in crime for discussions, sometimes to the annoyance of others, and for socialising with friends and colleagues. I want to thank you for your much-valued input, sanity checks, offering a helping hand, your amazing cooking, and for not judging my grocery list during the lockdown. The era of Kootte en van Dooren in academia has come to an end, and I'm looking forward to the next.

My sincere thanks to Linda for all of the support, always showing interest, the fun times as unofficial housemates, for suffering together when Luc's amazing food was a bit too spicy for us to handle, and for filling my Netflix recommendations with Bridget Jones's Diary and movies alike. I also want to thank Eva, for our conversations during coffee time and other social activities, talking about the ups and downs of the PhD and life, combined with a healthy dose of banter and gossip.

Thank you to Bas for bringing the industry to our office and for getting me back into cycling. Your industry knowledge and input were a great contribution to my work and provided me with direction and purpose. I also really appreciate the advice on writing, publishing and the final steps for finishing my Phd. I'm looking forward to many more bike rides with many Dutch hills to climb. I also want to thank Jens for keeping us on our toes in the so-called Dutch office; your interest in our language and our discussions on the most random topics gave us many amusing and light-hearted moments.

I also want to thank the following generations and visiting PhDs that internationalised the Dutch-office: Arne, Andres, Burhan, Merjem, Alessandro, Carmen and Giulia. Thanks for the many great moments in the office and during social activities. Special thanks to Arne for the work-related discussions, his enjoyable antics, the funny stories, and for joining in on bike rides and interval training. Also, thanks to Burhan for convincing me to join Boulderling. I feel lucky to have been surrounded in the office by great people, and I will miss it greatly.

During my Master's thesis and PhD, I was welcomed to the group by Ines, Marta, Javier and Yuqian from the cool kidz office. I want to thank you for making me feel like I belonged here, for introducing me to many people, for our many talks, and for your advice on the PhD and life in general. I appreciate it greatly that I could always come by with questions. We've had many enjoyable moments through the years, and I hope we continue to do so for many to come. Special thanks to Ines for your supervision during my Master's thesis, for being a great party host and for your wealth of Dutch facts and history.

Furthermore, many thanks to all of my PhD colleagues from the other offices for the conversations during lunches, quick chats during coffee time and other social activities: Giorgio, Panos, Niels, Hauke, Srikanth, Siddharth, Victor, Natalia, Stefan, Davide, Giovanna, Alfy, Camilla and Ioannis.

Arguably, my favourite office to barge into the last years, for coffee, talks and banter about both research and life, and a helping hand, was the post-doc and researcher office. A big thanks to: Javier, Antonio, Xavier, Nithya, Jing and Alex, for your interest, kindness, and patience and for showing us there's life after the PhD. I hope I didn't distract you too much with my many visits. A special thanks to Javier and Antonio for your Mediterranean influence and the many memorable moments both in and outside the office. Working in the lab during the lockdown was challenging, but it turned out to be one of the most enjoyable times of my PhD, thanks to you. I've also really enjoyed our holiday time together in Spain, with an exceptional (free) tour guide always by our side, and I hope it continues to be a tradition for many years to come.

My sincere appreciation to Edgars, for introducing me to working in the lab and for your help with the first tests.

I want to express my gratitude to the colleagues at ASM: Laura, Roeland, Daniël, Jurij, Saullo, Irene, Christos, Nan, Gemma and many more. My sincere thanks and appreciation

to Laura for always being there for us, cheering us up and for the always enjoyable welcome speech for new colleagues. You brought life and social cohesion to the department and made us realise there's more to life than the PhD, such as beers and sweetsies.

My work and research in the lab would not be possible and as enjoyable without the support from Dave, Alexander, Berthil, Gertjan, Victor, Fred, Johan, Johan and Chantal. I appreciate all of the tips, helping hands, setting up test machines, and troubleshooting. You made sure we had whatever we needed to perform our research. Also thanks to Peter and Ed for their support in specimen preparation, I could always rely on a quick turn-around.

I want to thank the Master students, Tara, Helena, Kübra, for the fun we had during social activities, but also for the discussions about their thesis research or my research, which I've always enjoyed.

I was lucky to have a great group of friends during the Masters, with whom I had great times working on assignments together, sharing the ups and downs of the thesis, enjoying the fun times during get-togethers, BBQs and many more activities. Thanks to: Guyonne, Tom, Katleen, Lander, Steven en Bram.

I also want to thank Vanessa for being a great housemate and for the many amusing moments over the years.

I want to express my appreciation to Fatma, for her encouragement during the concluding stages of my PhD, and for supporting me towards the end of this journey and beyond.

I want to thank my brother, Randy, for always being able to count on your support and advice. You pushed me when I needed it most but also allowed me to relax and take my mind away from academic life. An evening of casual gaming or bench-racing is the perfect medicine at times.

I'm very grateful to my parents, Jan and Harriët, for their unwavering support and the opportunities I got to pursue because of you. Knowing that I always have a home to go back to, allowing me to decompress and recharge, enabling me to be at my best, is something I cannot put into words.

BIOGRAPHICAL NOTE

Kevin Steven VAN DOOREN

Kevin van Dooren was born on April 18th, 1991, in Schaijk, The Netherlands. He went to De Regenboog in Schaijk for primary school, followed by pre-university education at MaaslandCollege in Oss. He finished his pre-university education at Rijn IJssel in Arnhem, while starting his bachelor of applied sciences in the same year.

He studied mechanical engineering at Fontys Hogescholen in Eindhoven, thoroughly enjoying the combination of theory and hands-on experiences. His first internship was in the R&D department of Vanderlande in Veghel, where he worked on fatigue failures in package sorting machines and methods for distributing packages before sorting. His graduation internship was at Marel Stork in Boxmeer, where he developed calculation methods for energy and water consumption of poultry processing plants and conducted tests at these plants for calibration and validation.

He enrolled for the Aerospace Bridging program at Delft University of Technology, looking for new challenges and expanding his horizon into a new field. The bridging program's steep learning curve was challenging, making it even more rewarding once he started his Master's.

He chose the structures program because of the closer affinity with his mechanical engineering background and interest in the bridging program structural analysis course. During his Master's, he took a particular interest in the courses on structural stability and design and analysis of composite structures. He graduated cum laude with his thesis on the buckling of scaled launch-vehicle cylindrical shells. His thesis included finite element analysis, studies on the effect of element type on buckling behaviour, and imperfection sensitivity studies on several scaled cylindrical shells.

Towards the end of his Master's Thesis, the opportunity of a PhD position arose, and he decided to take it based on the enjoyment of his Master's thesis research and his interest in the PhD topic. He greatly enjoyed the combination of experimental and numerical work during his PhD, in addition to social activities with friends and colleagues, sharing the highs and lows of academia. Now it's time for the next steps, and he's looking forward to new challenges.